INVESTIGATION OF THE CUTTING PROCESS IN SANDSTONES WITH BLUNT PDC CUTTERS

A Thesis

submitted to the University of London

(Imperial College of Science, Technology and Medicine)

by

Jose Raimundo Almenara Chau

In fulfilment of the requirements

for the degree of

Doctor of Philosophy

April 1992

Abstract

The forces acting on the tools when cutting rock are not only important for the design of the cutters but also because they can be utilized to characterize the rock being cut. To understand these forces, it is necessary to have a good insight into the mechanisms that govern the failure of the rock.

This thesis reports on studies of the cutting process with blunt — Polycrystalline Diamond Compact (PDC) — cutters. It presents a critical review of previous analytical, experimental and numerical models for the cutting mechanisms of single cutters. Associated mining and tunnelling studies suggest that the main rock cutting mechanism is tensile failure followed by fracture propagation. The work here provides evidence that these mechanisms are not applicable when drilling sedimentary rocks under pressure with PDC cutters — where it is more likely that the mechanisms of failure is different in nature, being ductile.

A cutting bit response model(Detournay and Defourny, 1992), which is based on ductile failure and considers the drilling process as a combination of a pure cutting action at the cutter face and a frictional contact at the wear flat, was selected for the present research. The model predicts that there is a linear relation between specific energy, $\mathcal{E}$, and the drilling strength, $\mathcal{S}$, which are two quantities with dimension of stress that are respectively defined as the horizontal and vertical force divided by the cross-sectional area of the groove traced by the cutter.

The two processes, the cutting and the friction at the interface, are then studied by means of finite difference simulations with a computer programme

Fast Lagrangian Analysis of Continua (FLAC). The numerical simulations are compared to the upper and lower bound plasticity solutions for this problem to determine the validity of the code. This code allows one to model large deformations and also friction at the tool/rock interface. The simulations were performed to determine:

- the validity of assuming that the two processes are independent; and
- to establish whether there is a linear relation between $\mathcal{E}$ and $\mathcal{S}$ by modelling different depths of cut.

An experimental programme of single cutter tests was undertaken to corroborate the numerical and analytical models. Results of cutting tests on three different sandstones using blunt PDC cutters are presented and analyzed. The experimental data support the theoretical prediction that there is a linear relation between the specific energy $\mathcal{E}$ and the drilling strength $\mathcal{S}$. Various quantities such as the cutting parameters (ϵ and ζ), the friction coefficient (μ) and the contact strength (σ) are estimated for each of the rocks tested.

The thesis also contains discussion on how these basic parameters of the drilling process are related to the geomechanical characteristics of the rocks tested. A discussion of the influence of small imperfections along the cutting edge of a "sharp" cutter on the determination of ϵ and ζ is also presented.

The main contribution of this research therefore is the verification of the cutting model, which in turn will enable the state of wear of PDC cutters to be established form the forces measured on site.

Acknowledgements

The author wishes to express his sincere gratitude to the people who helped in many ways in the completion of this thesis. In particular thanks are due to:

Prof J.A. Hudson for his encouragement, beneficial discussions, financial support and help in many other ways.

Dr. E. Detournay for his advice, guidance and clarifying discussions in the last 18 months.

Schlumberger Cambridge Research for their financial support and for providing the software for the numerical modelling.

The William Selkirk Scholarship and the Overseas Research Studentship.

Dr. D.H. Spencer, for proof reading and encouragement in the final stages of this thesis.

R. Marsden and J. Dennis for all their help during the experimental work.

The postgraduate students with whom the author has worked, for their friendship and interest in the author's work. They are: Yojiro Ikegawa, Eric Chaput, Kemal Gokay, Peter Arnold, Andy Hyett. Special thanks are due to Fabrice Cuisiat and Wei Lingli for their patience and understanding when interrupted with trivial questions.

The staff of the Rock Mechanics Research Group, notably, Miss Moira Knox and John Harrison for their help of many kinds.

Finally the author wishes to take the opportunity to thank his family, for their unconditional support and encouragement during all these years.

Contents

List of Figures

List of Tables

Notation

d	Depth of cut
$\vec{F}^c$	Cutting force
$\vec{F}^f$	Contact force
F_s^c	Horizontal component of cutting force
F_n^c	Vertical component of cutting force
F_s^f	Horizontal component of contact force
F_n^f	Vertical component of contact force
A	Cross-sectional area of cut
F_s	Measured force, parallel to the cutting surface
F_n	Measured force, normal to the cutting surface
γ	Bit constant
ϵ	Intrinsic specific energy
η	Drilling efficiency
φ	Internal friction angle
ψ	Friction angle at the cutter/rock interface
θ	Backrake angle of a PDC cutter
μ	Friction coefficient at the wearflat/rock contact
σ	Normal contact strength
ζ	Ratio of $\mathcal{S}$ over $\mathcal{E}$ when there is no friction
χ	Ratio of $\mathcal{E}$ over $\mathcal{S}$
$\mathcal{E}$	Specific energy
$\mathcal{E}_o$	Intercept of the friction line with the $\mathcal{E}-$axis
$\mathcal{S}$	Drilling strength

Chapter 1

Introduction

1.1 Industrial Background

The mining and petroleum industries have been interested for many years in the mechanisms of rock drilling/cutting. Research in the subject started in mining, in the early 1950s, to improve the performance of drilling/cutting equipment. It has continued up to now, trying to establish the relevant geoparameters that will provide an idea of how the rock will behave when drilling with different tools.

The investigation of the mechanisms of cutting has been concentrated on the forces necessary to break the rock by mechanical means. However, the researchers through the years have not reached a consensus on what the mechanisms are. Moreover, the introduction of new materials and new designs of cutters have stimulated continuing investigations.

In the late 1970s, the oil industry took an increasing interest in reducing costs of drilling operations, as the drilling was performed in more difficult conditions and the reservoirs became deeper and smaller. As the major part of the cost linked to the exploitation of an oil field is due to drilling, it is very important to optimize this operation. The introduction of Polycrystalline Diamond Compacts (PDCs) came at this stage, creating a breakthrough in drilling technology.

When drilling for exploration and production of oil, the drill bit is at several thousands of meters below the surface, where the process cannot be seen, as

opposed to the operations of tunnelling with mechanical excavators. It is thus important to determine from the surface how the tool is behaving and in what condition of wear it is. Changing a drill bit is a time consuming process, so if by monitoring torque and weight on the bit one could determine the state of wear of the tool, one could optimize the process by avoiding unnecessary stoppages. However, the recordings of the torque and weight on the bit, have to be interpreted — and that is why the processes have to be known.

The different tools, drag bits and indenters, have been tested in laboratories all around the world. Despite this, there has not been a consensus of opinion on what the mechanisms of cutting and failure are. This is probably because different tools act differently on the rock being tested. The depth of cut with relation to the microstructure of the material, the state of rock stress, and the mud used are other factors that affect these processes.

1.2 Purpose of the Research

The mechanisms of cutting have been studied since the early 1950s, see for example Fish[11, 12]. Since then, many models have been suggested for predicting the forces on the cutter. They also suggest the failure mechanisms of the rock when subjected to forces on its surface by indentation, dragging, or impact.

The purpose of this research is:

- to gain an understanding of the mechanisms of cutting rock with drag bits,
- to substantiate a model that considers the cutting process as two independent processes: one of cutting and the other of friction at the tool/rock interface, by means of numerical and experimental techniques, and
- to provide a new set of experiments carefully performed for the study of wear on PDC cutters.

1.3 Content of the Thesis

In Chapter 2, the available knowledge on rock cutting is reviewed in order to establish the models for the forces on a single tool, that could be applied to the study of blunt PDC cutters. The correlations between the cutting forces and the geomechanical characteristics of the tool are presented to show the different opinions on the subject. The different mechanisms of failure observed on cutting rock are discussed.

A model presented by Detournay and Defourny[6] is found to be promising, but needs substantiation. This model is described and the concepts of specific energy, drilling strength, $\mathcal{E}$–$\mathcal{S}$ diagram, friction line, and cutting point are introduced.

Chapter 3 presents a numerical investigation of the model[6] utilizing an explicit finite difference code, FLAC[7]. The purpose is to verify the model's prediction that rock cutting is a combination of two *independent* processes, one of pure cutting and the other of friction at the tool/rock interface. This is achieved by modelling a sharp tool, the contact at tool/rock interface, and the blunt cutter.

Chapter 4 introduces the experimental programme for linear cutting tests in three sandstones. It presents the laboratory equipment, the acquisition system and the principal characteristics of the tools. A discussion on the criteria used for the selection of the rocks to be tested is given. It also introduces the results obtained by Chaput [10] with sharp PDC cutters, as well as the tests performed for the present thesis with blunt PDCs under the same testing conditions.

Chapter 5 analyzes the results of the cutting tests with blunt PDCs following the model presented in Chapter 2, and describes the characteristics of the $\mathcal{E}$–$\mathcal{S}$ diagram. In this Chapter, the friction line will be studied as a mean of characterizing the rock for cuttability by attempting a correlation with the internal friction angle of the rock.

The average resultant force applied to the tool will be decomposed in its two components; "pure" cutting and friction at the contact, and a relation between

these forces with geomechanical parameters of the rock will be determined.

Chapter 6 concentrates on the final conclusions of the thesis. It discusses the contribution to industry and proposes future research in the area of rock cutting.

Chapter 2

Review of Current Knowledge on Rock Cutting

2.1 Introduction

There are two main types of cutting tools used in rock cutting, the drag bits or picks and the indenters (see Fig. 2.1). The drag bits apply a force to the rock due to the relative parallel movement of the tool across the surface to be cut. The indenters are tools that induce failure by the penetration of a wedge into the rock: the force applied is predominantly perpendicular to the rock surface. This chapter will review some of the research done earlier in the mining and the petroleum industry with drag bits. The main purpose of the research by the mining and tunnelling industries was to assess cuttability. For this reason the research was directed to find correlations between rock properties and cutting efficiency parameters. In petroleum, gas, and geothermal drilling, the purpose is to achieve higher rates of penetrations and bit life, by improving the design of the drilling tool. Drilling was performed mainly by roller cone bits, which are indenters, until the introduction of PDCs in early 1970s. PDCs were a break through in technology because of their wear resistance. PDC cutters are made of a circular and fine layer of synthetic polycrystalline diamond supported by a base of tungsten carbide.

In the following sections, a review of the research performed in rock cutting by

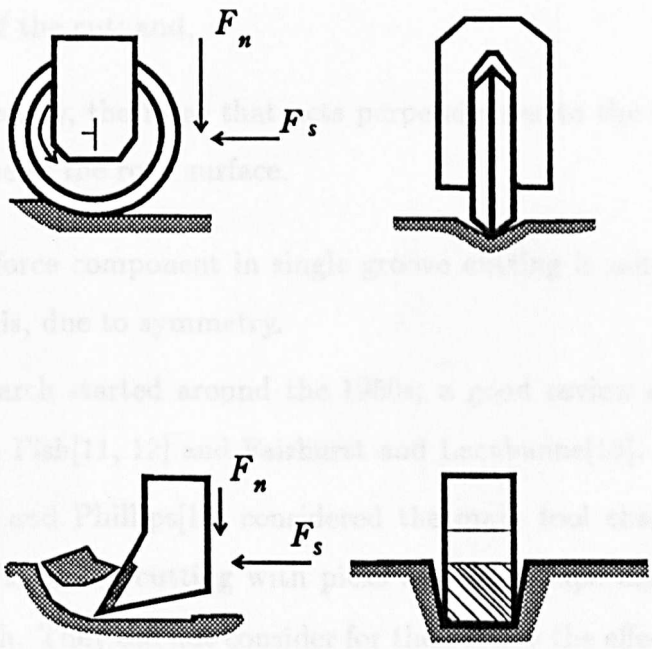

Figure 2.1: Drag bit and indenter (after Roxborough and Rispin[1]).

the mining industry, the several investigations on attempted correlations with geomechanical parameters, and then the research on PDCs will be presented. Some important models for the forces on a single drag cutter will also be presented. A detailed presentation of the cutting and friction model[6] will be given as it is the model subject of this research.

2.2 Single Drag Bit Tests

Drag bits are used in rotary drills and in excavation machines such as road-headers and coal ploughs.

Drag bits are produced in different shapes. When linear cutting tests are performed, the total force can be decomposed in three orthogonal forces:

- normal force, F_n, the force acting perpendicular to the cutting surface (the force directed to the rock mass is considered positive);

- cutting force, F_s, the force acting parallel to the cutting surface and in the direction of the cut; and,

- lateral force, F_l, the force that acts perpendicular to the cutting force but in the plane of the rock surface.

The lateral force component in single groove cutting is normally discounted from the analysis, due to symmetry.

Drilling research started around the 1950s; a good review of the early work can be found in Fish[11, 12] and Fairhurst and Lacabanne[13].

Roxborough and Phillips[14] considered the main tool characteristics to be analyzed when studying cutting with picks as: pick shape and size, front rake angle, and width. They did not consider for their study the effect of the wearflat, so this parameter was not taken into account. The geometrical parameters to describe a drag bit cutter are shown in Fig. 2.2. In the present work, front rake angle will be considered positive if the tool's cutting face is inclined forward. They regarded depth of cut, rock strength, rock microstructure and geometry of the tool as the parameters that affect the magnitude of the forces on the tool when cutting rock at a prescribed depth. These variables have been studied in several researches some of which will be reviewed below.

From observations of linear cutting tests, several researchers[2, 10, 14, 15] have qualitatively described the process as a sequence of events which includes crushing of material, chip formation and reworking of the groove cut to take the shape of the tool.

From the same observations and measurements of the tool forces, Fairhurst and Lacabanne[13] as well as others[16, 17, 18, 19] proposed that the forces on the tool were due to the cutting action and to friction on the tool/rock interfaces. These interfaces are located between the cutter face, the wearflat contact, and the rock. Zijsling[17] also concluded that at the wearflat interface, a layer of rock flour adheres to the tool. The friction coefficient used, for his thermal model at

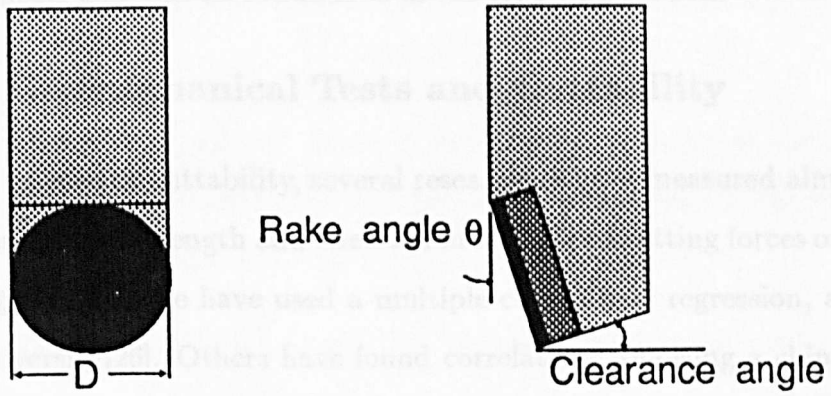

Figure 2.2: Geometrical parameters of a drag bit cutter.

this interface, is then assumed to be equal to the internal friction angle of the rock. Whittaker[16] studied the effect of tool shape on the cutting forces. He performed tests with different rake angles, clearance angles and blunt tools. From his investigations, he proposed a model for the vertical and the horizontal force on the tool considering a friction component.

Barker[20] presented results of cutting tests carried out with two types of drag bits, a chisel and a point attack pick. He found that the forces depended on the depth of cut, also that the forces induced on the chisel pick were larger than for the pointed one. He concluded that the efficiency of the cutting process increases to a maximum with depth of cut. The specific energy of cutting, i.e. the energy input per unit volume, was less for the chisel pick even though the forces for this tool were higher.

Several investigators[14, 21, 22, 23] have reached the conclusion that the speed of cut does not influence the cutting performance, but the normal force increases

considerably with speed as the tool wears out faster due to the heat generated by abrasion[23, 24, 25]. At slower speeds less energy is dissipated as heat.

Additional cutting tests have been performed with this type of tool for mining purposes, but most of the results presented are correlated with some geomechanical parameter and will be introduced in the following section.

2.2.1 Geomechanical Tests and Cuttability

In trying to predict cuttability, several researchers have measured almost all the parameters of rock strength and tried to relate them to cutting forces or efficiency of cutting tools. Some have used a multiple curvi-linear regression, as at Newcastle University[26]. Others have found correlations following a chip formation model.

Correlations between laboratory cutting tests and geomechanical properties are a difficult task if the cutting mechanism is not well understood. Correlations of laboratory experiments with field data are also complex as, in the field, many variables are difficult to control or measure. For example, tunnelling machines spend only a small percentage of the energy input to cut the rock, most of the energy is to drive the machine, to clamp it, or to muck the waste out. The other way of correlating drilling performance with rock properties is utilizing penetration rates, but this approach has to take into account the wear on the tool, as it will influence the cutting process and performance.

Misra[27], in his work, "drillability studies of rotary-percussive drills", used a large number of rock parameters to find a relation with machine performance. He found many correlations between drillability and uniaxial compressive strength, triaxial testing results, static Young's modulus, Shore scleroscope hardness, impact hardness, apparent density and apparent porosity. The most important of these is the correlation between drillability and the rock impact hardness number. This is because the test is similar to the mode of failure during excavation. The impact hardness test is a form of incremental crushing test. Misra's work

included a dimensional analysis in addition to single and multiple-variable curvilinear correlation analysis.

The U.S.B.M. covered a limited number of material properties and their analysis is based on a stepwise multiple linear regression.

The two U.S.B.M. groups involved in the research fundamentally disagree over a specific parameter:

- Morrell *et al.*[28] stated: "simple compressive strength of the rock is not fundamentally related to the rock breaking mechanism and therefore cannot be used as a reliable method of predicting machinability".
- Rad and Olsson[29, 30] found that compressive strength could be used to predict some of the cutting characteristics of independent grooves.

Many other correlations have been proposed in the literature between measured rock properties and cuttability. Some of these proposed correlations are given below.

McFeat-Smith and Fowell[26] used a multiple curvilinear regression program to analyze the data collected, in order to determine the properties of importance in explaining the cutting and wear characteristics of different rocks. They measured 23 different rock parameters from mineralogic composition to hardness and compressive strength. They also performed linear cutting tests obtaining the specific energy of cut for each type of rock. Their analysis showed that the most relevant parameters for the cutting process were cone indenter hardness and plastic deformation. For the case of wear on the tool, they concluded that quartz content, cementation coefficient and the shore rebound hardness were the parameters that gave the best correlations. The results were then used as prediction equations.

Morgan *et al.*[31] and O'Rourke and Priest[32] present a case history of tunnelling work for the Kielder Reservoir project. A good regression result is obtain by taking the mean values of Schmidt hammer tests for various geological zones against the field cutting rate.

Jenni and Balissat[33] concluded that penetration rate can be predicted with the use of a combined index including rebound hardness, point load strength, abrasion hardness and content of minerals with equal or higher hardness than quartz.

McFeat-Smith and Tarkoy[34], in order to determine the relation between rock material properties and penetration rates for two specific machine types, correlated point load test data with penetration rates.

Tarkoy and Hendron[35] compared rock hardness indices, uniaxial compressive strength and penetration rates for a variety of tunnel boring machine projects and showed correlations between penetration rates and rock properties (from Nelson and O'Rourke[36]).

Ingraffea *et al.*[37] introduced a new approach for cutting performance predictions. They studied fracture toughness, K_{Ic}, as a property that will give a better rock parameter to be used for sensitive predictions of tunnel boring machine performance. They used the short rod technique to obtain their values and then they related them to other rock properties, analyzing variability.

Nelson *et al.*[38], after an analysis had been made on the cutting mechanism, reached the conclusion that rock fracture and chip formation is a process in which energy is consumed in the creation of new surface area. They studied the relation between K_{Ic}, G_{Ic} (fracture energy) and the field penetration index of two case history tunnels. They arrived at the conclusion that for massive, brittle materials, the critical energy release rate can be correlated with optimum machine performance. That the correlation is consistent with the formation of rock chips is because of the fracture process. The correlations were performed for only four types of rock so the results were speculative but promising. They also concluded that the critical energy release rate can be correlated with optimum TBM performance and that this correlation is consistent with the formation of chips by a fracture process.

Nelson and Fong[39], in advancing the previous work, took the results from linear cutting tests (disk) performed at the Transport and Road Research Laboratory, and correlated the non-interactive rolling and normal forces (force/penetration) with the crack driving force, G_{Ic}. The trend seems to be linear. These results need to be confirmed as suggested by these researchers. Continuing with this new approach, they performed a series of fracture toughness tests and linear cutting tests with discs in five different British rocks and studied the relation between the normal forces and the crack driving force, G_{Ic}. They arrived at the conclusion that prediction of disc cutter forces and force penetration relations is possible using fracture material properties.

Almenara[40], in his M.Sc. dissertation, performing linear cutting tests with picks in three different rocks, found an apparent linear relation between peak cutting forces and fracture toughness values. The same trend was found also between specific energy of cutting and energy release rate, G_{Ic}. He agrees with Nelson *et al.*[38] that the correlations are consistent with the formation of chips in the cutting process, when the depths of cut are deep enough and the tools are of the chisel type. Short rod specimens were used in this case to obtain the fracture toughness values.

2.2.2 PDC Cutter Experiments

PDC cutters, are made of a circular and fine layer of synthetic polycrystalline diamond supported by a base of tungsten carbide. This set is then bonded to a matrix or to WC/Co studs that then are placed on a steel body.

Feenstra[41, 42] presents a good review on the development and application of PDC bits in petroleum drilling. He presents the special characteristics of PDCs, an overview on the temperature stability of the material, its impact resistance and the main problems, which are bit-balling and bit cleaning. Varnado *et al.*[43] carried out cutting tests in granites and Carthage Marble. They found that to avoid PDC chipping and obtain a self sharpening effect, when drilling hard rocks,

it is better to have cutters with high back-rake angle (they suggested greater than 30°).

Cheatham and Daniels[44] performed single cutter experiments to study the mechanisms of cutting on Pierre and Mancos shales. They carried out experiments with three different cutter shapes: a round, a rectangular and a 90° triangular profile. Different rake angles were also studied (+20° to -20°) as well as borehole pressure effects. They found that under elevated borehole pressures the cuttings of shale were very similar to those obtained from lead and plasticine clay cut at atmospheric pressure. The rectangular section cutter experiments showed that the average horizontal and vertical forces increased almost linearly with depth of cut. They also found that the cutting forces increased with increasing rake angle and suggested that this could be reasonably represented by the Merchant metal cutting theory. When the rake angle decreased, the forces did not decrease as predicted by the theory. They claimed that this was partially due to clogging of the tool (bit-balling). Tool profile experiments showed that the cutting force per unit area remains constant for all the tool shapes.

Glowka[18, 24, 45, 46] carried out an extensive investigation on wear of PDC tools. He analyzed the effect of temperature on wear and also studied the effect of wear on the efficiency of the cutting tool. From his investigations, he proposed empirical relations for the cutting and the normal forces:

$$F_n/A_w = C_1\delta^{n_1} \tag{2.1}$$

$$F_n = C_2\delta^{n_2} \tag{2.2}$$

$$K_d = \frac{F_s}{F_n} \tag{2.3}$$

where A_w is the wearflat area, C_1, n_1, C_2 and n_2, are determined by linear regression on data in log-log space of linear cutting tests. Eq. (2.1) is for blunt tools and Eq. (2.2) for sharp tools. The data presented by Glowka have considerable scatter, even though at least 5 replications were performed on each test.

Several tests have been performed with full scale PDC bits[43, 47, 48, 49].

Their observations with respect to the effect of wear on the torque and thrust are similar. As the tool wears out, the torque and the thrust need to be increased to achieve the same rate of penetration.

2.2.3 Single Cutter Models

The oldest model to describe the process of cutting was developed for metals by Merchant [50, 51, 8], and is defined by the material's shear strength. By giving a geometry for the chip formed, the components of the forces parallel and perpendicular to the face of the tool are calculated and compared with the strength of the metal, using the Mohr-Coulomb criterion. This model has served as a basis for other models, such as the ones described below.

Evans[52], based on early experimental work, showed that during the penetration of wedges normal to the surface in certain types of coal, cracks attributed to tensile breakage radiate from the tip of the wedge. The mode of entry of the wedge appears to be primarily through the crushing of the coal against the surface of the wedge. This is because the force required is mainly related to the compressive strength of the coal. However, since the fracture of an idealized buttock is due to propagation of cracks from a wedge tip to a free surface, the breakage mechanism proposed may be considered to be tensile. This model explains the cutting mechanism with a tensile strength criterion.

Nishimatsu[2] gives a similar approach. He explains the rock cutting process as a mechanism with three different stages (Fig. 2.3):

1. Formation of the Primary Crushed Zone. The tool edge is pushed into the buttock, where a crushed zone is generated about the tool edge. The material is recompacted and sticks to the tool edge.

2. Coarse Cutting Chip. A critical value of penetration generates a state of stress which allows the propagation of a macroscopic failure crack.

3. Fine Cutting Chip. The remaining peak of rock is removed as the tool moves

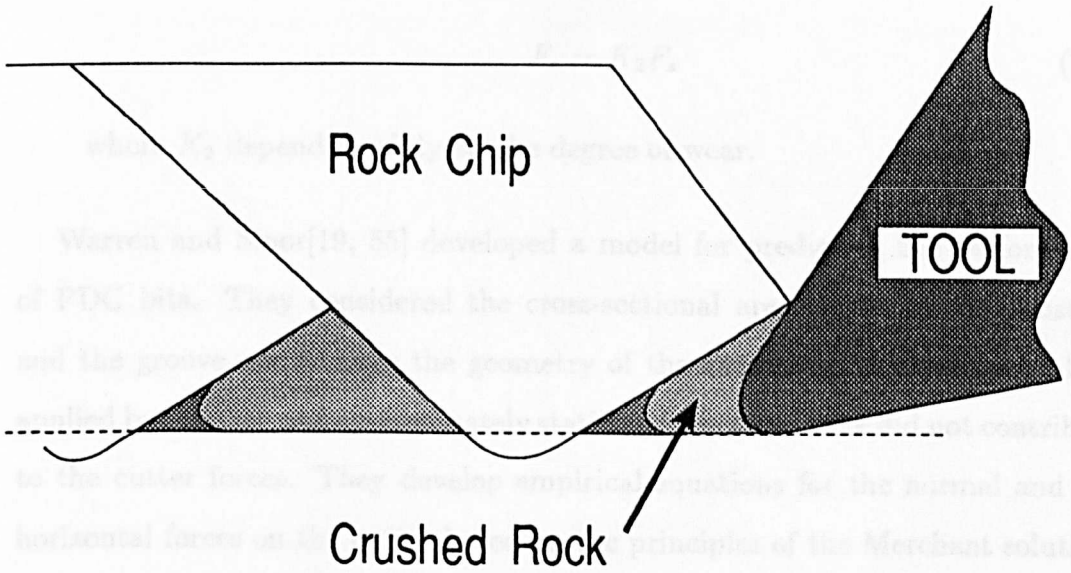

Figure 2.3: Cutting process (after Nishimatsu[2]).

forward.

The only difference that he found was that failure is due to compressive stress induced by cutting forces. This is based on his observations on the cutting process.

Lebrun[53, 54], extending Nishimatsu's theory, developed a three dimensional model for the failure of rock subjected to the action of a cutting tool. It assumes that the depth of cut to be much smaller than the width of the tool. He proposed two principles that regulate the action of a single pick and two others for the deepening and interaction between two cutters. The ones of interest for this research are:

1. Linear relation between the cutting force, F_s, and the depth of cut, δ:

$$F_s = K_1 \delta \tag{2.4}$$

where K_1 is an experimental coefficient that increases with the width and

wear of the cutter and decreases with the rake angle.

2. Linear relation between the cutting force, F_s, and the normal force, F_n:

$$F_n = K_2 F_s \tag{2.5}$$

where K_2 depends mainly on the degree of wear.

Warren and Sinor[19, 55] developed a model for predicting the performance of PDC bits. They considered the cross-sectional area of the cut as constant and the groove cut to have the geometry of the cutter, and also that the load applied by the tool was approximately static and the failed rock did not contribute to the cutter forces. They develop empirical equations for the normal and the horizontal forces on the cutter based on the principles of the Merchant solution. Their horizontal force component consisted of two parts: a chip generation force and a frictional (non-productive) component.

A new model for the forces on the cutting tool, based on the suggestions of Fairhurst and Lacabanne[13], has been recently published by Detournay and Defourny[6]. It considers the basic cutting process as combination of cutting and friction. It assumes a constant cross-sectional area of cut and friction at the tool/rock interface. They used their model to analyze Glowka's extensive work with blunt cutters in Berea sandstone and concluded that the scatter of the data was due to the geometry of the wearflat on the tools that Glowka used. Because the wearflat was parallel to the direction of motion of the cutter, the wearflat area was not the same as the contact area. This model will be presented in detail in Section 2.3, as it will be the subject of the present research.

An alternative approach to rock cutting analysis is obtained by using finite element methods.

Wang and Lehnhoff [3] attempted several computations with indentation models for different bit geometries. A typical result is presented in Fig. 2.4. Their analysis considered that the tool/rock interface was very rough, not allowing rel-

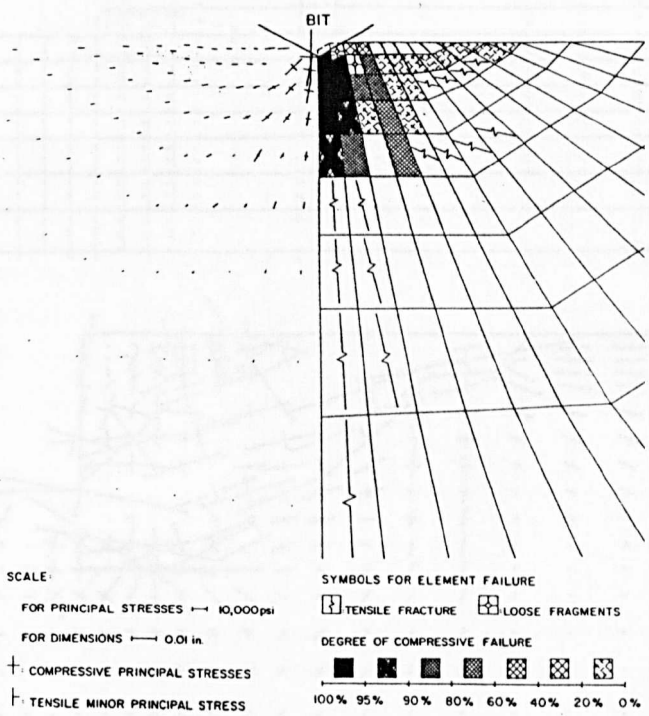

Figure 2.4: Sharp wedge bit penetration (after Wang and Lehnhoff[3]).

ative displacement of the material with respect of the tool. They had relative success in representing failure under indentation conditions.

Sellami and Deliac[4] carried out a finite element model (FEM) simulation of pick penetration up to a condition of rock failure-penetration and subsequent shearing of a chip. Fig. 2.5, shows concentrations of stresses under the action of a pick on a buttock.

Swenson[56] studied drag bit cutting using a finite element code that allowed large deformations. A maximum tensile strength together with Mohr-Coulomb shear failure criterion were used. Post-failure behaviour was set to follow the shear failure criteria if the surface crack was subjected to compression; if not, the code assigns zero to the shear stresses along this surface. The friction at the contact between the tool and the rock was taken to be zero. A few experiments were performed under atmospheric conditions for comparison with the numerical predictions. He could simulate the predominant characteristics of the cutting

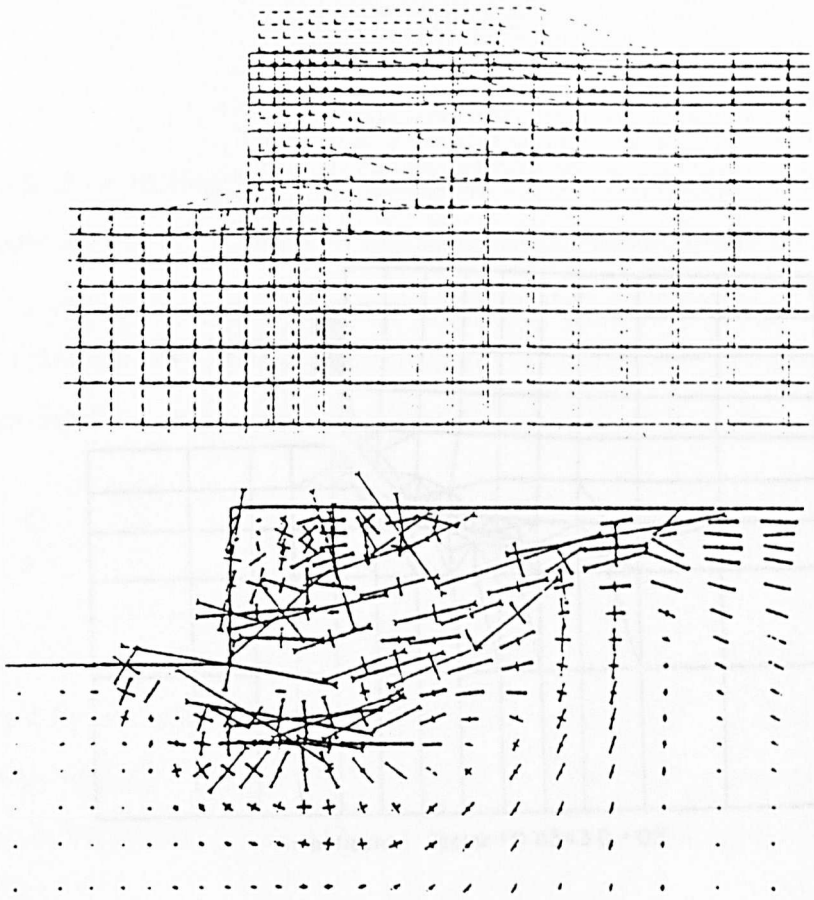

Figure 2.5: FEM simulation of pick penetration (after Sellami and Deliac[4]).

process but not all of it. A combination of crushing underneath the tool and a tensile chip formation could be modelled in atmospheric conditions. When a high borehole pressure was imposed, tensile failure changed to plastic shear. A wearflat of length equal to the depth of cut was also modelled. The vertical force required to maintain the depth of cut was enough to create indentation type fractures on the rock, even when the cutter was moving parallel to the rock surface.

These studies used the Mohr-Coulomb failure criterion and considered the stress conditions set up within the represented rock mass.

A different approach was proposed by Saouma and Kleinosky[57]. Rather than shear or compressive failure, a continual re-meshing during the simulation allowed them to produce a model with tensile cracks and a linear elastic fracture mechanics solution.

Ingraffea *et al.*[37] studied crack propagation with a fracture mechanics ap-

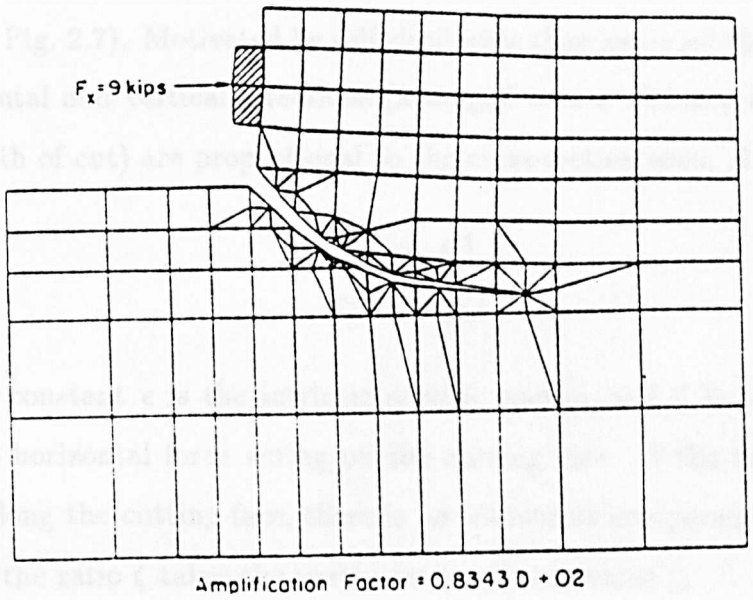

Figure 2.6: Final deflected shape and crack trajectory (from Ingraffea[5]).

proach, using finite element methods to model fracture propagation in rock. In 1987 he[5] presented an example problem (Fig. 2.6) that simulates "in a very simplified manner" a plane strain analysis of chip formation under a cutter.

2.3 Cutting and Friction Model

A model has recently been introduced by Detournay and Defourny[6], based on the assumption that rock cutting is actually a combination of two processes, "pure" cutting and frictional contact underneath the cutter. The basic equations of the cutting response model are summarized in the following.

2.3.1 Perfectly Sharp Cutter

The model considers first a perfectly sharp cutter which creates a groove of constant cross-sectional area, A, when it is moved across a horizontal rock surface at a constant depth of cut. This cutter can only transmit a force through the

contact of its cutting face with the rock. Let $\vec{F}^c$ denote this force and F_s^c and F_n^c its components in the parallel and normal directions to the rock surface respectively (see Fig. 2.7). Motivated by self similarity, they assumed that the forces in the horizontal and vertical directions (averaged over a distance large compared to the depth of cut) are proportional to the cross-section area, A:

$$F_s^c = \epsilon A \tag{2.6}$$

$$F_n^c = \zeta \epsilon A \tag{2.7}$$

where the constant ϵ is the intrinsic specific energy, and ζ is the ratio of the vertical to horizontal force acting on the cutting face. If the failed rock flows upwards along the cutting face, there is no transverse component of the cutting force, and the ratio ζ takes the particular maximum value ζ_*

$$\zeta_* = \tan(\theta + \psi) \tag{2.8}$$

where ψ denotes the interfacial friction angle and θ the back rake angle of the cutter.

2.3.2 Blunt Cutter

Force Decomposition. For a blunt cutter, the model is extended by assuming that two force vectors $\vec{F}^c$ and $\vec{F}^f$ act on the tool during cutting. The first force vector, $\vec{F}^c$ is transmitted by the cutting face, while the second one, $\vec{F}^f$, acts across the wearflat area of the blunt cutter (see Fig. 2.8). This second force vector can be decomposed into a horizontal and normal components, F_s^f and F_n^f, that are related by the friction law:

$$F_s^f = \mu F_n^f \tag{2.9}$$

where μ is a coefficient of friction.

From these basic equations, a linear relation between F_s, F_n, and A can be written:

$$F_s = (1 - \mu\zeta)\epsilon A + \mu F_n \tag{2.10}$$

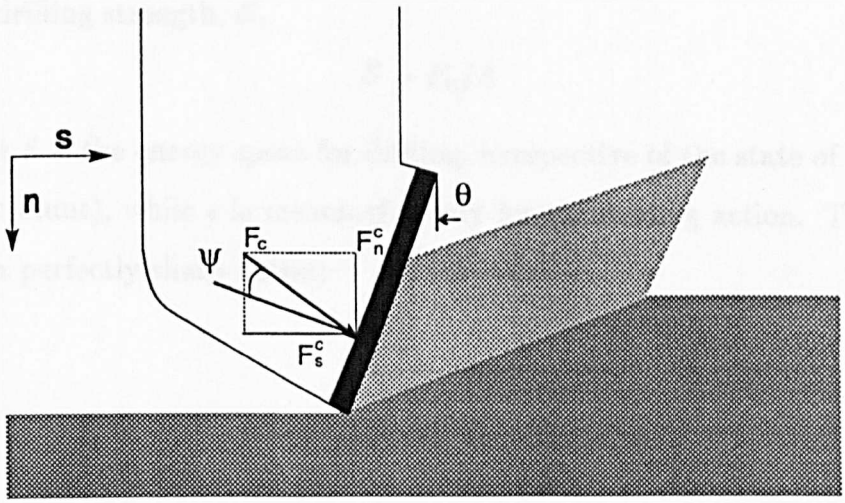

Figure 2.7: Forces acting on a sharp cutter (after Detournay and Defourny[6]).

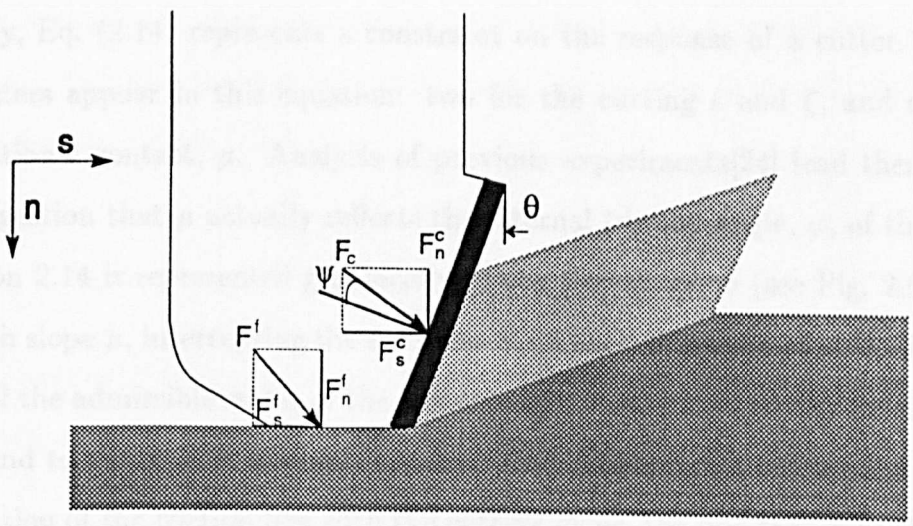

Figure 2.8: Forces acting on a blunt cutter (after Detournay and Defourny[6]).

$\mathcal{E}$–$\mathcal{S}$ Diagram. They then introduce two quantities: the specific energy, $\mathcal{E}$, defined as,

$$\mathcal{E} = F_s/A \tag{2.11}$$

and the drilling strength, $\mathcal{S}$,

$$\mathcal{S} = F_n/A \tag{2.12}$$

Note that $\mathcal{E}$ is the energy spent for drilling, irrespective of the state of the cutter (sharp or blunt), while ϵ is meaningful only for the cutting action. This means that for a perfectly sharp cutter:

$$\begin{aligned} \mathcal{E} &= \epsilon \\ \mathcal{S} &= \zeta\epsilon \end{aligned} \tag{2.13}$$

For a blunt cutter, there exists a linear relation between $\mathcal{E}$ and $\mathcal{S}$, which is obtained by dividing Eq. (2.10) by A:

$$\mathcal{E} = \mathcal{E}_o + \mu\mathcal{S} \tag{2.14}$$

where the quantity $\mathcal{E}_o$ is defined as

$$\mathcal{E}_o = (1 - \mu\zeta)\epsilon \tag{2.15}$$

Actually, Eq. (2.14) represents a constraint on the response of a cutter. Three parameters appear in this equation: two for the cutting ϵ and ζ, and one for the frictional contact, μ. Analysis of previous experiments[24] lead them[6] to the suggestion that μ actually reflects the internal friction angle, φ, of the rock. Equation 2.14 is represented graphically in the $\mathcal{E}$–$\mathcal{S}$ diagram (see Fig. 2.9) by a line with slope μ, intercepting the $\mathcal{E}$-axis at $\mathcal{E}_o$. This line is defined as the friction line. All the admissible states of the response of a PDC bit lie on the friction line above and to the right of the cutting point. The cutting point is the point at the intersection of the friction line with the cutting locus, the line that goes through the origin with a slope of ζ^{-1}.

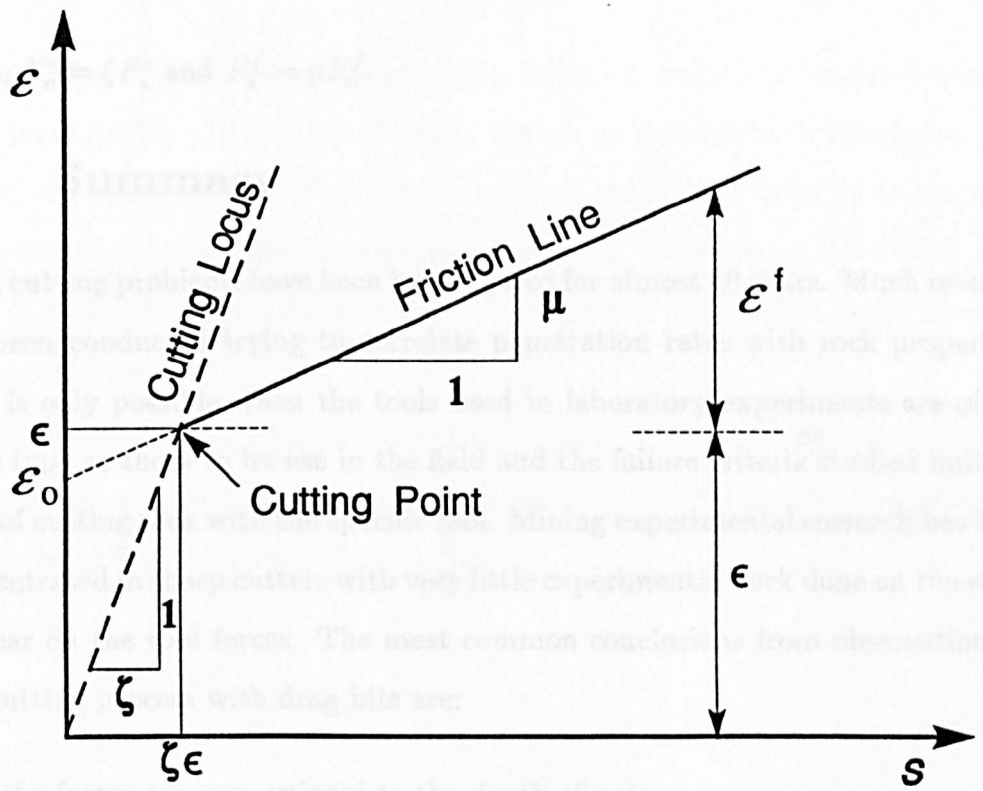

Figure 2.9: $\mathcal{E}$–$\mathcal{S}$ Diagram (after Detournay and Defourny[6]).

Contact Forces. Nothing has been said so far on the magnitude the frictional contact forces. It is expected that there is an upper bound on these forces due to failure of the rock underneath the cutter wear flat.

There are different ways (requiring different assumptions) to estimate the contact forces (this is further discussed in Section 5.4). One approach is to remove the cutting contribution from the cutter force; this assumes that both the cutting parameters ϵ and ζ are known:

$$\begin{aligned} F_s^f &= F_s - \epsilon A \\ F_n^f &= F_n - \zeta \epsilon A \end{aligned} \tag{2.16}$$

Another approach is to decompose the cutter force directly into its cutting and frictional contact components, assuming ζ and μ known:

$$\begin{aligned} F_s^c &= \frac{F_s - \mu F_n}{1 - \mu\zeta} \\ F_n^f &= \frac{F_n - \zeta F_s}{1 - \mu\zeta} \end{aligned} \tag{2.17}$$

Then, $F_n^c = \zeta F_s^c$ and $F_s^f = \mu F_n^f$.

2.4 Summary

Rock cutting problems have been investigated for almost 40 years. Much research has been conducted trying to correlate penetration rates with rock properties. This is only possible when the tools used in laboratory experiments are of the same type as those to be use in the field and the failure criteria on studied imitates that of cutting rock with the specific tool. Mining experimental research has been concentrated in sharp cutters with very little experimental work done on the effect of wear on the tool forces. The most common conclusions from observations of the cutting process with drag bits are:

- the forces are proportional to the depth of cut;
- forces increase with rake angle;
- two failure mechanisms are observed for different conditions, tensile and shear failure;
- the horizontal and vertical forces increase with wear on the tool;
- the force acting on the tool is due to the load needed to cut the rock and a non-productive component mainly due to friction at the interface tool/rock;
- the cross-sectional area of the groove cut can be approximated to the cross-sectional area of the cutting face in contact with the rock for shallow depths of cut;
- the Merchant theory for cutting metals has been the basis for the development of several models for the forces on the tool; and
- when drilling under high borehole pressures the rock behaves as a ductile material.

From these observations, a new model for sharp and blunt cutter forces has been presented[6]. It takes into account friction at the tool/rock interfaces. This model was tested against Glowka's comprehensive series of tests on Berea sandstone but due to the uncertainty encountered in determining the real contact area, it could not be concluded that the cutting and the friction forces were two independent processes.

Following this new idea, a numerical simulation, that will attempt to verify that cutting and friction at the tool/rock interface are two independent processes will be investigated in the following chapter.

Chapter 3

Numerical Analysis of the Cutting Process

3.1 Objectives and Philosophy of the Numerical Investigation

Previous numerical investigations of the drilling mechanisms have been reported in Section 2.2.3. In this chapter of the thesis, the purpose is to validate, by using a numerical model, the assumption that the drilling process with PDC bits can be regarded as two *independent* mechanisms: *i.e.* pure cutting and friction at the tool/rock interface[6]. The numerical model is based on the assumption that the material is characterized by a cohesion frictional yield condition of the material in front and underneath the tool's wearflat with friction on both tool/rock interfaces. The objectives and methods to achieve this purpose are presented below:

- test the validity of the numerical code for the investigation of the cutting and the frictional components of the drilling process;
- validate the cutting model by decomposing the cutting forces into two parts, pure cutting and frictional contact underneath the cutter;
- determine the intrinsic specific energy ϵ and the contact strength σ; and
- gain an insight on the mechanisms of failure.

This numerical investigation will start with an assessment of the validity of the numerical code by modelling a retaining wall with zero friction angle at the interface wall/soil(because the Merchant cutting solution and retaining wall solutions are similar). The numerical modelling will continue by studying two processes, one that simulates cutting with a sharp tool and the other that models the wearflat of the tool alone. Then it will proceed with the validation of the phenomenological drilling model. The last task will be achieved by modelling the blunt tool. For all the models studied, an example of the sequence of the FLAC instructions used in the simulations is presented in Appendix A. Tables with the numerical values of the results plotted are presented in Appendix B.

3.2 FLAC: Description and Capabilities

The numerical code used FLAC (Fast Lagrangian Analysis of Continua), is a two dimensional explicit finite difference code developed by Cundall[58]. This code is capable of simulating the behaviour of structures built of soil, rock or other material that may undergo plastic flow when their yield limit is reached.

The code was chosen for this investigation because:

- it allows the material to undergo large deformations; and
- it can model interfaces between two portions of the grid, taking friction into account.

Large displacements are possible due to the Lagrangian calculation scheme on which FLAC is based. It enables the grid coordinates to be updated at each time step in large strain mode[7].

The advantages over finite element methods that the code claims to have are:

- mixed discretization, as described by Marti and Cundall[59]. The term arises from the different discretization for the isotropic and the deviatoric parts of the stress and strain tensors;

- the use of full dynamic equations of motion, even when modelling static problems;
- explicit solution that can follow arbitrary non-linearity in stress and strain laws in almost the same computer time as for linear laws;
- no need to store any matrices, allowing to model large models; and
- easy numbering of elements, by row and column.

The disadvantages of this code are not very serious:

- linear simulations may take more time than with a finite element code; and
- when modelling elements with large disparities in Young's moduli, the model will take longer to converge as the solution time is determined by the ratio of the longest to the shortest natural period in the system being modelled.

The explicit calculation on which FLAC is based can be represented as in Fig. 3.1. Applying a velocity to a zone, the calculation is performed in box 2 of Fig. 3.1 were the velocities are 'frozen' during the calculation of the new stresses. The new stresses in an element do not modify the velocities of the one next to it. Once all the stresses have been calculated on the grid, the information passes to box 1 where the forces are derived from the new stresses, and by using the equations of motion the new velocities and the displacements are computed. In large strain logic the coordinates of the grid are updated. There is a maximum speed at which information can propagate across the material and the timesteps are calculated to be small enough so that information cannot physically pass from one element to the next.

The other great advantage of this code is the ability to model interfaces. This capability will allow us to model the contact between the cutting face and/or the wearflat of the tool and the rock (see Appendix C).

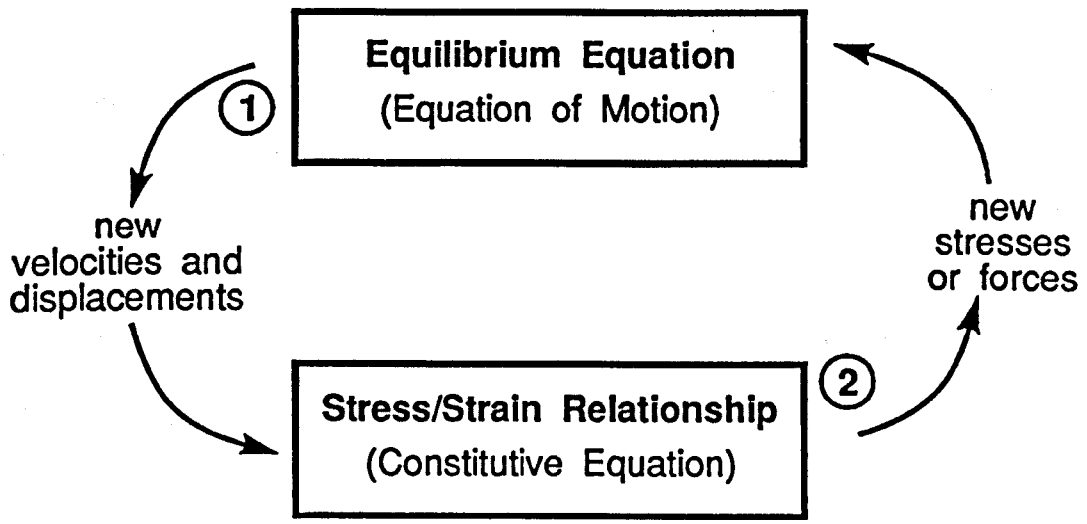

Figure 3.1: Basic explicit calculation cycle (after Itasca[7]).

The code is capable of modelling materials with the following constitutive laws:

1. null;
2. elastic, isotropic;
3. elastic, transversely isotropic;
4. Mohr-Coulomb plasticity;
5. ubiquitous joint;
6. strain-hardening/softening; and
7. double-yield (experimental).

A short discussion on the null and the Mohr-Coulomb plasticity models follows. The reader should refer to the user manual for descriptions of the other models.

Null Model. This model is used to represent material that has been excavated or removed from the model. The stresses in this zone are set to zero, automatically. It can be change back to any other type of model later in the simulation.

Mohr-Coulomb Plasticity This model only represents a material which is yielding in shear. The yield function, f_s, is given by:

$$f_s = \sigma_1 - \sigma_3(\frac{1+\sin\phi}{1-\sin\phi}) + 2c\sqrt{\frac{1+\sin\phi}{1-\sin\phi}} \tag{3.1}$$

The friction angle is ϕ, and cohesion is c. Plastic flow takes place when $f_s = 0$.

The flow rule is given by:

$$\Delta e_i^{ps} = \lambda_s \frac{\partial g_s}{\partial \sigma_i} \tag{3.2}$$

The plastic potential, g_s, for shear yielding is:

$$g_s = \sigma_1 - \sigma_3(\frac{1+\sin\tau}{1-\sin\tau}) + 2c\sqrt{\frac{1+\sin\tau}{1-\sin\tau}} \tag{3.3}$$

where τ is the dilation angle.

A perfectly plastic material was used for the modelling, with an associated flow rule, i.e. $\tau = \phi$.

3.3 Validation of the Code

The program FLAC will be validated for the problem circumstances required here against an exact analytical solution for a frictionless retaining wall. Then it will be compared with two solutions of the cutting problem. These solutions constitute lower and upper bounds for the true load on the cutter which are provided by the limit theorems of plasticity. The theorems of plasticity are defined below, according to Craig[60].

Upper bound theorem. If a mechanism of plastic failure is postulated and if, in an increment of displacement, the rate of work done by a system of external

loads is equal to the rate of dissipation of energy by the internal stresses, then failure must occur: the external load system thus constitutes an upper bound to the true collapse load.

Lower bound theorem. If a state of stress can be found which at no point reaches the failure criterion for the material and which is in equilibrium with a system of external loads, then failure cannot occur: the external load system thus constitutes a lower bound to the true failure load.

An upper and a lower bound solution can be found in literature for the mechanisms of cutting and will be presented later.

Coulomb's Retaining Wall

To validate the program, the analytical solution for a retaining wall with no friction at the wall/soil interface and a horizontal soil surface will be used. The solution for this case is exact because the upper (Coulomb, 1776) and the lower bound (Rankine, 1857) coincide.

Considering Rankine's theory for the case of a wall moving towards the soil mass, there will be lateral compression of the soil and the value of σ_x will increase until a state of plastic equilibrium is reached. For this condition σ_x becomes a maximum value and is the major principal stress σ_1. The stress σ_z, equal to the overburden pressure, is then the minor principal stress, *i.e.*

$$\sigma_3 = \rho g z \tag{3.4}$$

where ρ is the density of the material, g gravity and z depth. In this case the horizontal stress is defined by:

$$\sigma_1 = \sigma_3\left(\frac{1+\sin\phi}{1-\sin\phi}\right) + 2c\sqrt{\frac{1+\sin\phi}{1-\sin\phi}} \tag{3.5}$$

The Rankine solution predicts the failure plane to be inclined relative to the

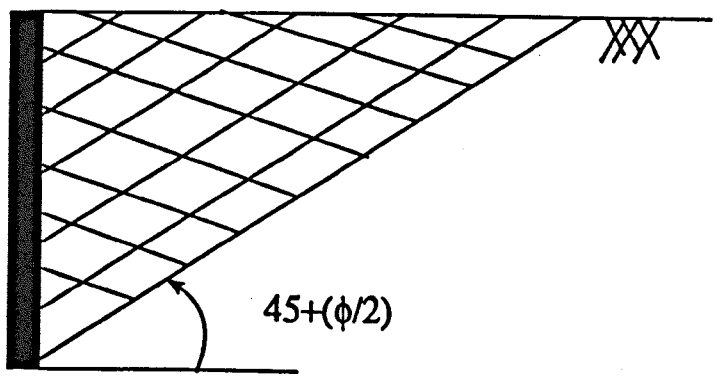

Figure 3.2: Shear plane predicted by Coulomb for a retaining wall.

axis of σ_3 from the following equation:

$$\alpha = \frac{\pi}{4} - \frac{\phi}{2} \tag{3.6}$$

The geometry of the numerical model of the retaining wall is presented in Fig. 3.3. The vertical wall/soil contact is modelled without friction and three of the domain boundaries are fixed. The top surface is free.

The properties used for the simulations are presented in Table 3.1.

After 1500 steps of simulation, the numerical model has converged as shown in Fig. 3.5. When plotting the velocity vectors of the grid, an idea of the shear plane location and shape can be determined. As can be seen in Fig. 3.6, the velocity vectors next to the wall have an orientation of about 30° with respect to the horizontal, as predicted by Coulomb's and Rankine's solutions. The failure surface appears to be a straight line.

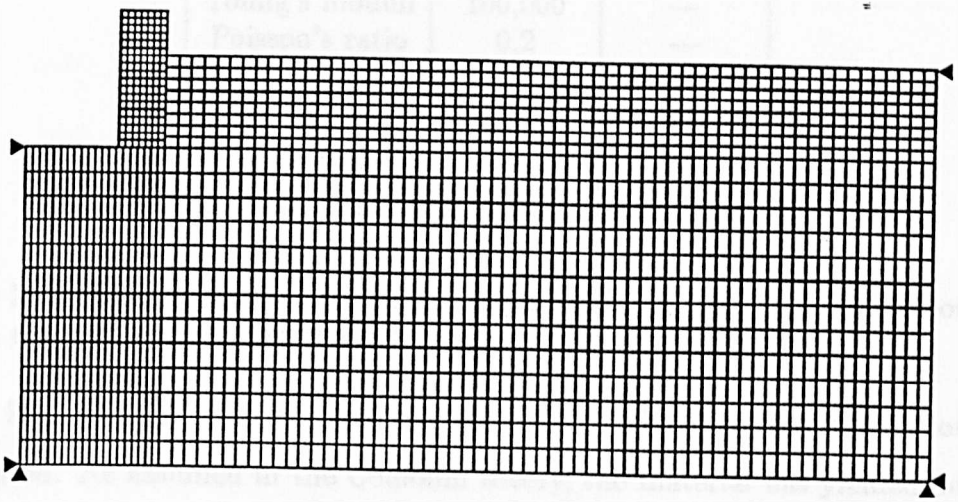

Figure 3.3: Grid for the modelling of the retaining wall.

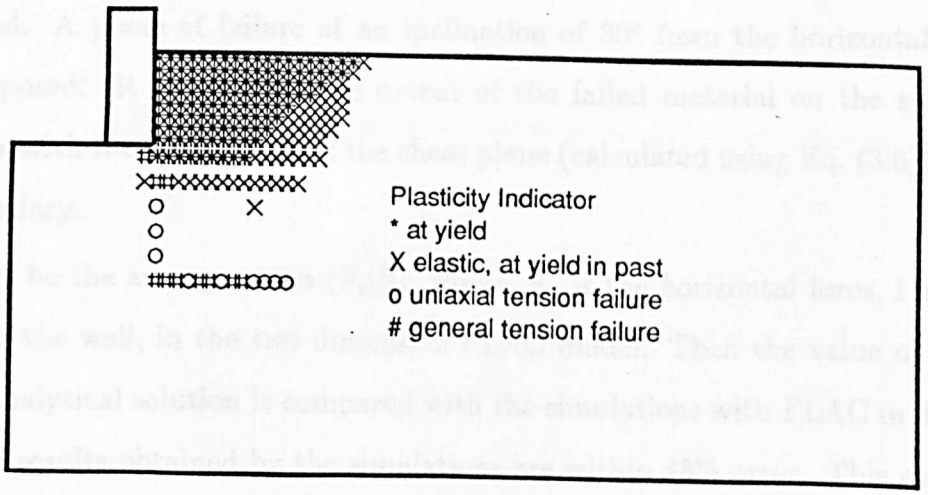

Figure 3.4: Plastic zones developed in Coulomb's retaining wall simulation.

Parameter	*Numerical*	*Analytical*
ϕ	30°	30°
c	10	10
Young's moduli	100,000	—
Poisson's ratio	0.2	—
ψ	0°	0°
θ	0°	0°
ρ (g/m^3)	0	0
g (m/s^2)	0	0

Table 3.1: Parameters used for simulating a retaining wall with no friction between the wall surface and the soil.

In Fig. 3.4, the yield zones of the material predicted by the simulation are presented. As assumed in the Coulomb theory, the material has yielded behind the wall. In this figure, it can also be noticed that a tensile crack develops from the foot of the wall downwards. This feature can be explained because the material model had very little tensile strength and, as the wall moved, the element underneath the wall is stretched in an opening mode, failing in tension. In Fig. 3.7, the initial boundary for the simulation and the boundary with the displacements of the elements magnified ($\approx$ 65 times larger) after 1500 steps is presented. A plane of failure at an inclination of 30° from the horizontal was superimposed. It shows that the extent of the failed material on the surface coincides with the intersection of the shear plane (calculated using Eq. (3.6)) and the boundary.

Let σ_1 be the average stress (F_x/l), where, F_x is the horizontal force, l is the height of the wall, in the two dimension FLAC model. Then the value of σ_1/c for the analytical solution is compared with the simulations with FLAC in Table 3.2. The results obtained by the simulations are within 15% error. This can be improved by modifying the density of the grid. This validation suggests that the code is accurate enough for the simulations required in this research.

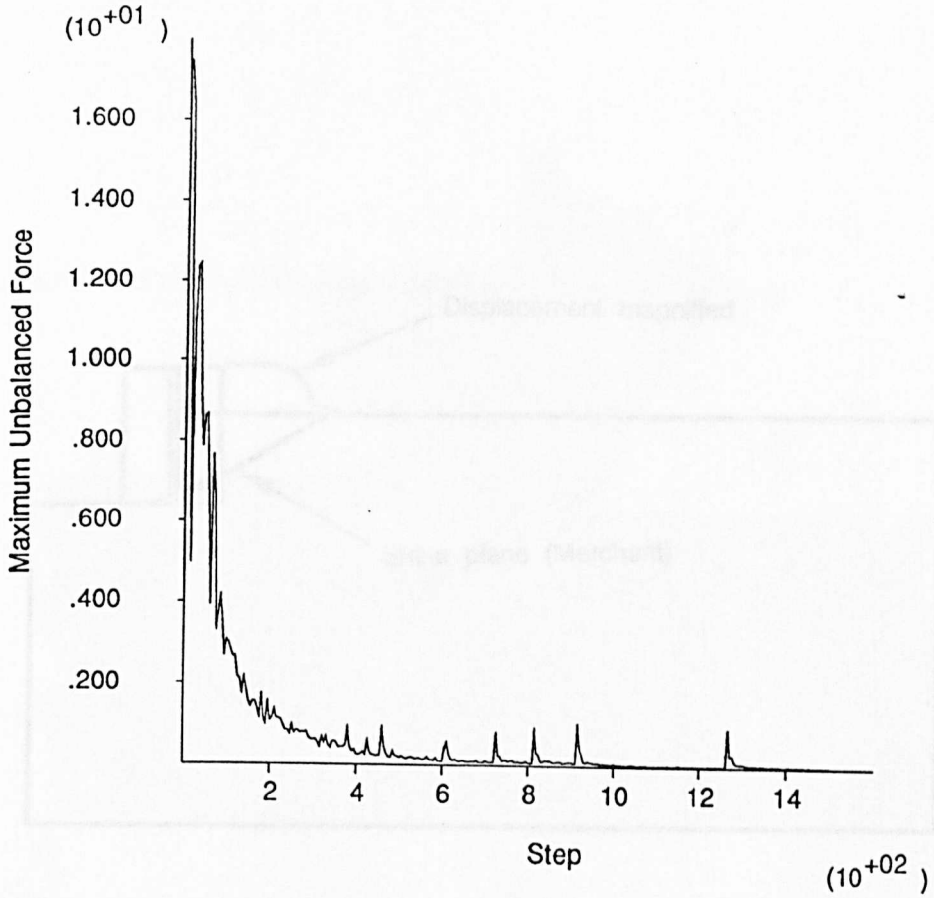

Figure 3.5: Unbalance force history of the retaining wall simulation (every 5 steps).

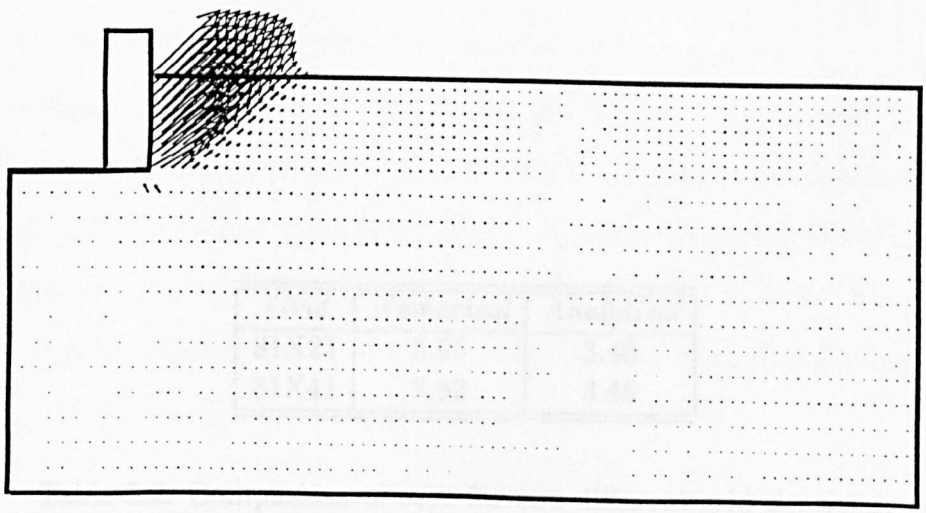

Figure 3.6: Velocity vectors retaining wall model (after 1500 steps).

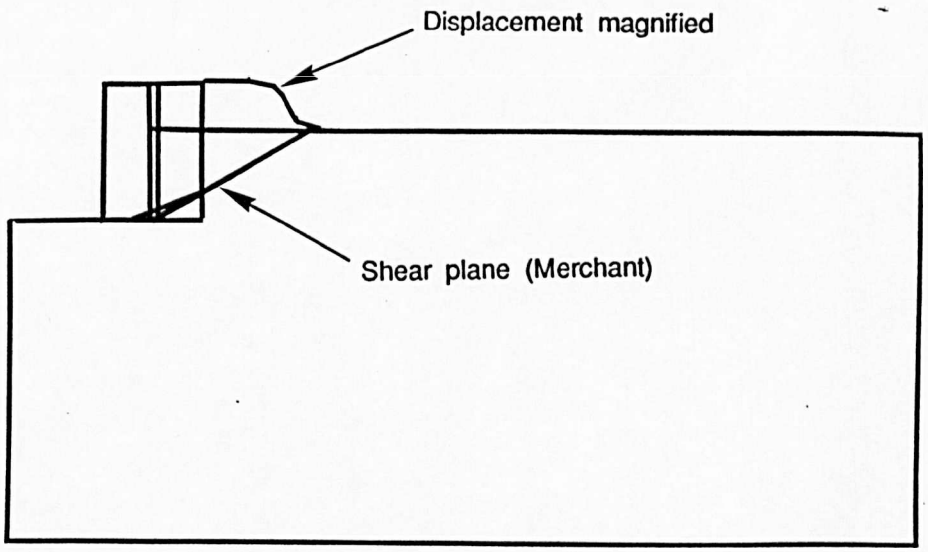

Figure 3.7: Initial boundary and magnified displacements at the boundary. Shear failure plane at 30° superimposed.

Grid	*Numerical*	*Analytical*
81X21	3.96	3.46
81X41	3.92	3.46

Table 3.2: Comparison of σ_1/c for two different grid densities.

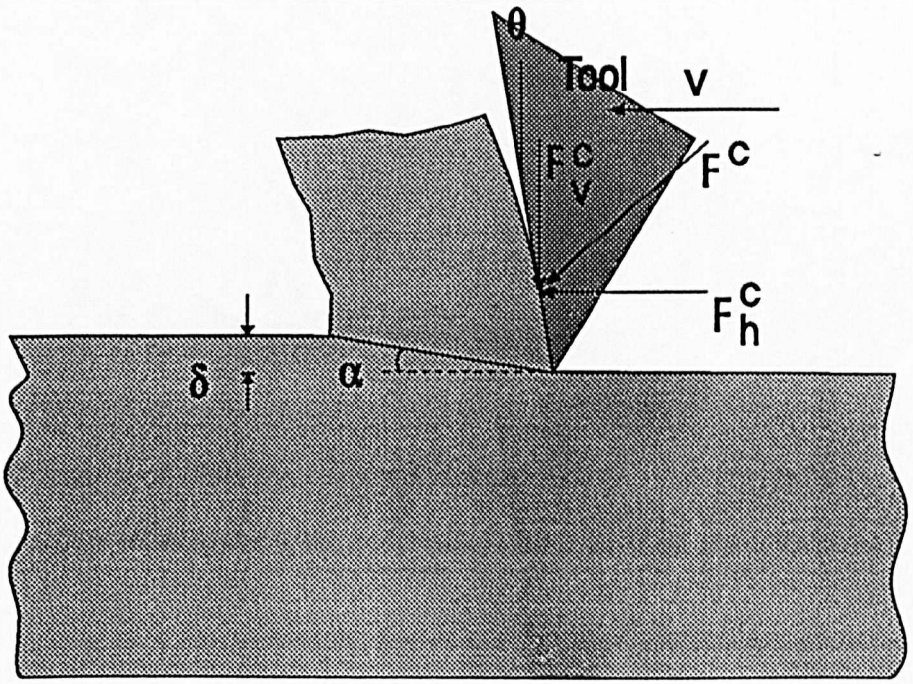

Figure 3.8: Simple flow mechanism (after Merchant[8]).

3.4 Sharp Cutter Model

In order to validate the numerical simulation of the sharp cutter mechanism, the upper and lower bound solutions for the true load on the cutter will be compared with the results obtained by numerical experiments.

A solution derived by Merchant[8] for the machining of metals, which assumes that the material is rigid perfectly plastic with a cohesion c and internal friction angle ϕ, will be taken as the upper bound. Fig. 3.8 illustrates the simple flow mechanism considered by Merchant[8]. It shows a cutter moving at a constant velocity v and constant depth of cut δ. The specific energy of cutting ϵ from Merchant[8] can be expressed as[61]:

$$\frac{\epsilon}{c} = \frac{2\cos\phi\cos(\theta+\psi)}{1-\sin(\theta+\psi+\phi)} \tag{3.7}$$

where ϵ is the specific energy of cutting as described in Section 2.3, θ the rake angle (taken as positive if the cutter is inclined forward) and ψ the interface

friction angle.

The inclination of the shear plane with respect to the direction of motion, corresponding to Eq. (3.7), is given by

$$\alpha = \frac{\pi}{4} - \frac{\theta + \psi + \phi}{2} \tag{3.8}$$

Equations 3.7 and 3.8 indicate that the Merchant failure mechanism can only be constructed for:

$$\theta < \frac{\pi}{2} - (\phi + \psi) \tag{3.9}$$

This constraint is usually met since the rake angle for PDC cutters is typically between 15° and 20°[61].

The lower bound solution for the limit force on a single PDC cutter working at atmospheric pressure conditions was reported by Drescher[62]. It assumes the cutter to be working in plane strain conditions and moving horizontally with a constant speed. The rock is modelled as a weightless rigid-perfectly plastic solid whose flow rule is associated with the Mohr-Coulomb yield criterion.

The two solutions of the upper bound (Merchant[8]) and the lower bound (Drescher[62]) will be used to validate the numerical experiments.

3.4.1 Model Description

Grid

The grid dimensions for the cutting model is taken to be 5 times greater than the depth of cut in the direction of motion of the cutter and approximately 3 times the depth of cut in the direction perpendicular to the motion of the tool. This ensures that the failure zones are inside the grid boundaries. Fig. 3.9 presents the grid geometry and density used for the validation of the code. The optimum number of elements (41x21 at the start of the grid generation process) was determined by using various mesh densities; this number of elements provides accurate results in a reasonable time.

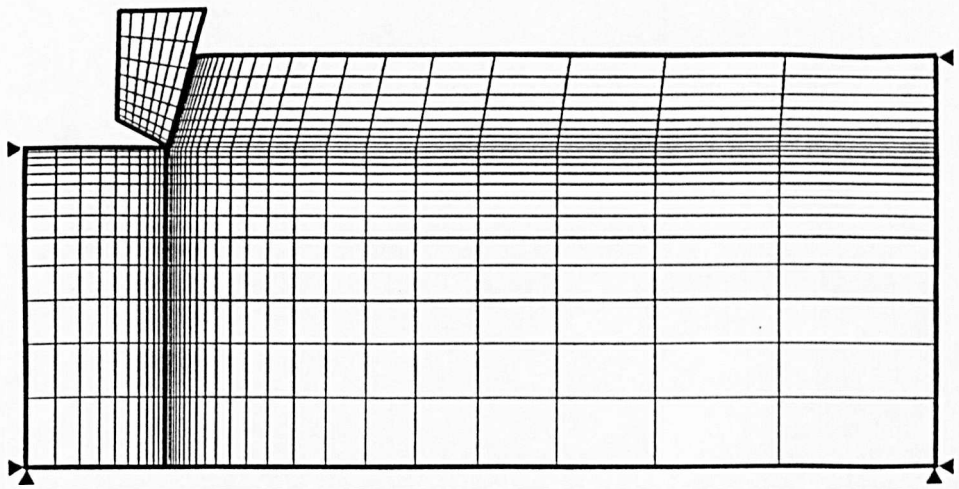

Figure 3.9: Grid geometry for the sharp cutter problem.

Material Properties

The model simulates a weightless rigid-perfectly plastic material with a Mohr-Coulomb yield function. It is assumed to be deforming in plane strain conditions. The tool is modelled as a linear elastic material.

The material properties assigned to the model were chosen considering that the behaviour should approach that of a rigid plastic material (*i.e.* the ratio of c/E very small). Table 3.3 presents these properties. The tool is 10 times stiffer than the rock and for the rock E/c=10,000. This ratio is very large compared to the real values for rocks (≈600). These properties were chosen to approach the condition pertaining to a rigid-perfectly plastic material. The density assigned to the rock and to the tool is only used for numerical simulation, as there is no gravity force.

The upper bound and the lower bound solutions are defined for weightless material in which the only parameters relevant for the determination of ϵ are

Property	*Tool*	*Rock*
Young's modulus(MPa)	1,000,000	100,000
Poisson's ratio	0.2	0.2
density(g/m^3)	1e-3	1e-3
cohesion(MPa)	—	10
tensile strength(MPa)	—	10

Table 3.3: Properties used in the numerical simulation of a sharp cutter.

those represented in Eq. (3.7). In the case of the PDC cutting face, experimental evidence[24] shows that the interface friction angle is around 10° to 18°. The friction angles selected for the simulations were 10° and 20°.

Boundary Conditions

The grid was fixed on three sides as shown in Fig. 3.9. The top surface was left free, simulating atmospheric conditions. No initial confining stresses were imposed to the boundary. The tool had a rake angle of 16.7° and a constant velocity in the horizontal direction of 8E-6 mm/step.

'Time Steps'

The simulations were performed to a prescribed number of time steps. In this way, all the simulations will stop when the cutter had moved a specific distance. For this investigation the number of steps was 1500, giving a displacement of 1500x8E-6= 0.012 mm. The size of the element on the grid closest to the tool interface was of 0.011 mm, which means that the tool will displace more than one length of the element, but this is possible with FLAC when using large strain logic.

The history of the maximum unbalanced force (Fig. 3.10) showed in all the cases that the simulation had converged.

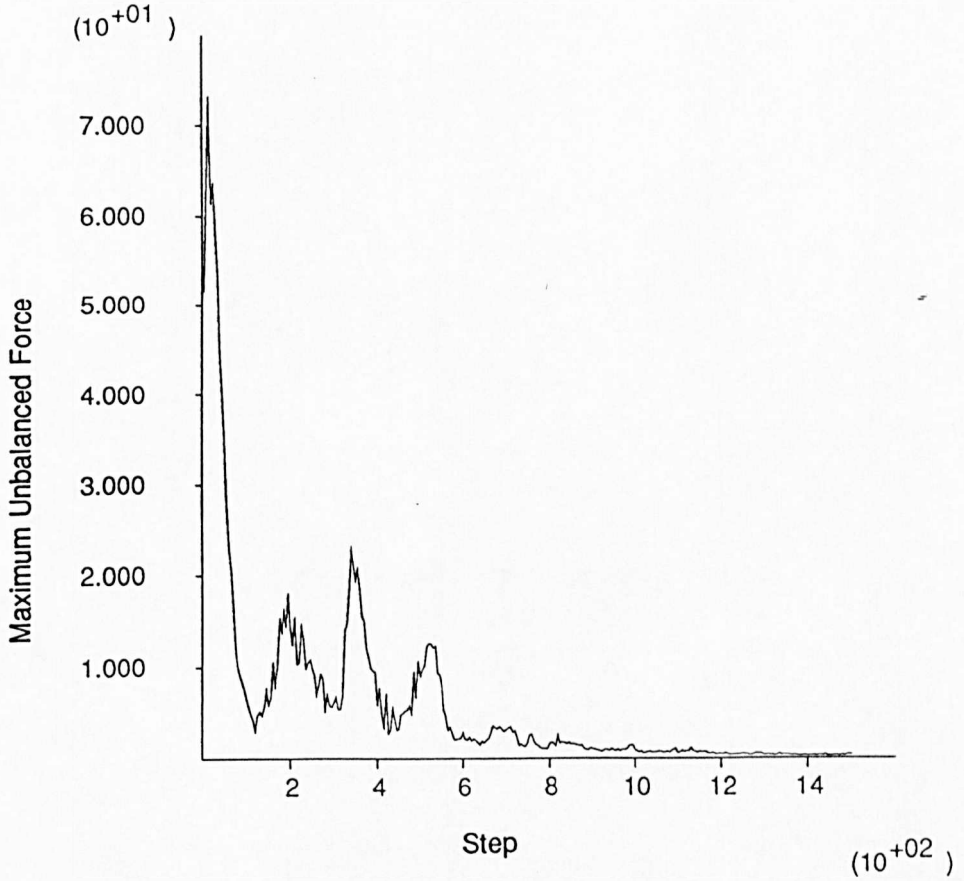

Figure 3.10: Example of maximum unbalance force history for the sharp cutter problem.

3.4.2 Parametric Investigation

In order to validate the numerical model, a number of experiments were performed by varying the parameters relevant to the determination of the specific energy. These are:

- internal friction angle of the material;
- tool/rock interface friction angle; and
- tool rake angle.

The depth of cut was also varied for the model of the sharp cutter even though it is not specified as a parameter in the calculation of ϵ. It was done to assess the quality of the numerical code, by checking if ϵ is modified by a change in discretization, and to obtain data for further analysis of the blunt cutter problem.

The parametric study program can be summarized in Table 3.4.

Model	ψ	ϕ	θ	δ (mm)
1	10°	10°	16.7°	1.00
2	10°	15°	16.7°	1.00
3	10°	20°	16.7°	1.00
4	10°	25°	16.7°	1.00
5	10°	30°	16.7°	1.00
6	10°	35°	16.7°	1.00
7	20°	10°	16.7°	1.00
8	20°	15°	16.7°	1.00
9	20°	20°	16.7°	1.00
10	20°	25°	16.7°	1.00
11	20°	30°	16.7°	1.00
12	20°	35°	16.7°	1.00
13	10°	30°	20°	1.00
14	10°	30°	10°	1.00
15	10°	30°	16.7°	0.25
16	10°	30°	16.7°	0.50
17	10°	30°	16.7°	0.75
18	10°	30°	16.7°	1.00
19	10°	30°	16.7°	1.25
20	10°	30°	16.7°	1.50

Table 3.4: Summary of parametric investigations on sharp cutter.

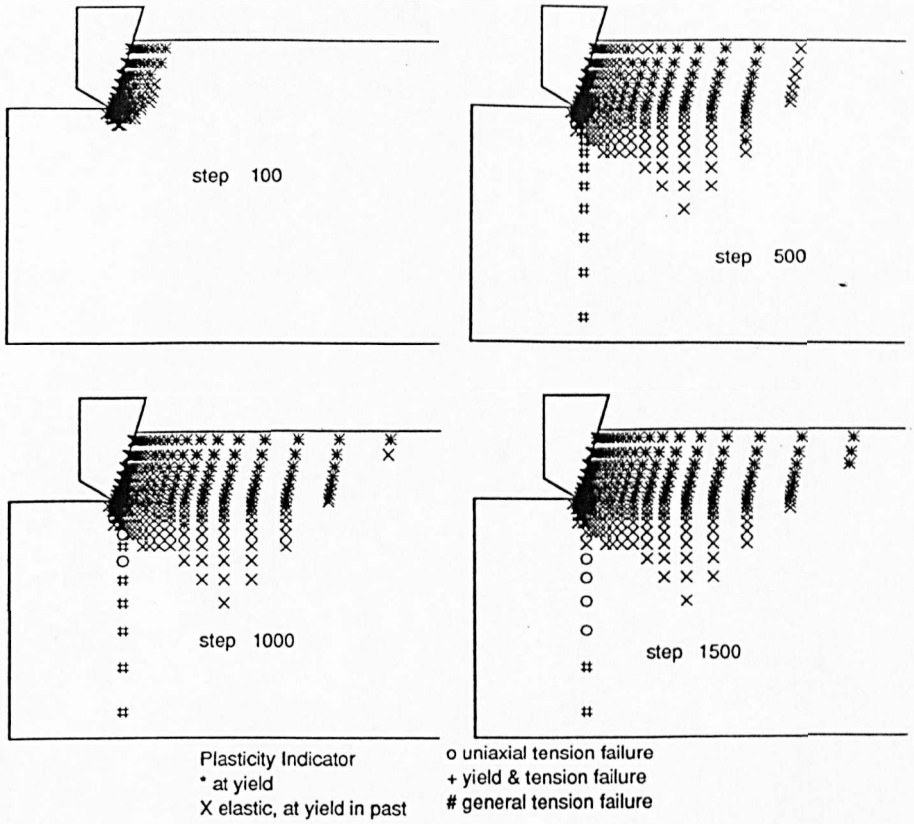

Figure 3.11: Sequence of failure zones for the sharp cutter model.

3.4.3 Analysis of the Results

Failure Mechanism

The observed failure mechanisms in the sharp cutting simulations can be illustrated with the sequence in Fig. 3.11. The figure shows the material in contact with the tool yields very quickly (after only 6 'time' steps) due to the rigid-plastic behaviour of the model, then it starts to develop a yield zone in front of the cutter. The boundary of the yield zone forms an arc from the tip of the cutter upwards, touching the surface at a point that can be estimated from the Merchant's[8] solution (Eq. (3.8)). In Fig. 3.11 a tension crack can be seen developing from the corner below the tip of the cutter. This can be explained, as in the modelling of the retaining wall, by the fact that the elements in front of the tool and the elements behind the tool have opposite relative displacement, creating a fracture in opening mode. A confining pressure applied to the lateral boundaries could

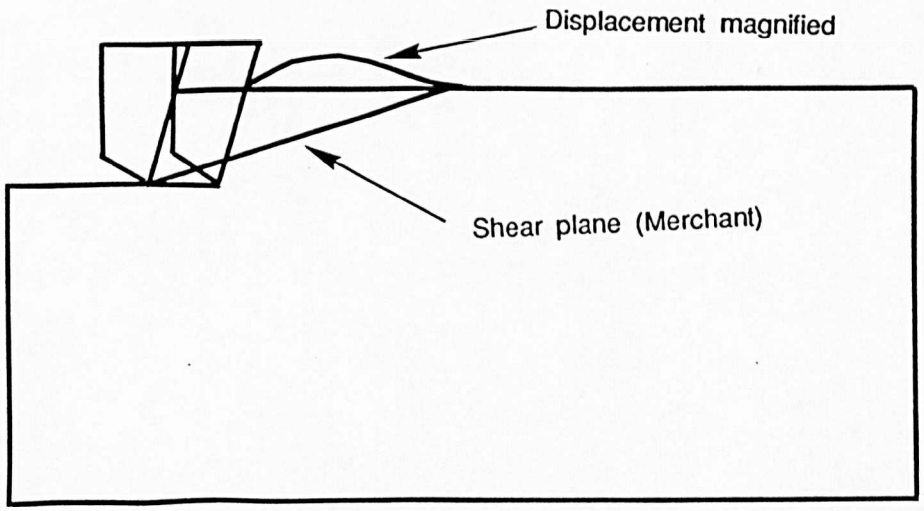

Figure 3.12: Displacements of the boundary magnified with Merchant's shear plane prediction superimposed.

eliminate this tensile crack, but in this investigation this crack does not affect the results, as the interest lies in the shear failure in front of the cutter.

Internal Friction Angle

After 1500 steps of simulation, the tool has moved a distance of 0.012 mm. Fig. 3.12 shows the original boundary and the boundary after the simulation with the displacements magnified. A shear plane with an inclination α=30° has been superimposed, where the boundary displaced approximately intersects the shear plane predicted by Eq. (3.6). In Fig. 3.14, the velocity of the tool has been set to 0, to emphasize the velocity in the material. These vectors can give an idea of the shear plane location. The friction at the interface causes the failure surface to be curved near the bottom of the cutter, but then it can be approximated to a line until it reaches the surface.

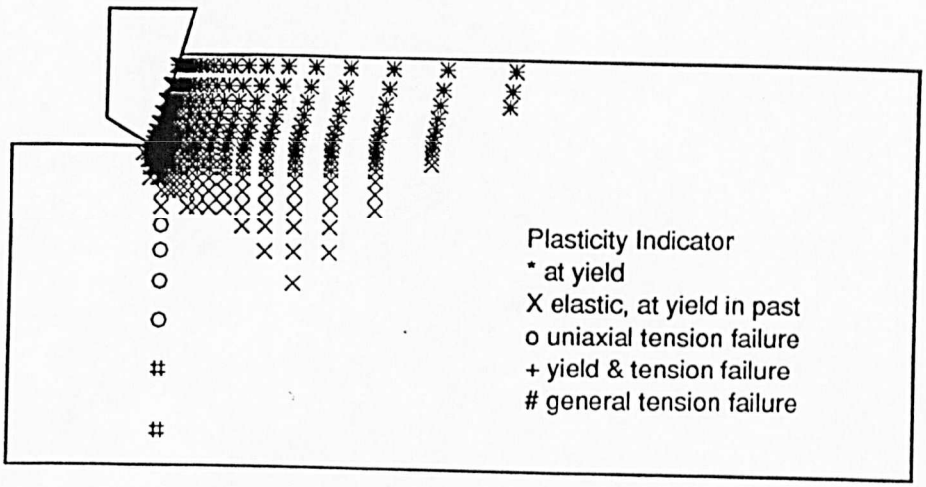

Figure 3.13: Plastic zones after 1500 steps in the sharp cutter problem.

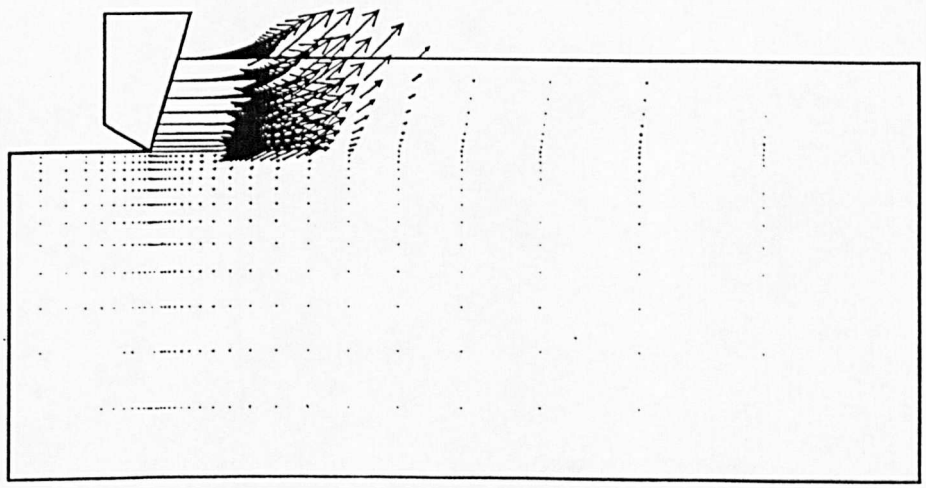

Figure 3.14: Velocity vectors after the sharp cutter has moved 0.012 mm.

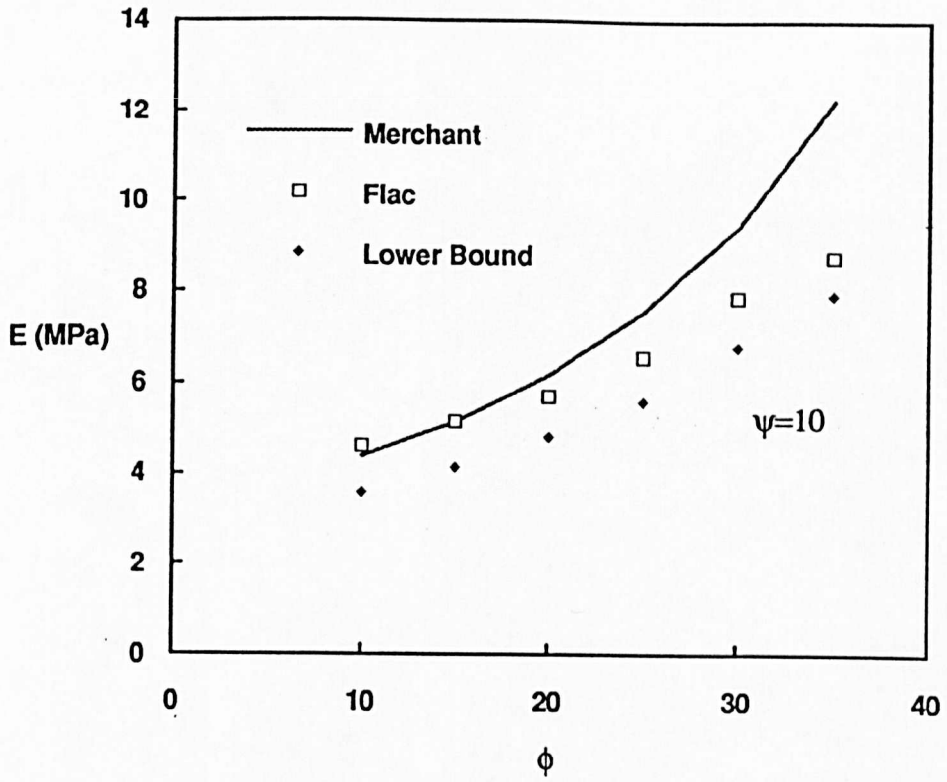

Figure 3.15: Specific energy ϵ versus friction angle ϕ for ψ=10°.

The values of ϵ/c from the results of the simulations performed varying the internal friction angle of the material are plotted against ϕ, in Fig. 3.15 and Fig. 3.16, for tool/rock interface friction angles of 10° and 20° respectively. The graphs show that the numerical predictions are in between the upper and the lower bound solutions having the same trend as the lower bound, which starts flattening after 35° friction angle. The upper bound tends to go steadily upwards.

Rake Angle

Two numerical experiments were performed by varying the rake angle of the tool. The first was with a rake angle of 10° and the second of 20°. They were designed to corroborate Eq. (3.8) as being an approximation of the shear plane location. The results, for 20° rake angle, can be shown in Fig. 3.17, where the boundary displacement has been magnified. A line representing the shear plane at an angle of inclination calculated by Eq. (3.8) has been superimposed. As for the previous

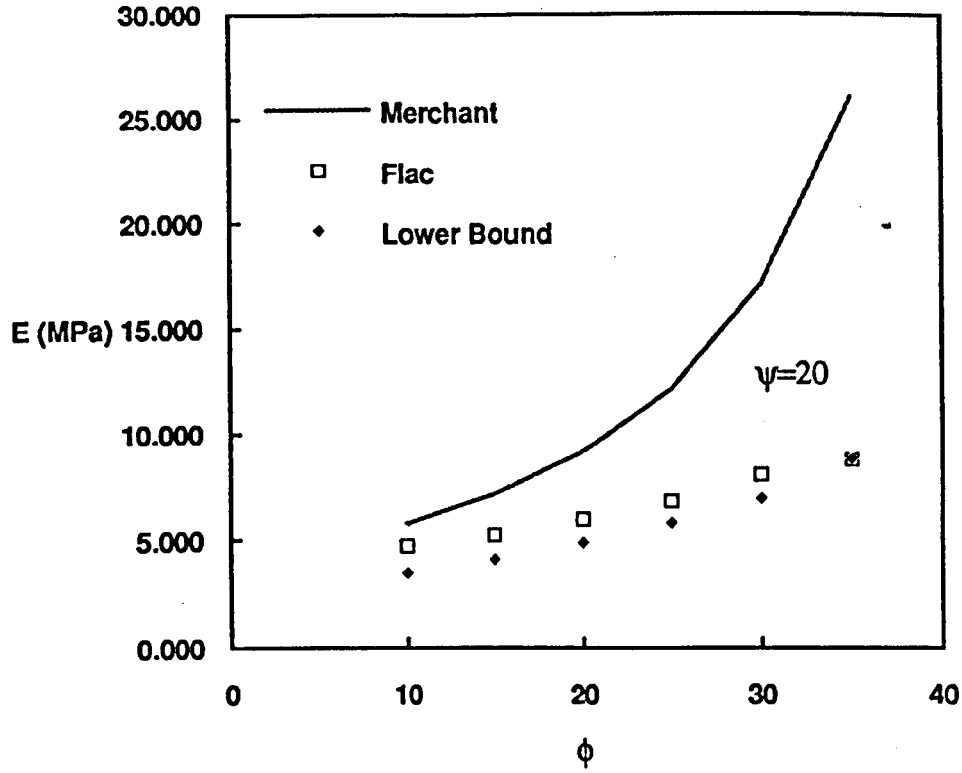

Figure 3.16: Specific energy ϵ versus friction angle ϕ for ψ=20°.

rake angle (16.7°), the intersection of the shear plane with the boundary marks the length of surface deformation. In Fig. 3.18, the velocity vectors are plotted. In this case, due to a greater rake angle, the velocity vectors near the tool have near horizontal direction, but then they change direction towards the surface. The results for the 10° rake angle are as expected. The displacement (Fig. 3.19) and the velocity vectors (Fig. 3.20) plots show a smaller zone of failure, with a steeper shear plane. For rake angles higher than 20°, the Merchant solution starts to deviate as the material sticks to the cutting face and no slip occurs at the interface.

Depth of Cut

The simulations changing the depth of cut were conducted mainly to check the quality of the simulations, as for different discretization the values of ϵ obtained should be the same. As predicted, the results did not show significant deviations

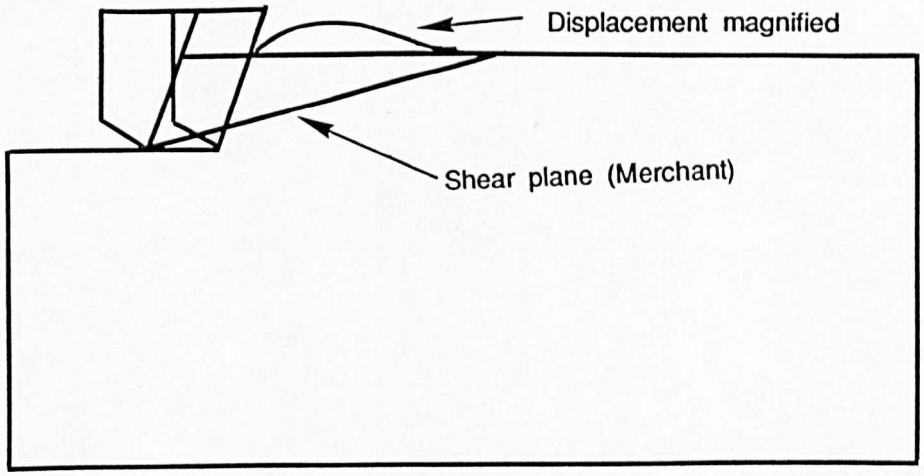

Figure 3.17: Boundary displacement magnified for a tool rake angle of 20°.

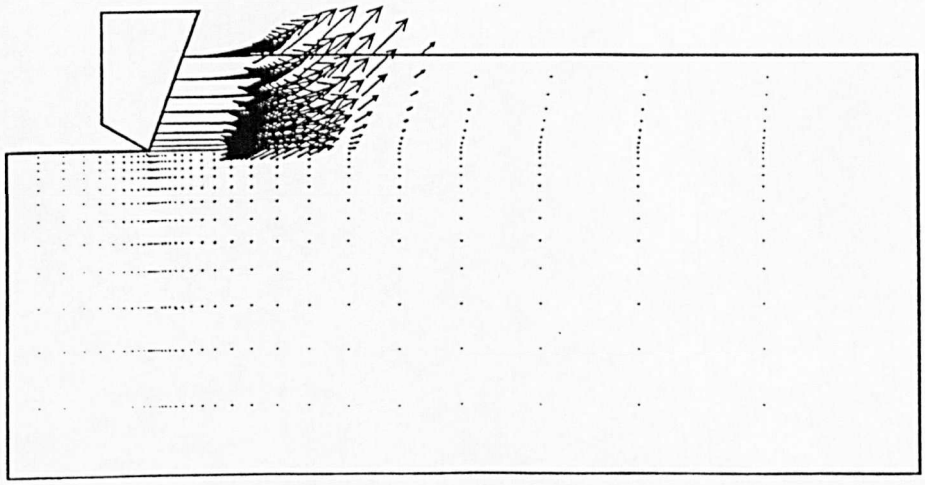

Figure 3.18: Velocity vectors for a tool rake angle of 20°.

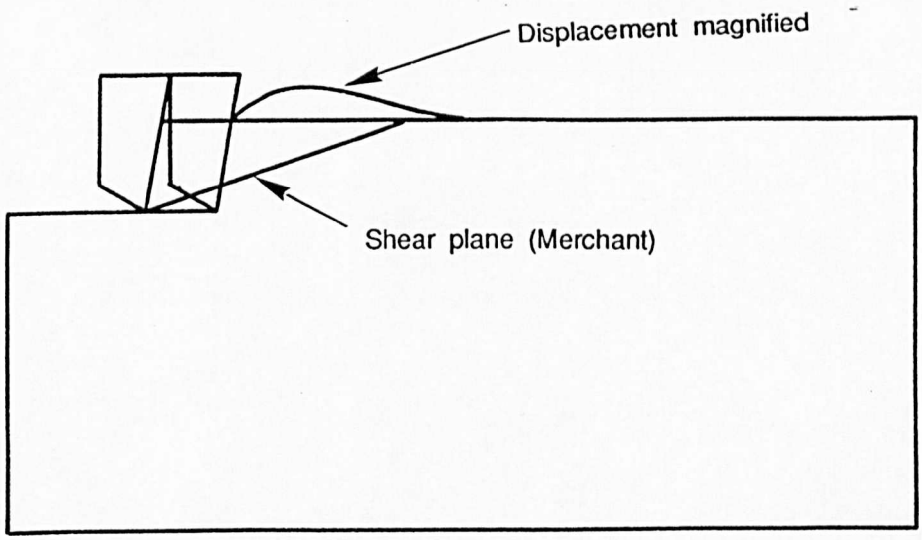

Figure 3.19: Boundary displacement magnified for a tool rake angle of 10°.

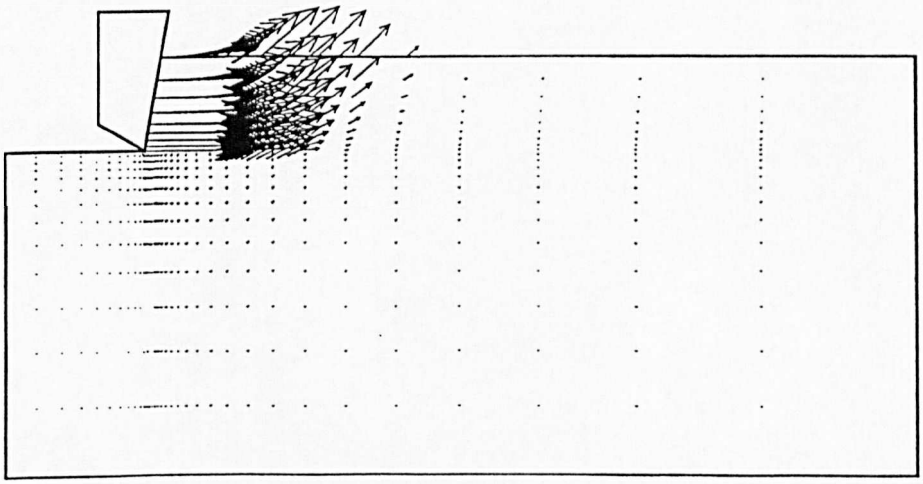

Figure 3.20: Velocity vectors for a tool rake angle of 10°.

Depth (mm)	ϵ *(MPa)*
0.25	8.16
0.50	7.78
0.75	7.77
1.00	7.36
1.25	7.86
1.50	8.16
Average	7.85
St.Dev.	0.29

Table 3.5: Values of ϵ obtained for different depths of cut.

in ϵ. Table 3.5 present the values of ϵ for each depth of cut, their average and standard deviation. As the table shows, all the values of ϵ are within 3.5% of the average.

3.5 Wearflat Contact

As for the sharp cutter problem, the main purpose of the numerical modelling of the wearflat contact is to validate the code for the simulation of the blunt cutter tool.

The wearflat contact problem has an upper and a lower bound solution. The lower bound is the same one described by Drescher[62] and used in the sharp cutter problem, but the upper bound is different, as the value of θ does not comply with the restriction given by Eq. (3.9).

There are two possible states at the interface between the cutter face and the rock:

1. the material flows forwards;

2. the material flows backwards.

When modelling the wearflat, the rake angle of the tool is much greater than 20°, at which the material sticks to the tool breaking the flow rule for the Merchant

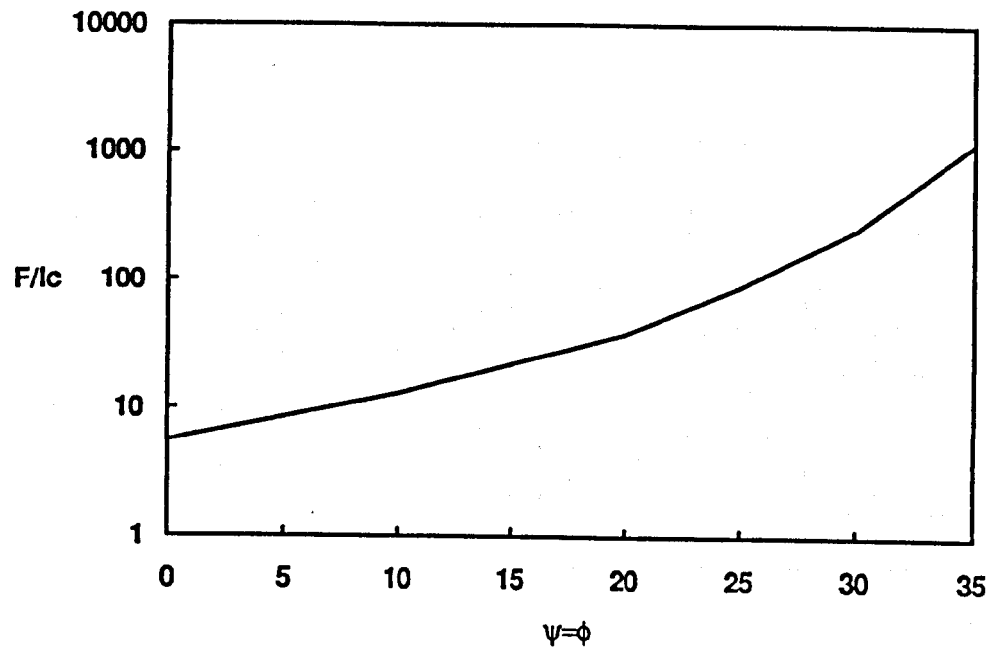

Figure 3.21: Upper bound plot for the wearflat contact (after Detournay[9]).

solution (case 1). In the second case, the material sticks to the wearflat of the tool creating a layer of material in between the tool and the rock, creating what is called bit balling.

An upper bound solution was derived by Detournay[9] in which the flow of the material is backwards. This upper bound is plotted in Fig. 3.21, where F/lc is the total stress normalized by the cohesion, c.

3.5.1 Model Description

Grid Geometry

The geometry for modelling the wearflat contact problem is simpler than that of the sharp cutter. The grid size used for the investigation of the wearflat problem was 21x21 elements. Some of the elements have been eliminated (assigning to them the null model), to separate the grid in two. In Fig. 3.22, the geometry, dimensions and discretization of the grid are shown. The lengths for the wearflat

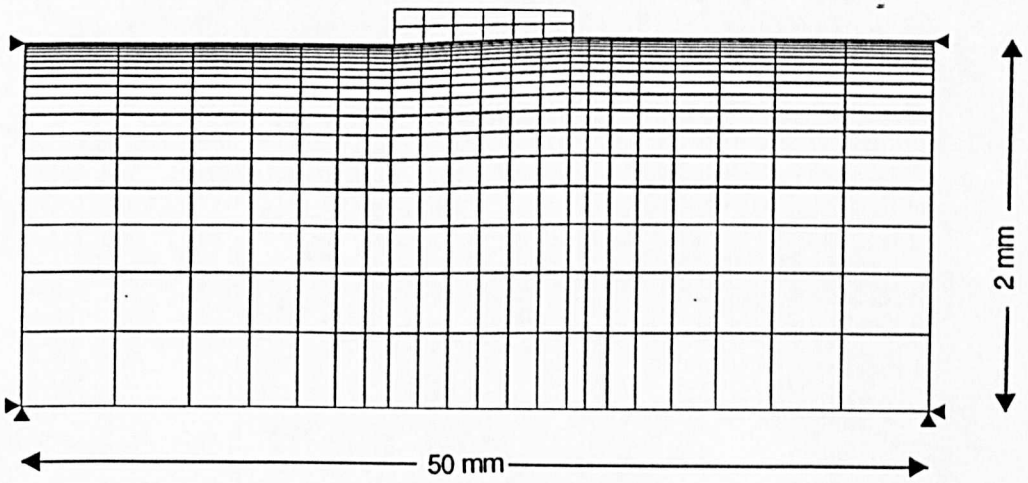

Figure 3.22: Geometry and dimensions of the model of wearflat contact.

(represented by a plate) were taken as 0.5 mm and 0.25 mm. These dimensions gave a good discretization without needing to add more elements to the grid, which will increase the calculation time.

Material Properties

The simulations approximate a weightless rigid-perfectly plastic material with a Mohr-Coulomb yield function. It is assumed to be deforming in plane strain conditions. The plate representing the wearflat is modelled as a linear elastic material.

The same material properties as for the sharp cutter are used in this investigation (Table 3.3). For this case, the values of the parameters of E and c are most important, as for a small E/c ratio, the material will not yield under the wearflat.

Boundary Conditions

The grid was fixed on three sides as shown in Fig. 3.22. The top surface was left free, simulating atmospheric conditions. No initial confining stresses were imposed on the boundary. The plate that represents the wearflat contact had a prescribed velocity in the horizontal direction of 8E-6 mm/step. This velocity is the same as for the sharp cutter problem since the two problems have to be combined later.

'Time Steps'

The number of steps required for the problem to converge (about 600) is much less than for the sharp cutter, but more steps were required to achieve failure along the total length of the plate and also to obtain the same displacement as in the previous model. A typical history plot for the maximum unbalance force is presented in Fig. 3.23.

3.5.2 Parametric Investigation

The parametric investigation for the wearflat contact will include the study of the variation of the total average stress (normalized by cohesion) when $\phi = \psi$, the effect on the total force due to wearflat contact length and the effect of the wearflat contact angle. The parametric study for the wearflat contact is summarized in Table 3.6.

3.5.3 Analysis of Results

Failure Mechanism

Failure was observed after a few timesteps due to the rigid-plastic characteristics given to the model material. Then some elements on the material in the area near the centre of the contact, started compacting surrounded by yielded material. The compacted zone under the wearflat is confined by the surrounding plastic

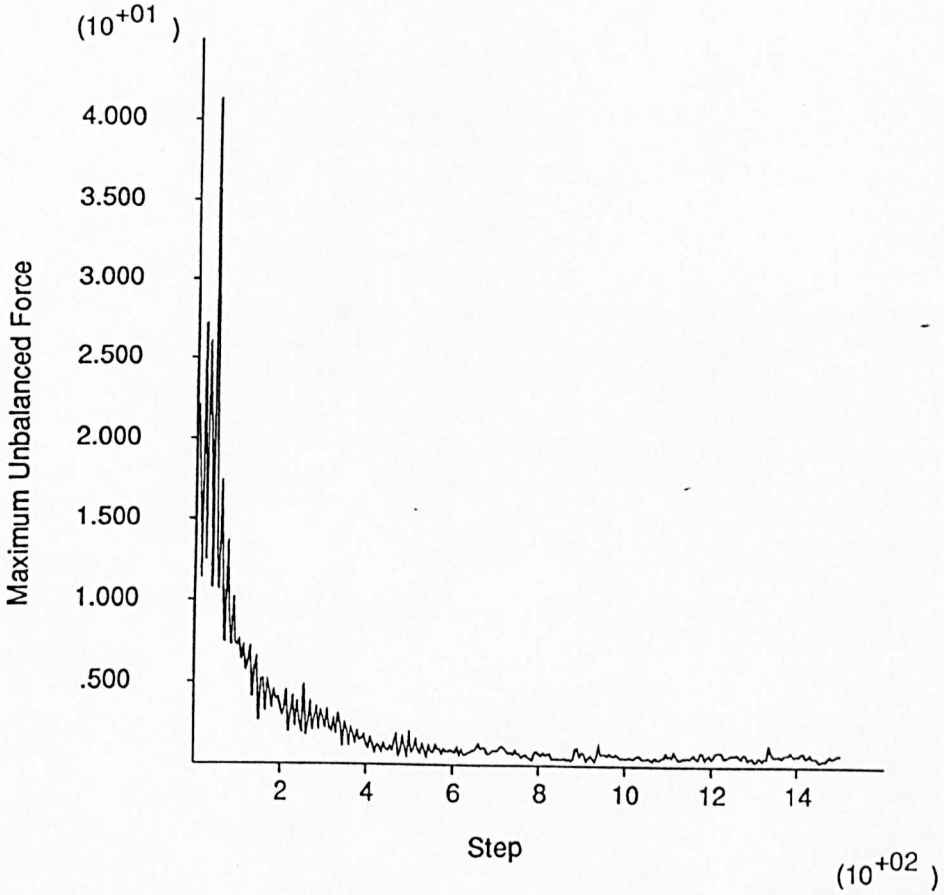

Figure 3.23: History of the maximum unbalanced force for the wearflat problem (every 5 steps).

ϕ	ψ	*Wearflat length* (mm)	*Inclination* (°)
10 10	10	0.50	3
15	15	0.50	3
20	20	0.50	3
25	25	0.50	3
30	30	0.50	3
35	35	0.50	3
10	10	0.25	3
15	15	0.25	3
20	20	0.25	3
25	25	0.25	3
30	30	0.25	3
35	35	0.25	3
30	30	0.25	0
30	30	0.25	1
30	30	0.25	2
30	30	0.25	5

Table 3.6: Summary of the parameters studied for the wearflat contact.

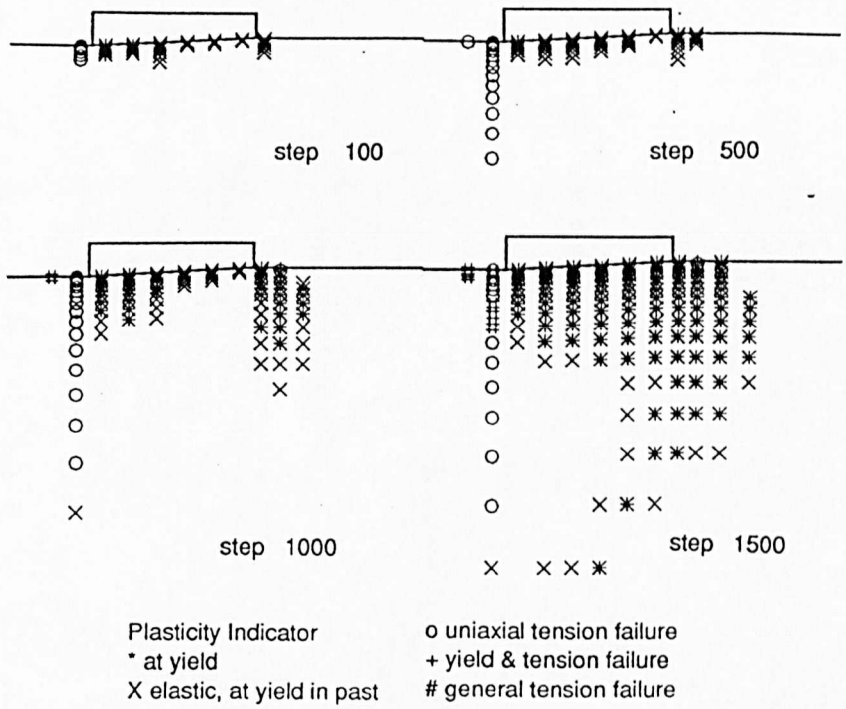

Figure 3.24: Predicted sequence of failure for the wearflat contact problem.

zone, increasing its yield strength. After a large displacement of the wearflat (depending on grid discretization), this zone yields again giving the maximum values for the shear stress at the interface. Fig. 3.24 presents a sequence of the failure process as predicted by the simulation.

Friction Angle

The numerical experiments performed to analyze the effect of the friction angle on the contact stress were considered for the cases where $\phi = \psi$, as it is assumed that the friction at this interface is the friction angle of the material. This is true for the cases when the material sticks to the rough surface of the wearflat, creating an interface layer.

To verify the quality of the code, the length of the wearflat was changed for different models 1.00 mm, 0.50 mm and 0.25 mm (different discretization).

The numerical experiments varying the friction angle ($\psi = \phi$) and the length of

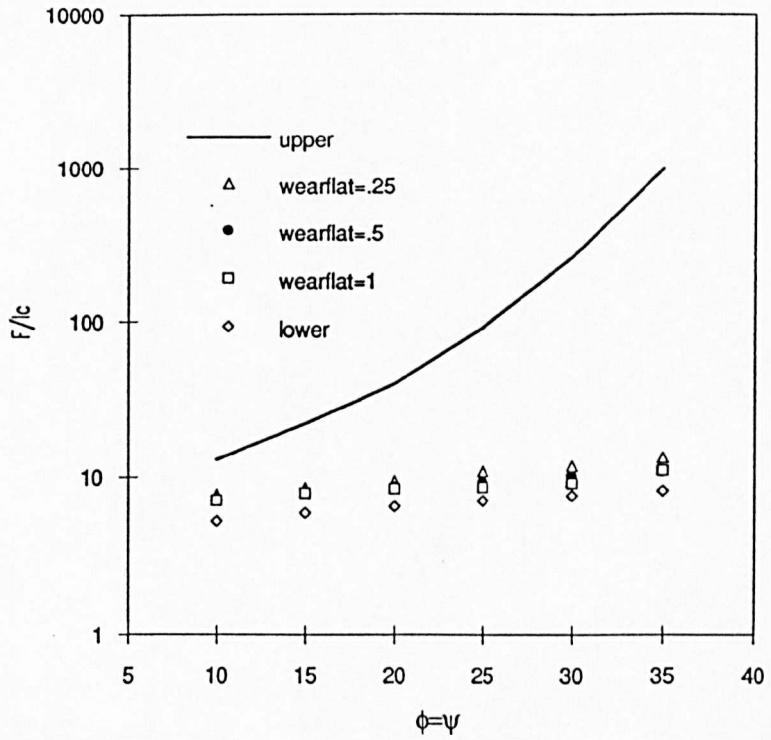

Figure 3.25: Normalized contact stress against variation of $\phi = \psi$, for different lengths of wearflat.

the wearflat show that the total normalized contact stress, F^f/lc, falls in between the upper and lower bound plasticity solutions, as shown in Fig. 3.25 for the two different lengths of wearflat. The graph also proves that the discretization for the models was adequate.

Inclination of the Wearflat Contact

The inclination of the wearflat with respect to the horizontal has to be modelled to determine the influence of this parameter on the contact stress. Four different angles (0^o, 1^o, 2^o and 5^o) were simulated in addition to the 3^o used in previous simulations. In Fig. 3.26, the results of these experiments are plotted. For an inclination of 0^o, the contact stress is equal to 0 as expected, the tool only moves horizontally at a constant depth of cut, which means that there is no normal force applied. As the angle increases, the contact stress also increases with a linear

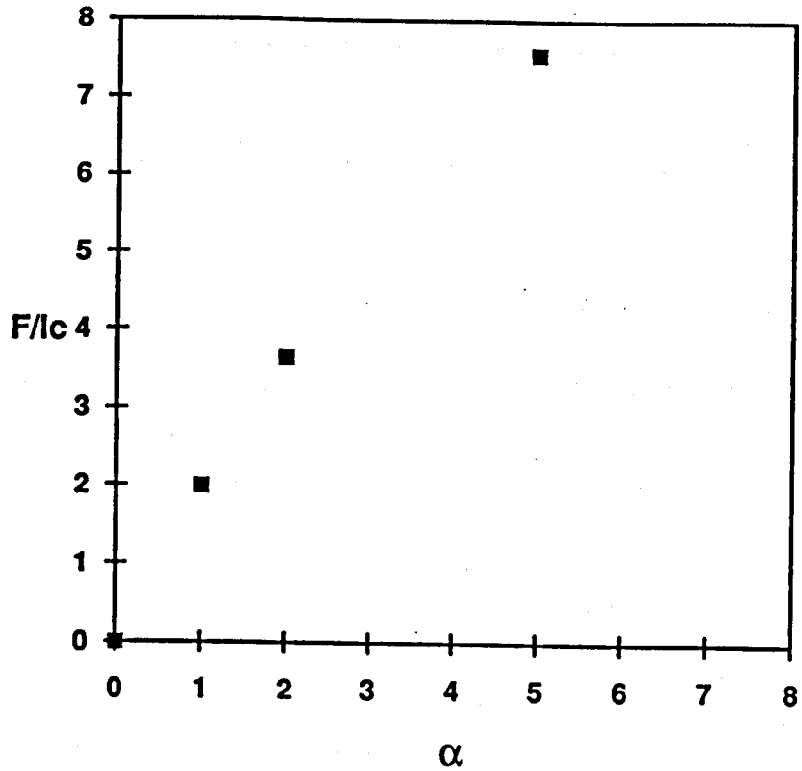

Figure 3.26: Normalized contact stress against inclination of the wearflat.

trend. From Fig. 3.27, it can be seem that, under the wearflat, the material yields in larger areas as the angle of the wearflat increases.

3.6 Blunt Cutter Model

The blunt cutter model experiments will provide with an insight on the cutter mechanisms and will complete the data needed for the validation of the model. The validation can be achieved by:

1. by comparing the cutting and frictional components of the blunt cutter simulations with the results of the sharp cutter and the wearflat models respectively; and

2. by comparing the slope of the friction line with the friction angle of the material.

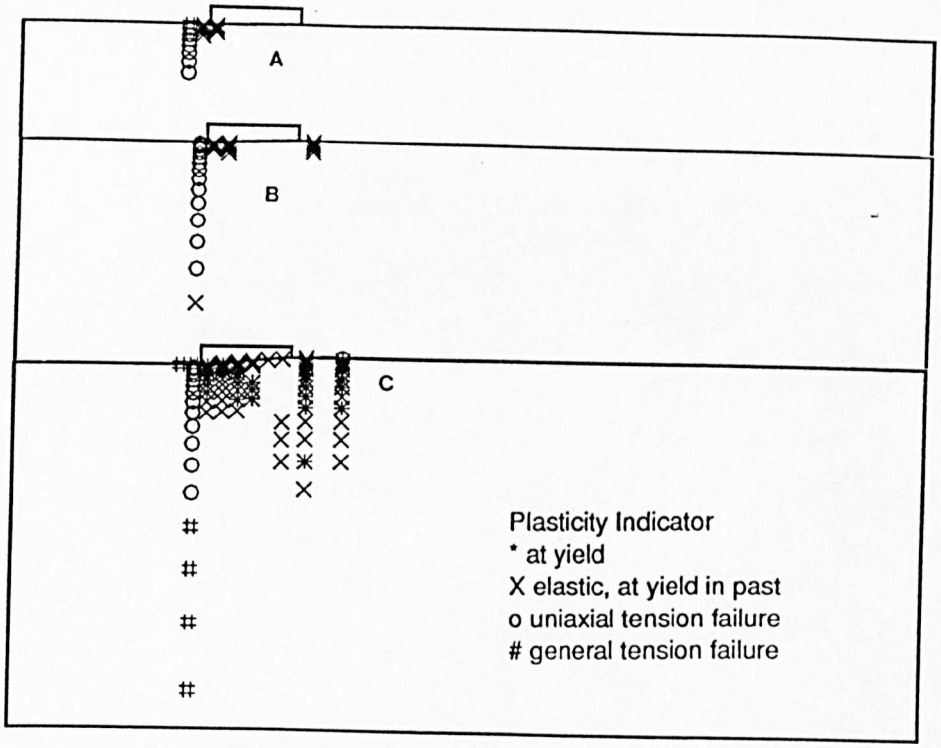

Figure 3.27: Plastic zones developed for a) 1°, b) 2°, and c) 5° inclination of the wearflat.

3.6.1 Model Description

Grid Geometry

The grid geometry is shown in Fig. 3.28. It is a combination of the geometries of the sharp cutter and the wearflat simulations. The number of elements used was 41x21. The dimensions were taken as 5 times the depth of cut in the direction of movement and 3 times the depth underneath the cutter.

Material Properties

As for the previous models, the material was modelled as a rigid-plastic Mohr-Coulomb material, deforming in plane strain conditions. The tool was modelled as a linearly elastic material. The values for the material properties were the same as for the sharp cutter and the wearflat (Table 3.3).

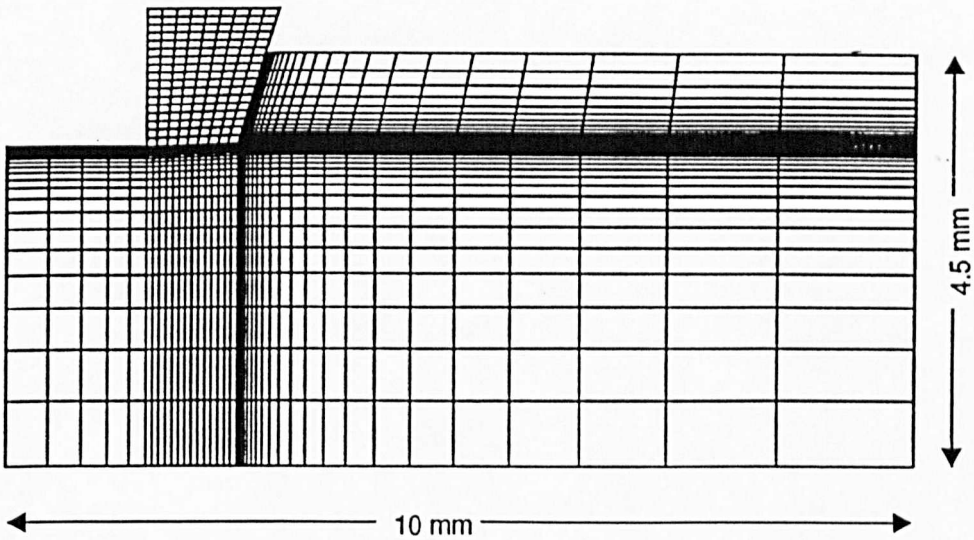

Figure 3.28: Geometry and dimensions for the blunt cutter simulations.

Boundary Conditions

The grid boundaries were fixed in three sides, preventing the grid from moving sideways and downwards. The top surface was left free and with no pressure applied to it, simulating atmospheric conditions. A constant horizontal velocity of 8E-6 mm/step was imposed on the tool.

'Time Steps'

The number of iterations required for the simulation to converge was about 600, as shown in Fig. 3.29, but 1500 'time' steps were computed to obtain the same displacement as for the sharp cutter model.

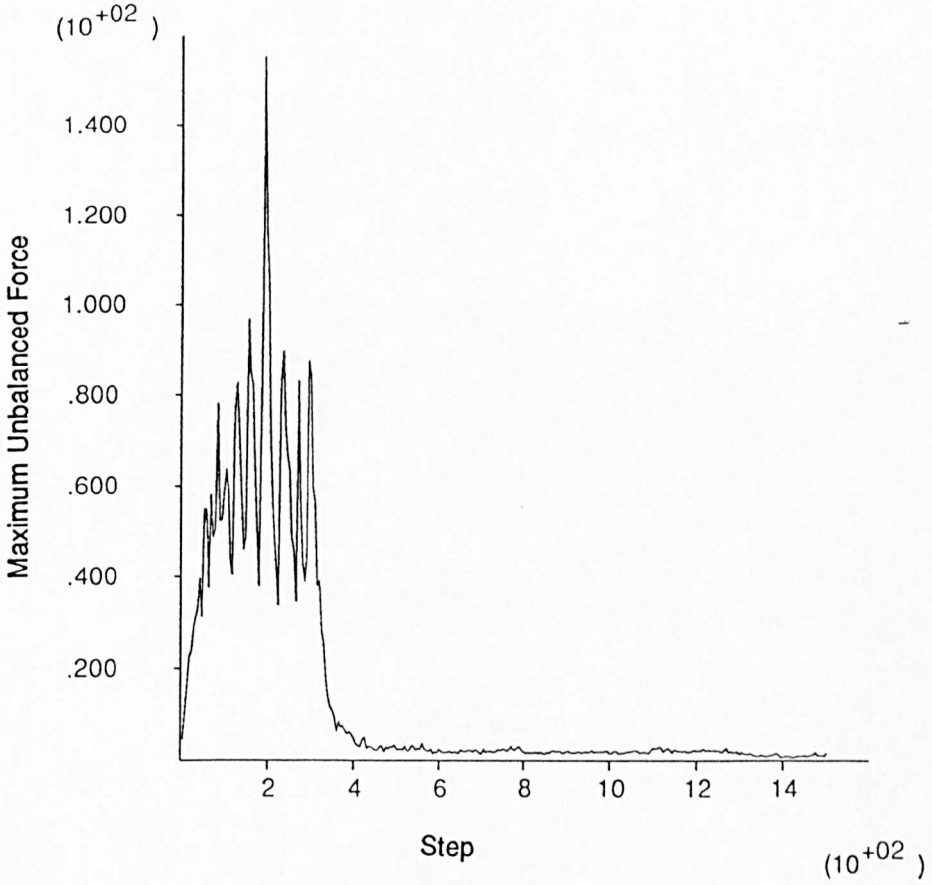

Figure 3.29: Typical history of maximum unbalance force for the blunt cutter simulations.

3.6.2 Parametric Investigation

To obtain the data for the $\mathcal{E}$–$\mathcal{S}$ diagram and the contact strengths on the tool, experiments changing the depths of cut and the wearflat lengths were performed. They will provide data for an $\mathcal{E}$–$\mathcal{S}$ diagram to be drawn and the friction line calculated. Table 3.7 presents the simulations conducted.

3.6.3 Analysis of Results

Failure Mechanism

By assuming material properties that made the model behave as a rigid-plastic material, failure was observed in the model after small strain had been imposed on the material. Once the material had failed in the contact surface, the failure zones expanded towards the inside of the material with the characteristics of the two single processes. The cutting face creates a zone of failure that surfaces at a

Model	*Depth* (mm)	*Wearflat length* (mm)
1	0.25	1.0
2	0.50	1.0
3	0.75	1.0
4	1.00	1.0
5	1.25	1.0
6	1.50	1.0
7	0.25	0.5
8	0.50	0.5
9	0.75	0.5
10	1.00	0.5
11	1.25	0.5
12	1.50	0.5

Table 3.7: Parameters studied for the blunt cutter simulations.

point predicted by Eq. (3.8), while the wearflat contact developed a zone of failure that advanced downwards into the material. A sequence of this progressive failure is presented in Fig. 3.30. Notice the compacted zone in front of the cutter. This feature was also seen in the sharp cutter simulations.

$\mathcal{E}$–$\mathcal{S}$ Diagram

The blunt cutter model was computed for two different wearflats and six different depths of cut. If the friction line in the $\mathcal{E}$–$\mathcal{S}$ diagram gives a slope angle that is equal to the friction angle of the material it means that:

1. the cutting and the contact processes are independent; and

2. the cutting forces are proportional to depth of cut.

Fig. 3.31 shows the $\mathcal{E}$–$\mathcal{S}$ diagram for all the tests with blunt cutters. As can be seen, the results are in a straight line. Parameters of linear regressions performed on these data are given in Table 3.8. From the results, the slope of the friction line is not exactly the same as ϕ, but they are very close. The difference might be due to the discretization of the grid and the interface logic used by the FLAC.

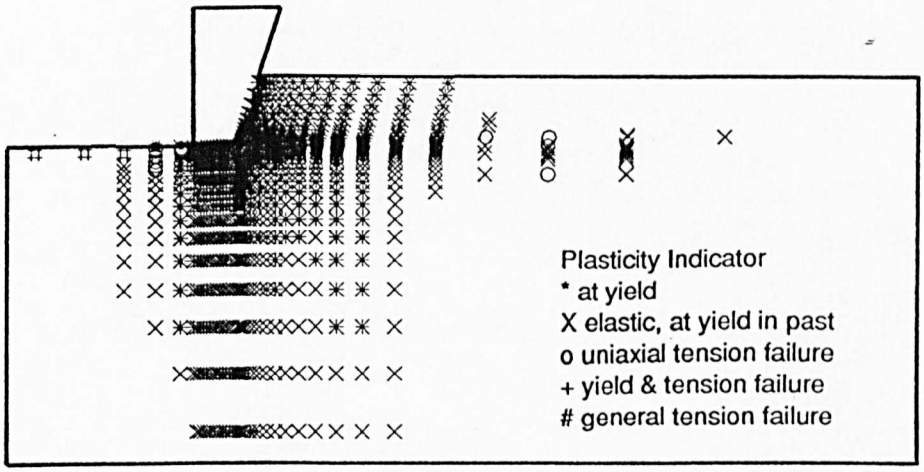

Figure 3.30: Plastic zones after 1500 steps of simulation with a blunt tool.

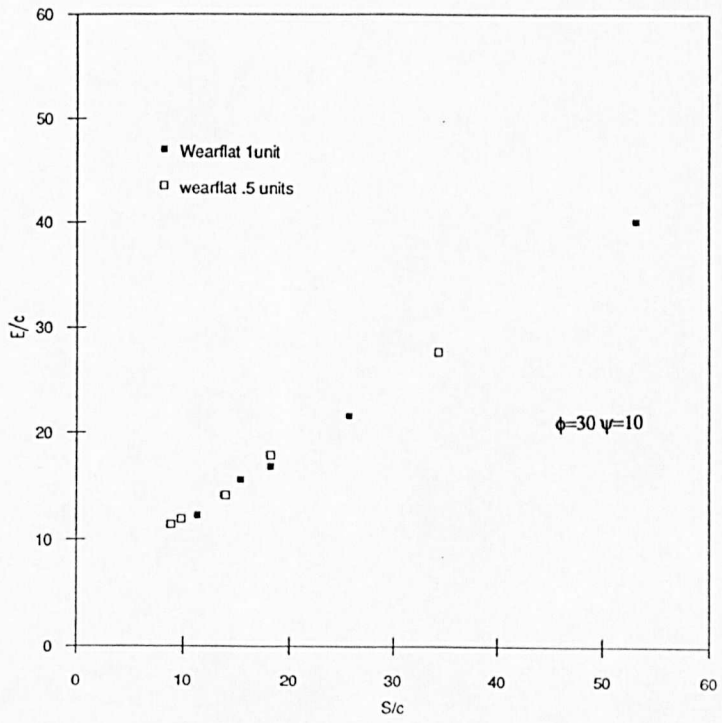

Figure 3.31: $\mathcal{E}$–$\mathcal{S}$ diagram for the numerical simulations with different depths of cut.

Blunt cutter	*Wearflat* 1mm	*Wearflat* 0.5mm
Slope	0.659(33.4°)	0.647(32.9°)
Intercept	4.93	5.54
r^2	0.99	0.99

Table 3.8: Linear regression parameters for the friction line.

Intrinsic Specific Energy

From the numerical results of the blunt cutter simulations with different depth of cut and different wearflat, the specific energy was calculated and the results are presented in Appendix B. The values were obtained from the printouts of the interface data. From these data, the average for ϵ/c calculated was of 8.51 and 8.31 for 0.5 and 1.0 mm wearflat lengths respectively. The average value of ϵ/c obtained from a sharp cutter model for the same friction angle was 7.85. As can be seen, the values are very close to each other.

Contact Stress

The contact strength, σ, can be calculated by three different methods (each requires different assumptions) from the results of the numerical experiments:

1. by subtracting the cutting contribution from the total forces in the blunt tool model;

2. by decomposing the forces into cutting and friction at the interface, from the interface data; and

3. by extracting it from a linear regression of the cutter normal force (vertical component) versus the cross-sectional area A, from numerical experiments in which only the depth of cut varies (same rock and tool).

Assuming that both parameters of the cutting ζ and ϵ are known, Eq. (2.16) can be used to determine the total average contact force. For ϵ/c equal to 8 and ζ equal to 0.41 (values obtained from the sharp cutter model), the average contact stresses determined by subtracting the cutting contributions are equal to 14.00 and 18.66 for wearflats of 1 mm and 0.5 mm respectively. The average value determined from the wearflat contact problem was of 10.95. Using this method, the calculation of the contact stress is very sensitive to the value selected for ϵ/c: if a value of 10 is selected then the contact stresses become 12.58 and 15.92, values that are much closer to the ones obtained from the contact problem simulations.

The second way of calculating the contact stresses is by taking the data directly from the interface printout(see Appendix C), as each interface, *i.e.* the cutting face and the wearflat, are calculated separately. In this case, the average results are 13.41 and 17.11 for wearflats of 1 mm and 0.5 mm respectively.

Using Eq. (2.16) (a line with the independent variable the depth of cut) the contact force can be estimated from a linear regression if:

1. the contact force is proportional to the contact length;
2. the cutting process is characterized by ζ and ϵ; and
3. the data for the regression come from tests in which only the depth of cut changes.

In Fig. 3.32, the depth of cut is plotted against the total normal force for the two different wearflats (1 mm and 0.5 mm) and for the sharp cutter. The average contact forces, for a condition where the cutter is not working, are estimated by regression analysis. Table 3.9, presents the parameters obtained by this method. From the results of Table 3.9, the average normalized contact stresses are 11.52 and 14.84 for 1 mm and 0.5 mm wearflat respectively.

Blunt cutter	*Wearflat* 1 mm	*Wearflat* 0.5 mm	*Wearflat* 0 mm
Slope	3.86	3.90	2.66
Intercept	11.52	7.42	0.33
r^2	0.86	0.99	0.99

Table 3.9: Linear regression parameters for the normal force F_n versus depth of cut δ.

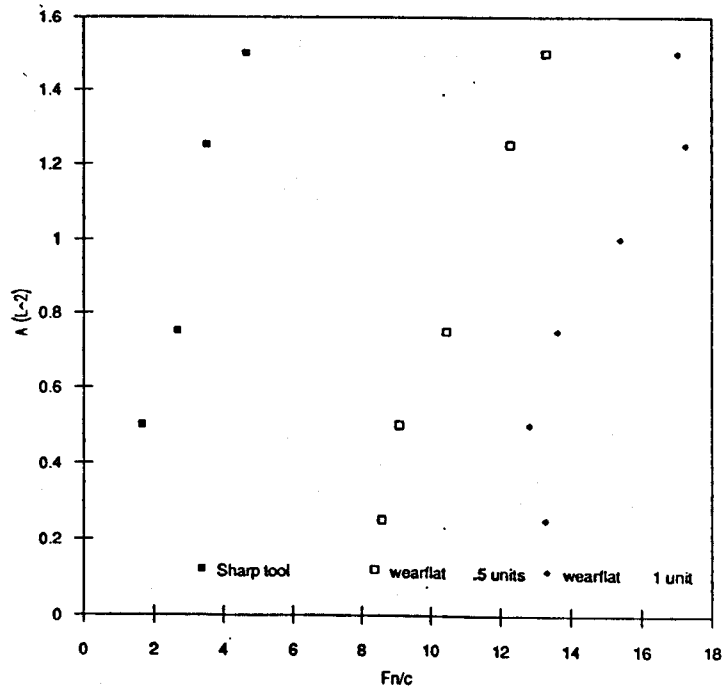

Figure 3.32: Normal force versus depth of cut.

3.7 Summary and Preliminary Conclusions

From the simulations performed during this research, the following points can be highlighted.

For the sharp cutter:

- the material yields in front of the cutter face;
- the intrinsic specific energy, ϵ, calculated from the numerical experiments of a sharp cutter, for different friction angles of the material, and of the interface, falls in between the upper and the lower bounds;
- varying the rake angle θ, the internal friction angle ϕ and the interface friction angle ψ showed that the shear surface changes shape and inclination with these parameters, but a good approximation of the extent of the failure on the surface of the material, can be predicted by drawing the shear plane proposed by Merchant (Eq. (3.8)); and
- the variation of the depth of cut (*i.e.* different discretization of the grid) does not influence the calculation of ϵ.

For the wearflat contact:

- the numerical code is valid for the modelling of the contact problem as it gives results that are between the upper and the lower bound solutions.
- the conjecture that the forces are proportional to the wearflat length is supported by the simulations; and
- as the inclination of the wearflat increases, the normalized contact stress increases linearly.

For the blunt cutter:

- The model gave a good insight on the mechanics of the cutting processes;

- the failure processes on the cutting face and the wearflat appear similar to those in the single processes;
- changing the depth of cut on blunt cutter simulations provides enough data for an $\mathcal{E}$–$\mathcal{S}$ diagram to be plotted;
- different methods for the estimation of σ were presented.

The code has proved capable of representing the cutting mechanisms. It has shown that the two mechanisms of drilling, cutting and friction at the wearflat contact appear to be *independent* as the model subject of this research assumed. It provided a good insight into the progressive failure of the material. The possibility of drawing an $\mathcal{E}$–$\mathcal{S}$ plot from the results of blunt cutter simulations has shown that the cutting forces are proportional to the depth of cut, and most importantly, that the processes of cutting and friction at the contact can be regarded as *independent.*

Chapter 4

Cutting Tests

4.1 Introduction

In Chapter 3, the numerical calculation showed that the process of drilling could be represented as a combination of pure cutting and friction at the interface tool/rock. It also provided evidence that these two processes were probably independent. In the following sections, a description of an experimental investigation, cutting sandstones, will be presented with the purpose of substantiating the hypothesis that drilling can be represented as a combination of two *independent* processes.

The test consists of producing a linear groove in a block of rock. The movement of the cutter across the rock, at a constant depth, induces stresses in the rock causing the formation of rock fragments. The equipment used to perform the cutting and measure the forces is described in Section 4.2.

This experimental work could be considered as a complement to the tests conducted by Glowka[24] in which, because the wearflat was parallel to the direction of the tool movement, the contact area was different to the measured wearflat[6]. This artifact will be avoided by having the wearflat at a small angle with respect to the direction of motion of the tool.

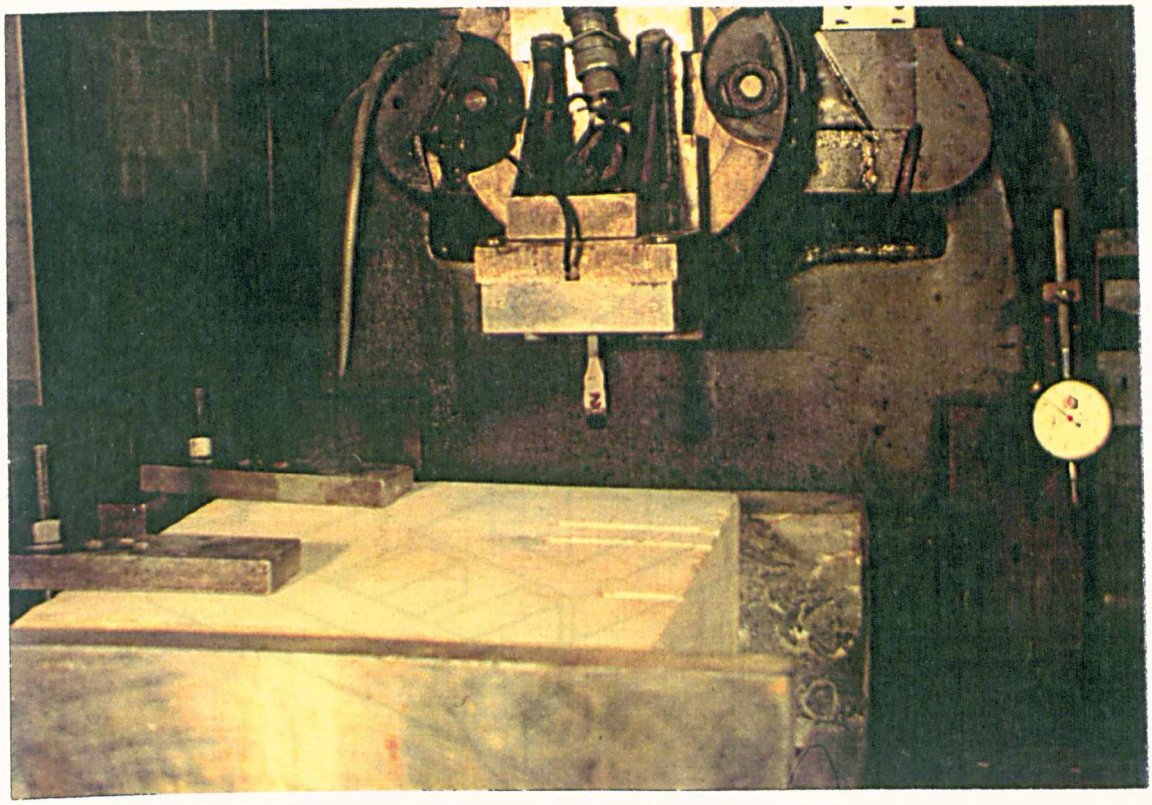

Figure 4.1: G.S.P.Shaping Machine with PDC tool and dynamometer.

4.2 Testing Facilities

4.2.1 Instrumented Shaping Machine

The linear cutting tests were performed in an instrumented shaping machine (Fig. 4.1). The shaping machine used at Imperial College is a Geometric Machine Tools G.P.S. Shaping Machine 117A. It has variable cutting speed which can be adjusted between 120 and 500 mm/s over a maximum stroke length of 850 mm. The stiffness varies between 10 and 100 kN/mm depending on the length of the stroke used.

4.2.2 The Dynamometer

The movement of the cutting tool through the rock results in a wide variation of forces acting on the tool. These forces can be measured using a flat plate dynamometer specially designed for this purpose (Fig. 4.2). The dynamometer

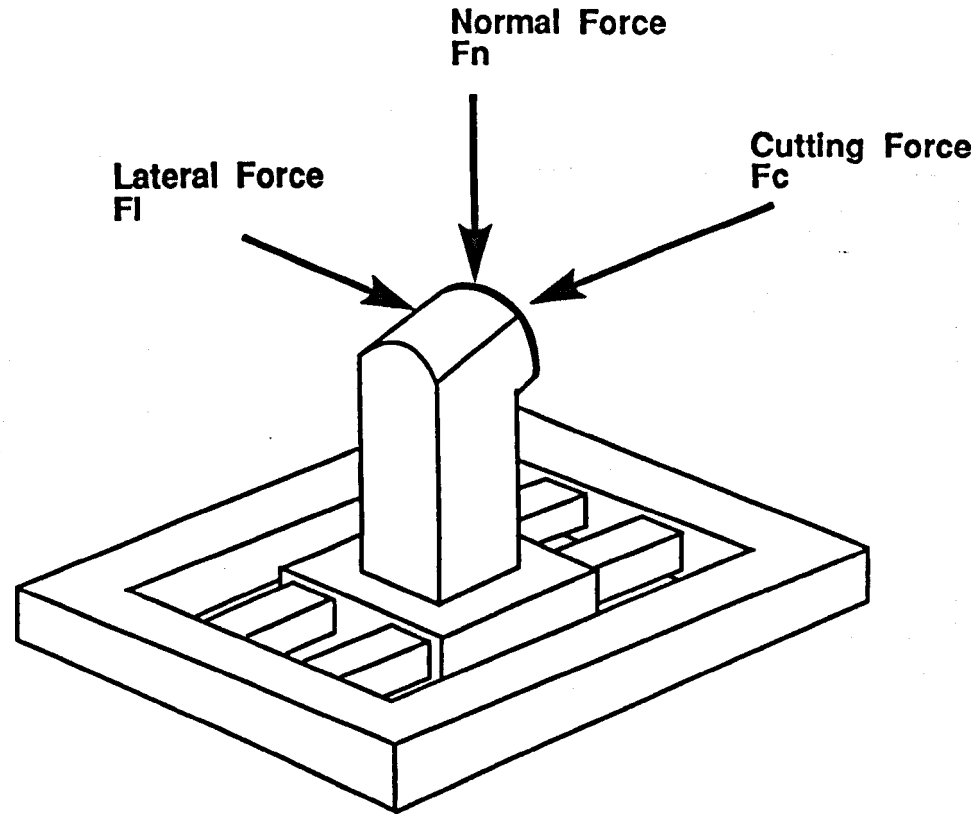

Figure 4.2: Flat plate dynamometer showing force components.

was first designed to monitor forces on individual drag bit tools by the Mining Research and Development Establishment. Subsequently, this design was developed at the Transport and Road Research Laboratory (TRRL) for the use on a pilot-scale boring machine.

The dynamometer is prepared with strain gauge bridges. It has 24 strain gauges which provide full bridge circuits to determine force in the three directions. The strain gauges are mounted on pillars, set in the plane of the dynamometer. These pillars experience bending moments due to the forces on the tool. The calibration was performed with a proof ring, once the dynamometer was mounted on the cutting head of the shaping machine. Fig. 4.3 shows a typical calibration plot. The dynamometer response to static loads is nearly perfectly linear. For each load, one hundred readings were made and then their average taken for the calibration. The variation of the values read is not due to the dynamometer but to electrical interferences (i.e. noise). The calibration was performed in two

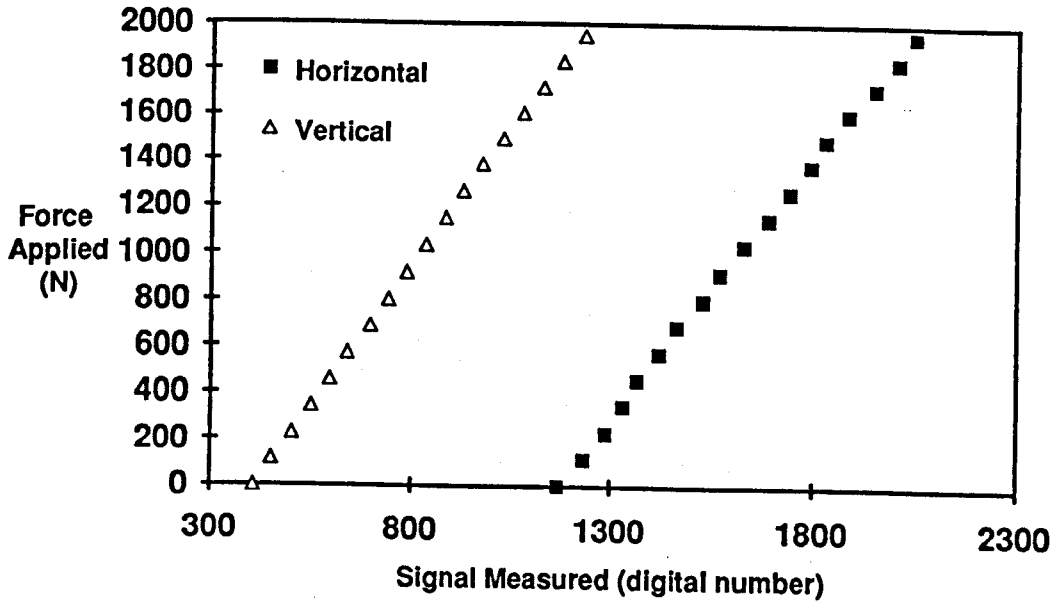

Figure 4.3: Calibration of the flat plate dynamometer.

directions and they showed independence of each other. Table 4.1 presents the linear regression parameters for the calibrations.

4.2.3 Tool Characteristics

Two PDC cutters with 15° back rake angle and 13.3 mm diameter were used. The cutters were cut to simulate wear in the area of contact with the rock surface (see Fig. 4.4). The wearflats of tools 1 and 2 made an angle with the surface of the rock of 2° and 3° respectively, so that the contact areas are very close to the

Tool Calibration	Horizontal Component	Vertical Component
Slope (N/division)	2.23	2.38
Intercept(divisions)	1170	403
r^2	0.9989	0.9998

Table 4.1: Linear regression parameters for dynamometer calibration.

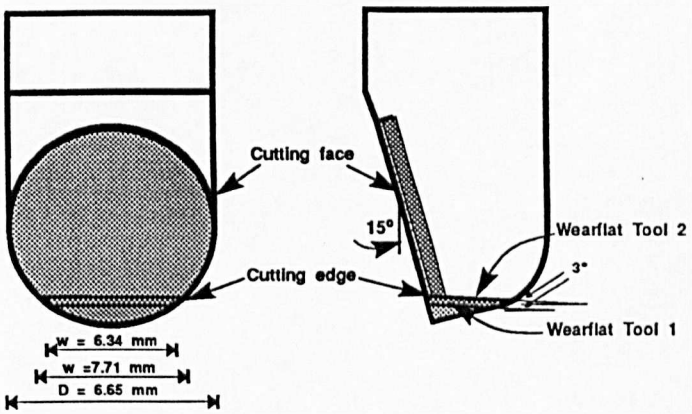

Figure 4.4: PDC cutter geometry.

Tool No.	Cutter Radius (mm)	Wear flat area (mm^2)	Cutting Edge (mm)
1	6.65	26	7.71
2	6.65	17	6.34
3	6.65	(0)	(0)

Table 4.2: Characteristics of cutters.

measured wearflat area. The wearflat was measured prior to the testing, following the technique used by Glowka[24] consisting of pressing the tool against the rock surface with carbon paper and a millimetric paper in between, so as to leave an impression of the contact area. The geometry of the cutters was measured with a travelling microscope to a precision of 0.001 of a mm. The tools were numbered 1 and 2, and are shown in Fig. 4.5. Tool numbered as 3 is the one used by Chaput[10] in his experiments with sharp cutters, results which will be used in this work as a reference. The main characteristics are presented in Table 4.2.

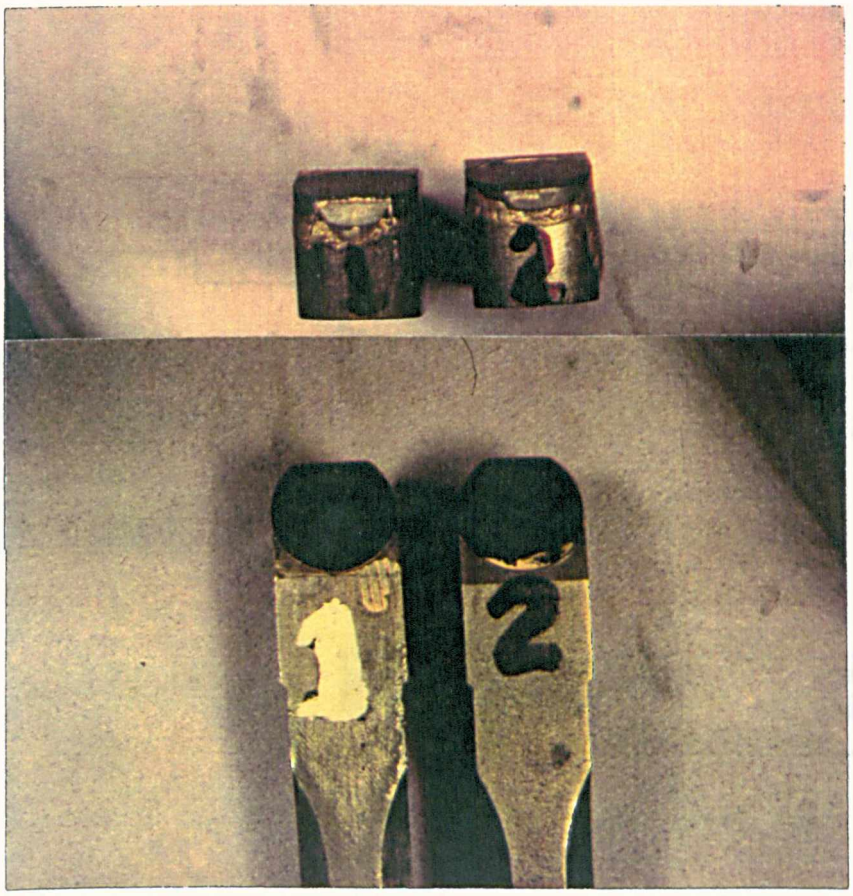

Figure 4.5: PDCs used in the experimental investigation.

4.2.4 Data Acquisition System

The voltages from the strain gauges are received in a signal conditioning multiplexer card (EXP-RES, Metrabyte Corp.), with switchable gains ranging from 1 to 1000. The analog signal amplified is then converted into a digital number by a fast A/D (Analog to Digital) converter card installed inside an IBM 286 compatible computer. The A/D converter, a DAS 16 G1 (Metrabyte Corp.), is a 12 bits digital conversion (4096 divisions), with 16 channels, a speed of 70,000 samples/s, and 4 programmable gains 1, 10, 100 and 500.

The data acquisition is achieved via "Asyst", an acquisition, analysis and control software package capable of handling large arrays of numbers (depending on computer expanded memory), and performing arithmetical, statistical, regression analysis, and fast Fourier transforms for frequency analysis. It also allows plotting of the results on the screen, a printer or a plotter. It possesses its own programming language. A flow chart of the acquisition system is shown in Fig. 4.6. The

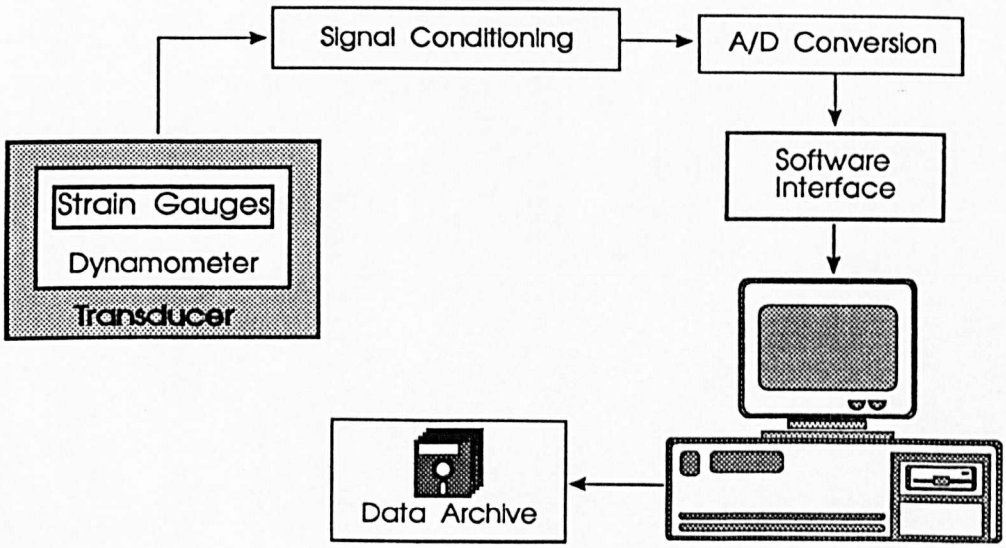

Figure 4.6: Rock cutting acquisition equipment.

code for the acquisition is presented in Appendix D.

4.3 Description of the Rocks Tested

4.3.1 Choice Criteria

The research to be carried out during this study was concerned with the validation of the method of interpreting the cutting response with blunt PDC cutters. The choice of rocks was determined according the facts/criteria described below.

- Most rock formations are not suitable for conventional PDC cutters, as in hard rocks excessive frictional heating produces 'thermally-accelerated wear' which quickly leads to the destruction of the PDC[63]. Thus, only relevant rock types were considered.

- Because a large number of tests were programmed, the rocks had to be homogeneous and isotropic so that the conditions of the tests were as constant

Rock	ϕ (deg)	c (MPa)
Crosland Hill	32	35
Pennant	29	27
Vosges	34	17

Table 4.3: Triaxial tests results.

as possible.

- The properties of the individual rock types selected had to be different, so as to be able to find some correlation between the material properties and the cutting parameters.
- Rocks and data for cutting tests with new 'sharp' tools should be easy available for reference.

The choice was finally made among the sandstones belonging to a suite of ten rocks (five sandstones and five limestones) considered as the most likely to be excavated (in mines, tunnels, or wells) in England and France[64].

These rocks had been intensively tested for cuttability at Imperial College and at the Ecole des Mines de Paris, under an EEC Research Contract[64]. The three rocks were: Crosland Hill Millstone Grit (Hard York Stone), Forest of Dean Pennant and Red Vosges sandstones. The first two come from locations in England while the third comes from France. A summary of triaxial test results performed on these rocks are presented in Table 4.3.

A complete geomechanical characterization of the three rocks selected was carried out for this research and the results are presented in Appendix E.

4.3.2 Crosland Hill Millstone Grit sandstone

The Crosland Hill sandstone used for the work described in this thesis is extracted from a quarry near Crosland Moor, Huddersfield (NGR:SE118143), U.K. Similar sandstone has been previously tested by Santarelli[65] and Priest and

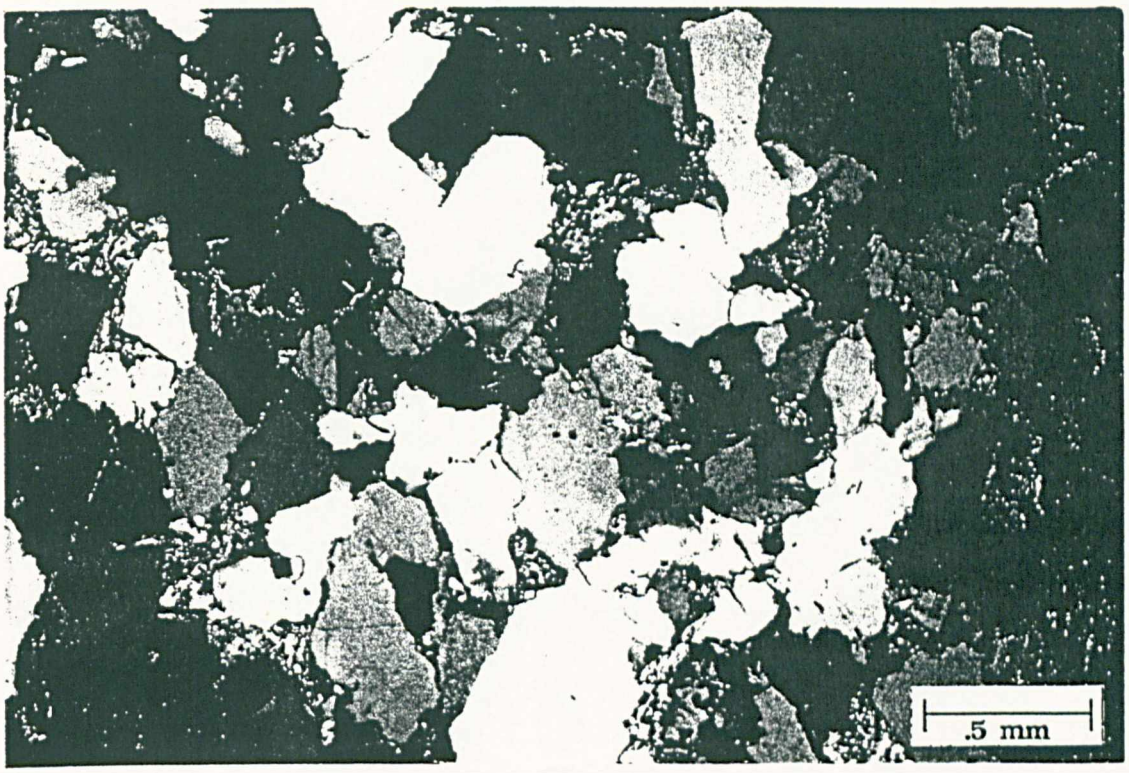

Figure 4.7: Thin-section Crosland Hill sandstone (from Chaput [10]).

Selvakumar[66]. It belongs to the Millstone grit Carboniferous period. The rock is grey beige to pale yellow in colour. It is made of subangular grains of quartz, whose average diameter is around 0.5 millimetres. Slightly altered grains of feldspars and both dark and white mica are present. There is no trace of bedding. The cement is not abundant, but the grains are strongly pressed together and form a very resistant mosaic. A thin-section of this rock is presented in Fig. 4.7. The compressive strength of the rock is 90 MPa (Priest and Selvakumar[66] obtained 100 MPa) and its density 2428 kg/m^3. Other characteristics can be found in Appendix E.

4.3.3 Forest of Dean Pennant sandstone

This Pennant Grit sandstone is extracted from a quarry in Barnhill, Coleford, Gloucestershire (NGR:SO597106), U.K. It belongs to the Upper Carboniferous and comes from one of the Coal Measures. It is fine grained and grey in colour.

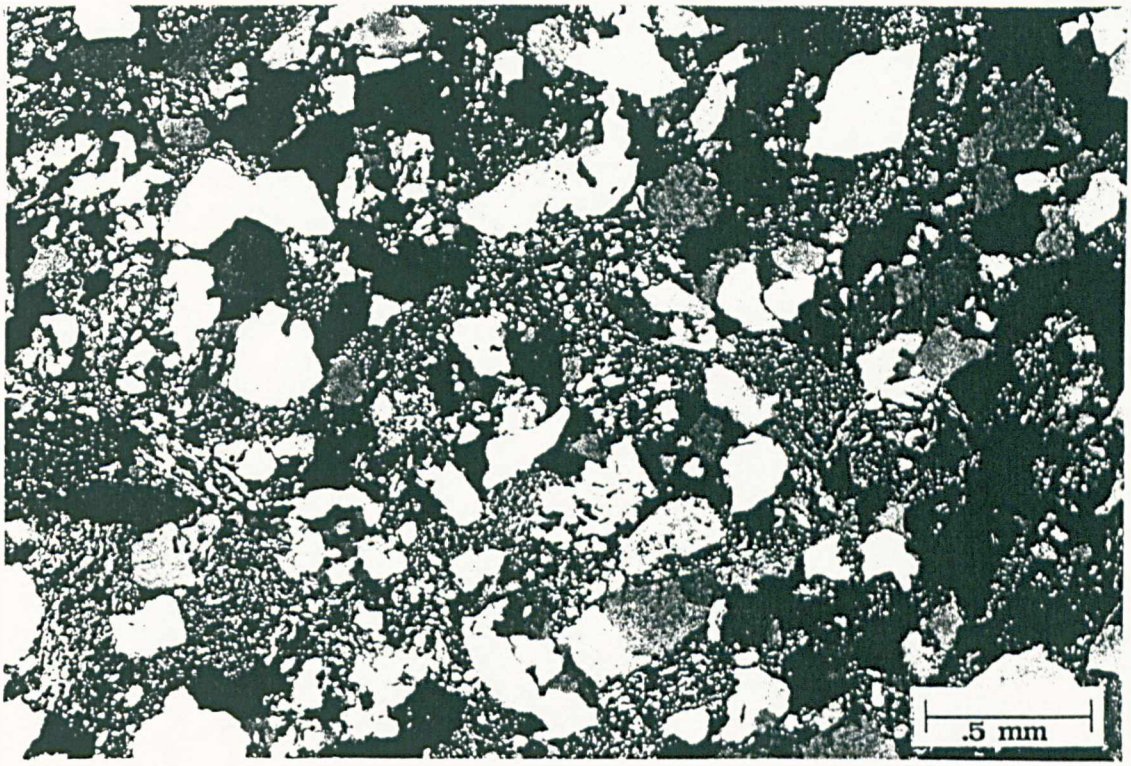

Figure 4.8: Thin-section of Forest of Dean sandstone (from Chaput [10]).

A thin-section of this rock is presented in Fig. 4.8. The average diameter of the grains is 0.25 mm. The material consists of quartz, altered plagioclase, feldspar in large quantities, abundant particles of altered material and mica. The cement is silicious and bonds the grains together with a fine inter- granular film. The bedding is highlighted by thin laminae of aligned microquartzites. This rock has been used in water jet cutting experiments by Fowell *et al.*[67], who reported a uniaxial compressive strength of 172 MPa and a density of 2652 kg/m^3. The value obtain from U.C.S. tests for this research was 88 MPa and the density was measured as 2446 kg/m^3.

4.3.4 Red Vosges sandstone

This rock comes from the region of Alsace from a quarry near the town of Rothbach (48°55'N,7°31'E), 40 Km NW of Strasbourg, France. This is a fine grained brownish red sandstone. It is made up of angular equidimensional grains, 0.1

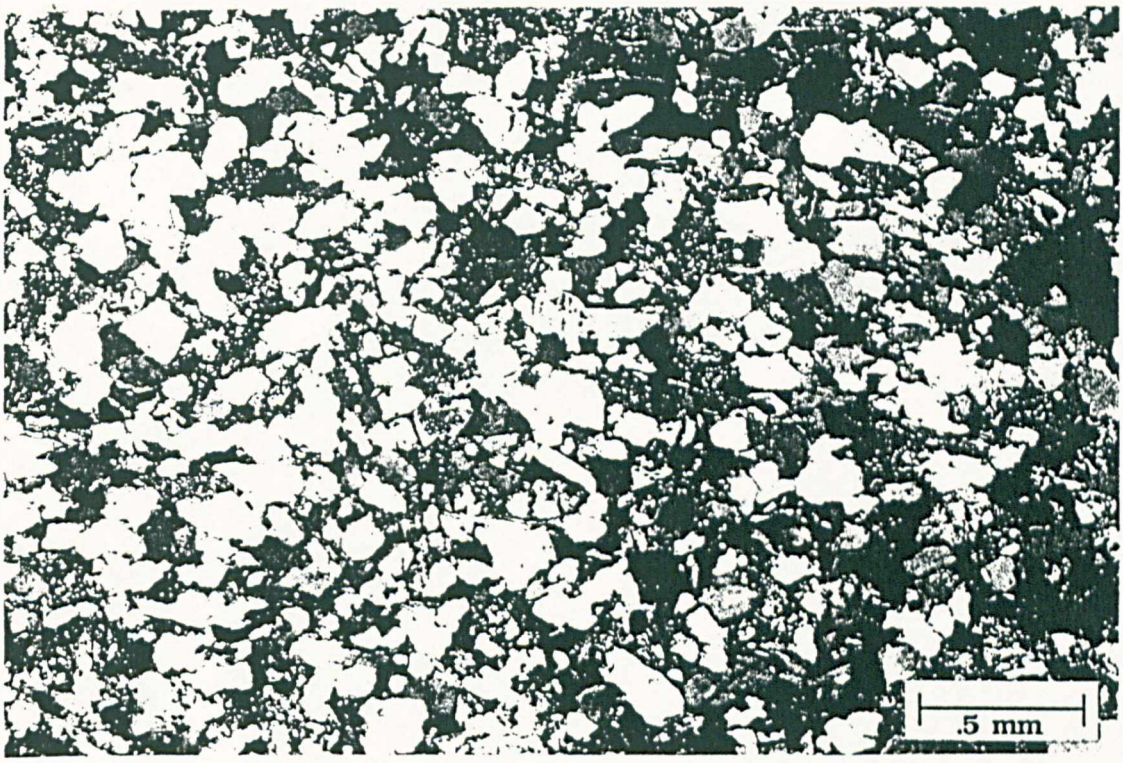

Figure 4.9: Thin-section Red Vosges sandstone (from Chaput [10]).

mm in size. Its main constituents are quartz and, slightly altered feldspars, with abundant mica along the bedding planes. The cement is almost non-existent: the grains touch and are just interlinked together. Therefore it is somewhat friable. A thin section is shown in Fig. 4.9. The rock was tested to obtain the most relevant geomechanical parameters and physical characteristics. The uniaxial compressive strength of the rock was found to be around 54 MPa, with a density of 2067 kg/m^3. Other parameters are presented in Appendix E.

4.4 Testing Procedure

4.4.1 Sample Preparation

The rocks samples were blocks with no fixed dimensions; length varied from 300 to 375 mm while the width and the height varied between 150 and 300 mm. The surface of the sample was carefully prepared by successive grindings of 0.1 mm thickness, using a 12 mm miniature orthogonal drag pick of hardened steel. This

was done to level the surface as flat as possible, as the tests needed to be at constant depth. It was also done to ensure the same experimental conditions in all the rocks.

Crosland Hill sandstone is the hardest of the three rocks tested. During the planing of the surface, the friction between the tool and the rock created very high temperatures on the pick, and water was used to cool the tool down. The wetted rock was left to air dry for approximately one hour and then tested. Because of this, the water content of the rock is not known at the moment of testing.

4.4.2 Testing Conditions

The lowest cutting speed, 140 mm/s, was selected because then more points could be sampled per mm. The multiplexer card receiving the voltages from the strain gauges was set to a gain of 500, while the A/D converter was set to a gain of 10. This configuration limited the sampling rate to 1760 Hertz. Since the cutter speed was 140 mm/s, this sampling rate was equivalent to 12.5 readings/mm of tool displacement, a reasonable number for the type of process.

The cutting depth varied from 0.25 to 1.50 mm in steps of 0.25 mm. The accuracy of the measuring device for the depth of cut was 0.01 mm.

The tests were conducted at atmospheric conditions: no confining pressure nor mud effects were taken into account. The rocks were tested dry, except for the Crosland Hill which was not completely dry after preparing the sample, due to the problems mentioned above.

4.4.3 Experimental Programme

This consisted of performing linear cutting tests with two blunt PDC cutters with characteristics described in Section 4.2.3. Six different depths of cut varying from 0.25 mm to 1.50 mm in steps of 0.25 mm, on each of the three rocks selected were performed. To have a measure of the development of the wear, after each series

of tests a reference test was performed on the Vosges sandstone at 1 mm depth of cut. One replication was also allowed for comparison of results.

4.4.4 Description of a Test

A rock of sample of approximately 300x250x300 mm^3 is placed on the table of the shaping machine, as horizontal as possible, and fixed by means of hydraulic jacks and mechanical clamps. The rock surface is then planed as described in Section 4.4.1. After the rock surface has been prepared, the chisel pick is replaced with the PDC cutter mounted on the dynamometer. The cutter is displaced on top of the surface and the table is moved slowly upwards until the bottom of the PDC cutter slightly touches the rock surface. At this point the machine is stopped and the depth measuring gauge is set to zero. The depth of cut is then adjusted. This depth is measured from the cutting edge of the cutter not from the bottom of the wearflat. The machine is now ready for the test. The data acquisition equipment is then prepared and started, it has an internal delay of 9 seconds, which allows enough time to get to the shaping machine and start the test as soon as the computer beeps. The head of the shaping machine moves across the rock surface dragging the PDC cutter along. The cutter induces stresses on to the rock surface causing the formation of rock fragments.

Once the tool has reached the end of the rock sample, the table is lowered down quickly, so the tool does not touch the rock on its way back. Then the machine is stopped. Meanwhile the computer recorded the variation of the voltage on the dynamometer in the two directions of interest.

The voltages are then converted to forces by the calibration factors. Typical records of the horizontal and vertical components of the force are shown in Fig. 4.10 and Fig. 4.11 respectively, for a test performed in Vosges sandstone at a cutting depth of 1.00 mm with tool No.2. It shows how the forces vary with the distance travelled by the cutter. The recorded forces are saved onto floppy disks for further analysis.

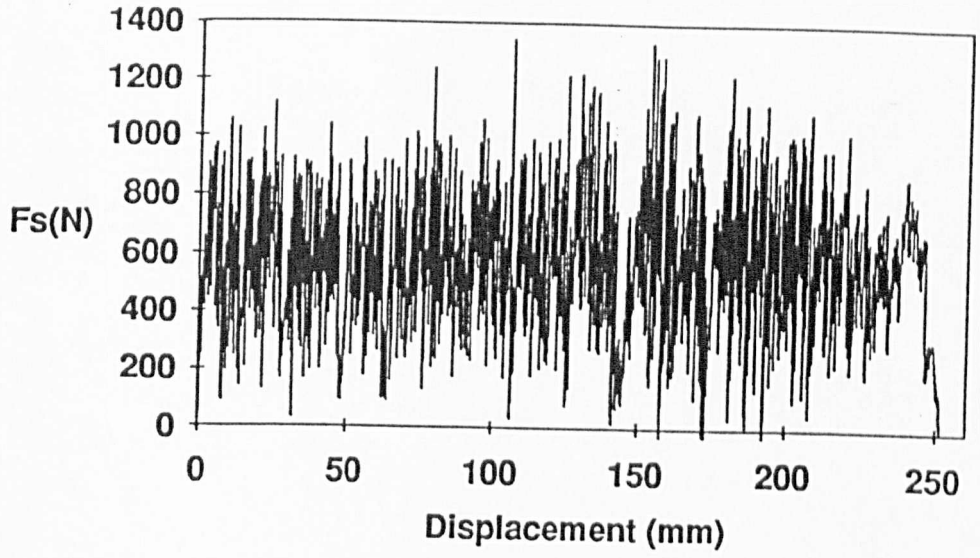

Figure 4.10: Horizontal force.

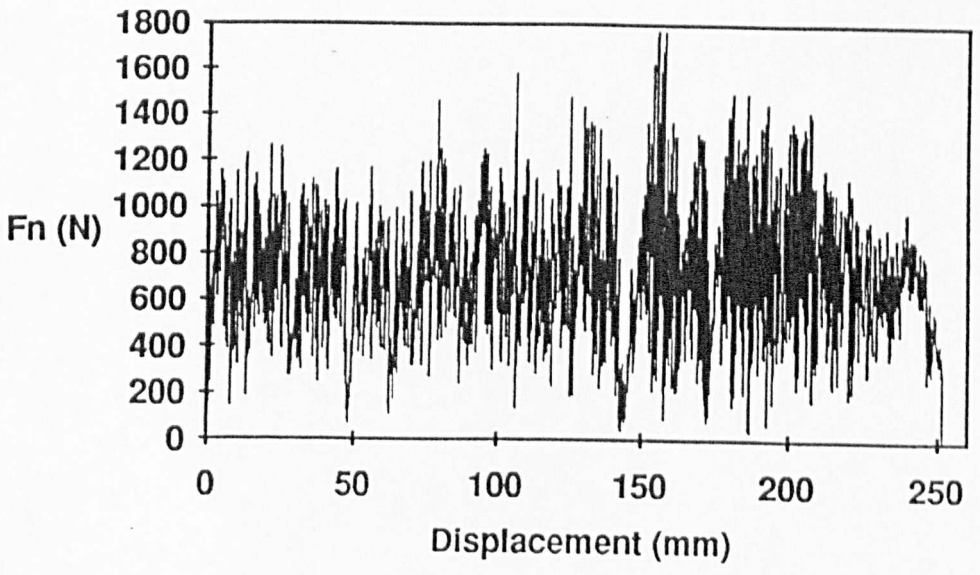

Figure 4.11: Vertical Force.

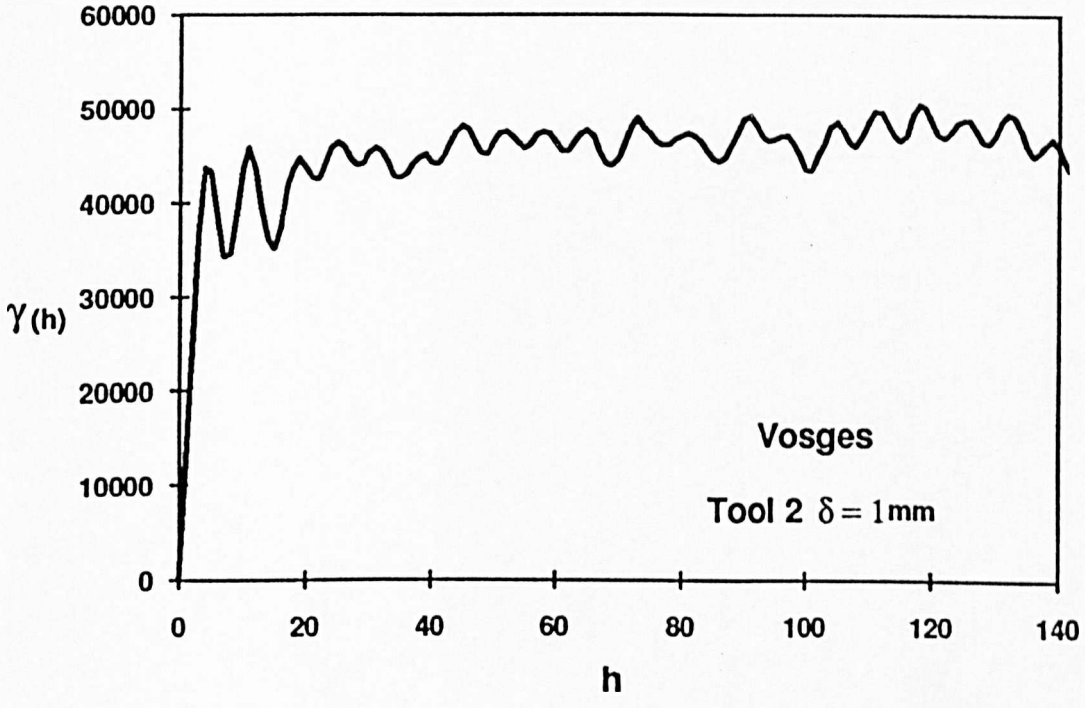

Figure 4.12: Variogram for the horizontal force.

4.4.5 Test Results

From the data collected for each cutting test, which was about 3000 points for each of the force components, the average of the these forces was taken for the analysis.

An examination of the variation of the forces with time was performed to determine the minimum distance over which the average could be taken. It was done by calculating the variogram on the recorded forces. A typical example of a variogram for the horizontal force (see Fig. 4.10) is shown in Fig. 4.12. The variogram presents the typical spherical model with a waviness possibly representing periodicity[68, 69]. It also shows the zone of influence between h=5 and h=20; this probably gives a good estimate of what the length of a single event on the cutting process is. In the example given, h=5 to 20 represents a true length of 0.40 to 1.60 mm for a depth of cut of 1 mm.

Fig. 4.13 and Fig. 4.14 present plots of the forces against depth of cut for the

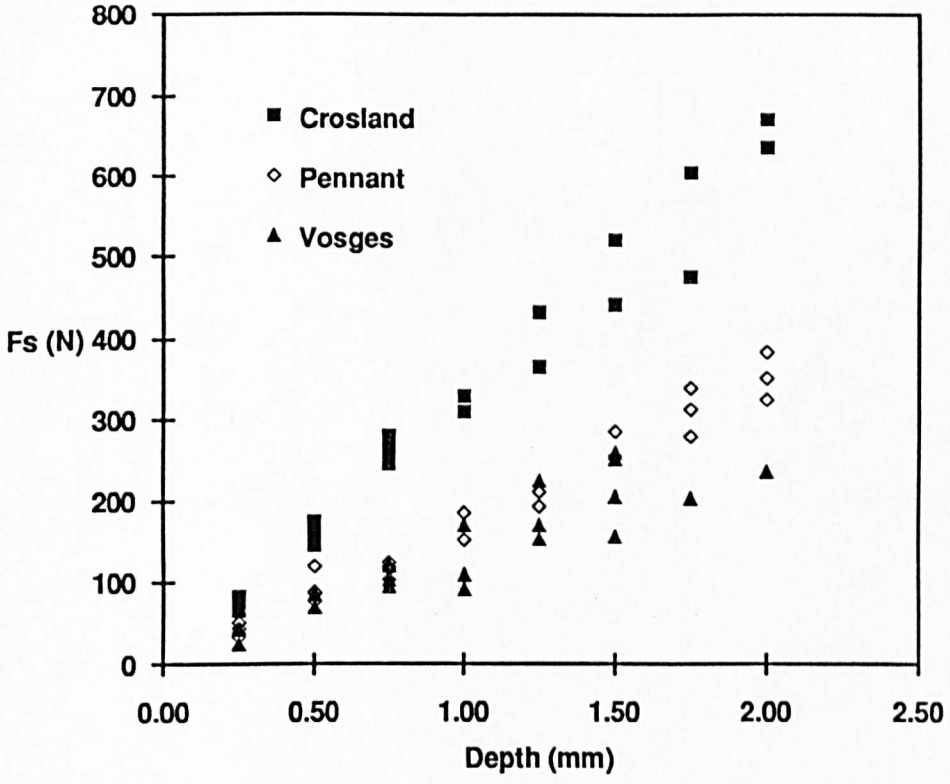

Figure 4.13: Horizontal force versus depth of cut ('sharp' tool).

tests performed with the sharp cutter[10]. The plots show a reproduction of the results of previous investigations (see Chapter 2), in which the main conclusion was that the horizontal and vertical forces increase with depth of cut, and that these forces are linearly related (see Fig. 4.15). When plotting the same graphs for the results of the blunt cutters, the relation is not so clear (see, Fig. 4.16 and 4.17), this is probably due to the effect and the continuous development of the wearflat.

The cutting test results are presented in Appendix F.

4.5 Summary and Preliminary Conclusions

This chapter has described the experimental work performed for this research. It has introduced the equipment used as well as the rocks tested. The cutter characteristics were described —of which one characteristic made these tests different from previous investigations: this is that the wearflat makes a small angle with

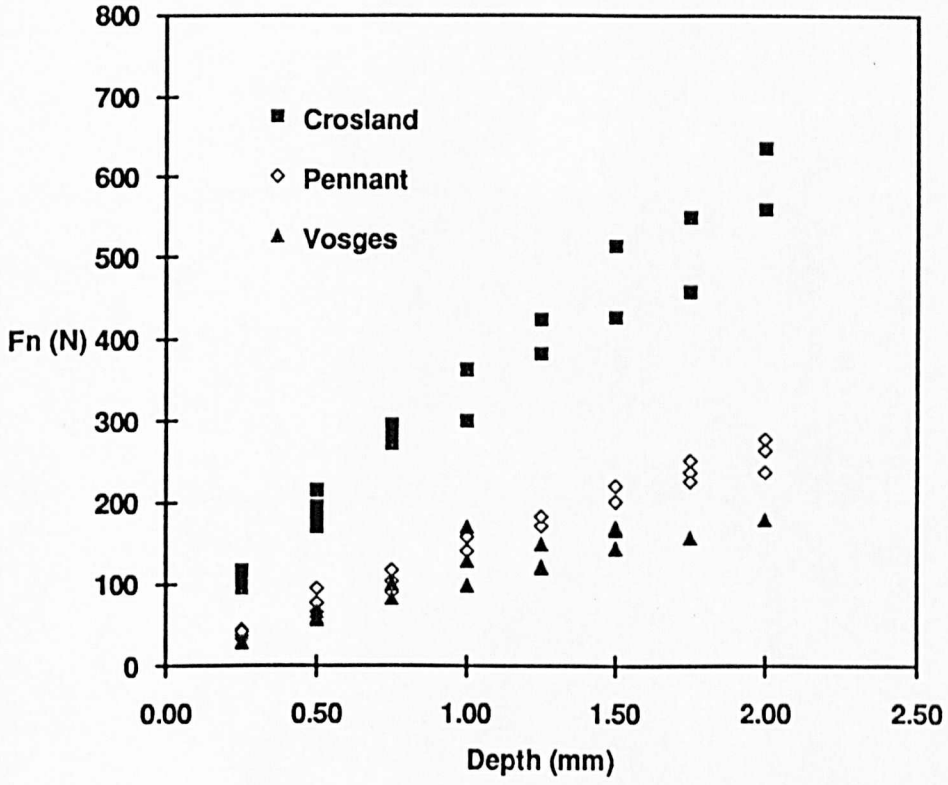

Figure 4.14: Vertical force versus depth of cut ('sharp' tool).

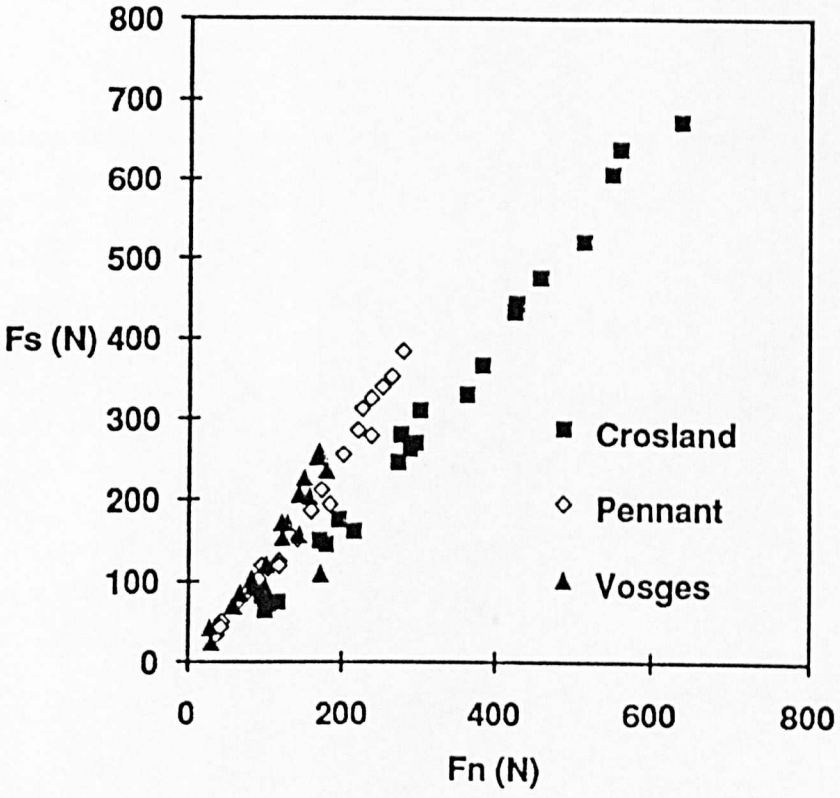

Figure 4.15: Horizontal versus vertical component ('sharp' tool).

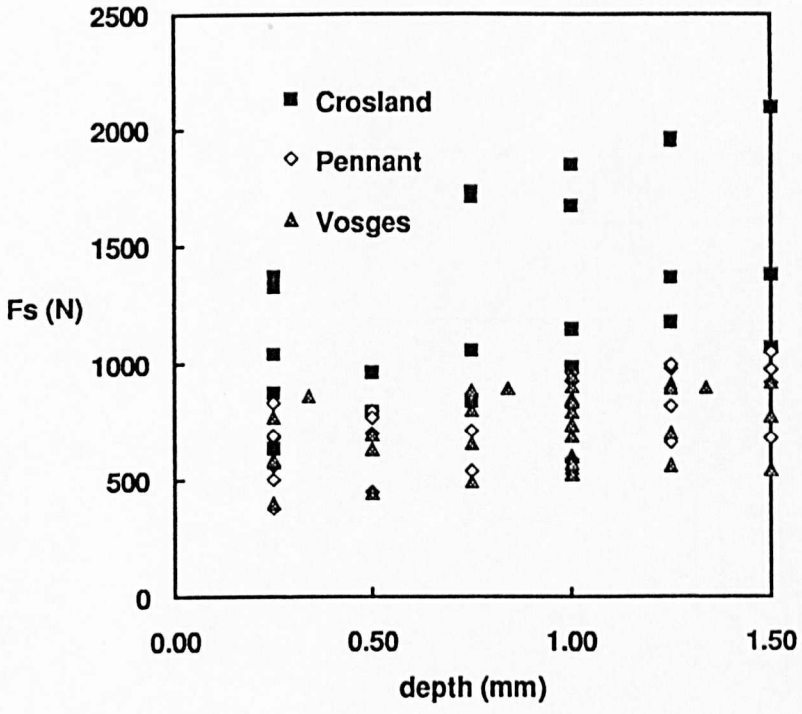

Figure 4.16: Blunt tool horizontal force versus depth.

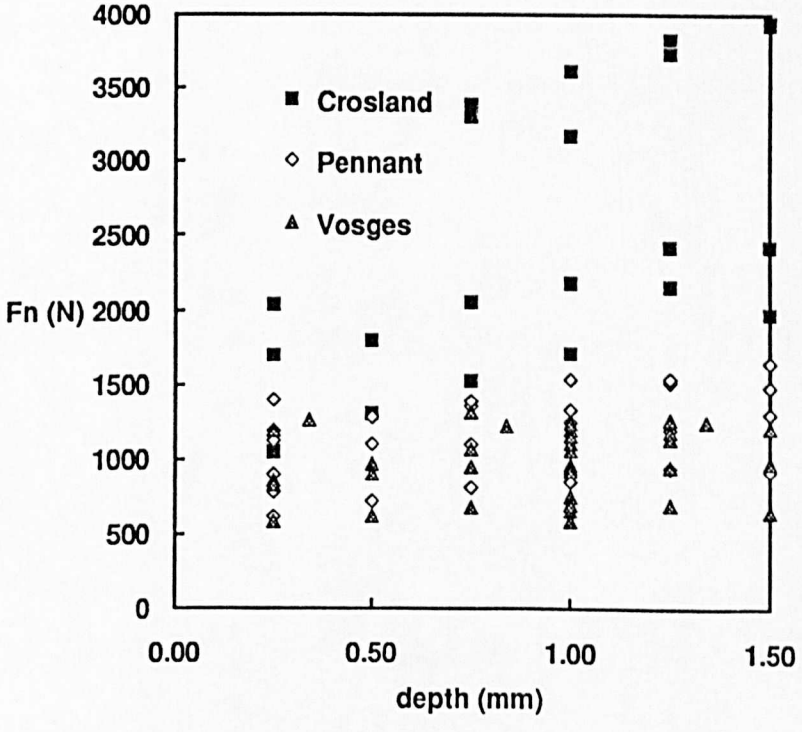

Figure 4.17: Blunt tool vertical force versus depth.

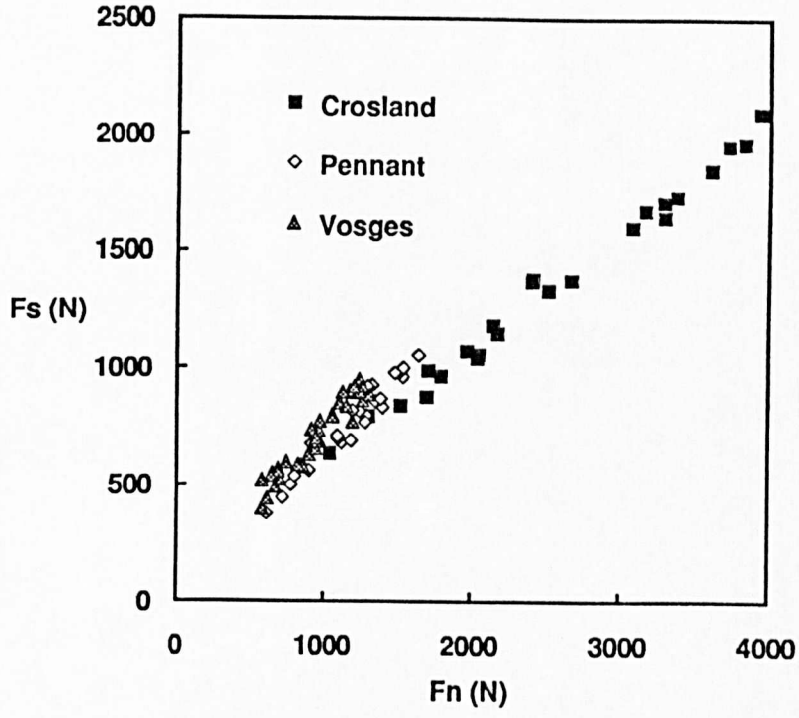

Figure 4.18: Horizontal versus vertical force (blunt tool).

the surface of the rock producing a nearly constant contact area with it. The experimental programme and the laboratory conditions were also presented.

From the experimental results, it is possible to conclude that, when cutting rock with 'sharp' cutters, there is definitely an increase in the forces when the depth of cut is increased, and that the relation between the horizontal and the vertical components of the forces on the tool is linear.

When cutting rock with blunt cutters, the results do not show clearly the relations mentioned above and they need to be analyzed differently. The following chapter will present the analysis of the cutting results with the blunt PDCs, utilizing the model proposed by[6].

Chapter 5

Analysis of Experimental Results

5.1 Introduction

The experimental data from tests with blunt cutters have been presented in Chapter 4. They show that the conventional analysis that the force increases with depth of cut is not as clear as when 'sharp' cutters are studied. In this chapter, the same data will be presented but analyzed following the new model discussed in Section 2.3. The procedure to be followed is to determine the friction line, the cutting point, and ways of estimating what the contact frictional forces could be for each rock tested.

5.2 Determination of the Friction Line

Following the cutting and friction model, an $\mathcal{E}$-$\mathcal{S}$ diagram can be drawn with the test data considering Eq. (2.14). The $\mathcal{E}$-$\mathcal{S}$ diagram for each of the rocks tested (Figures 5.1, 5.2, 5.3) supports the contention that there is a linear relation between the specific energy, $\mathcal{E}$, and the drilling strength, $\mathcal{S}$. The two parameters $\mathcal{E}_o$ and μ, that characterize the friction line, have been calculated by linear regression (Table 5.1). These linear regressions were calculated only for the tests with tools 1 and 2, as the data for tool 3 cluster along a different friction line due to the "γ" effect of the tool (see Appendix G). Note that the intersection of the

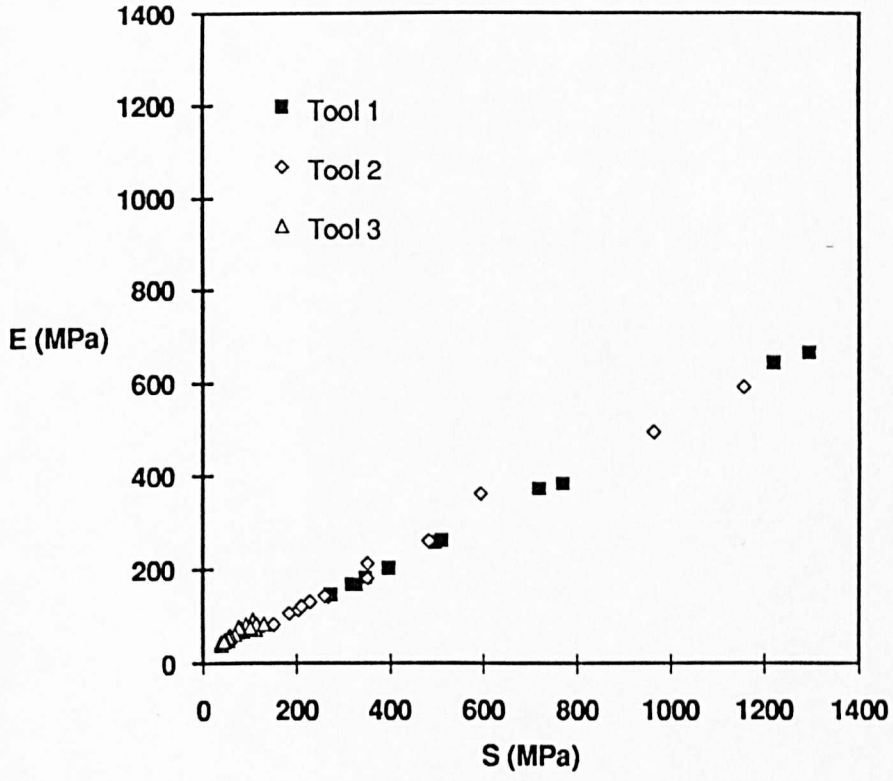

Figure 5.1: $\mathcal{E}$–$\mathcal{S}$ diagram for cutting experiments in Crosland Hill.

two friction lines appears to be close to the ideal cutting point estimated below. The $\mathcal{E}$–$\mathcal{S}$ diagram for all the cutting tests (Figures 5.4,5.5) clearly indicates the different slopes of the friction line for the three sandstones. The values of the friction angle, $\arctan \mu$, extracted from a linear regression of the $\mathcal{E}$–$\mathcal{S}$ data, can be compared to the internal friction angle of the rock obtained from triaxial tests (Table 4.3). This comparison shows a very good match between the friction angles obtained by the two methods for the Vosges and the Pennant sandstones. There is however a small discrepancy between the two friction angles for the

Rock	Slope μ	$\arctan \mu$ (deg)	Intercept $\mathcal{E}_o$ (MPa)	r^2
Crosland Hill	0.51	27	9.7	0.994
Pennant	0.58	30	10.6	0.997
Vosges	0.67	33	9.0	0.998

Table 5.1: Regression characteristics of $\mathcal{E}$–$\mathcal{S}$ Diagram.

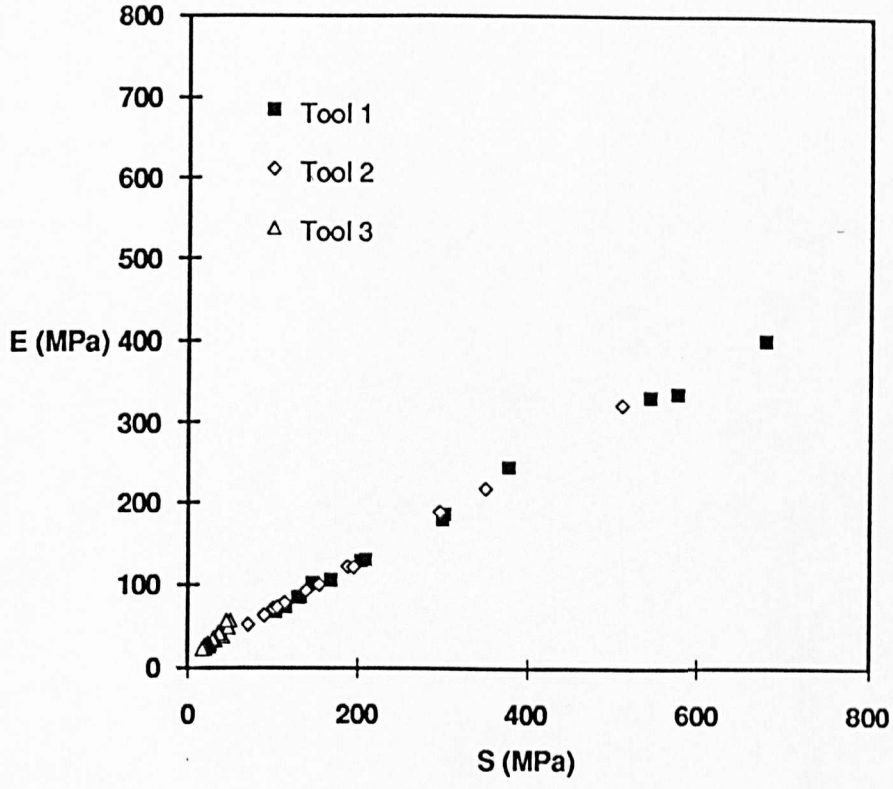

Figure 5.2: $\mathcal{E}$–$\mathcal{S}$ diagram for cutting experiments in Pennant.

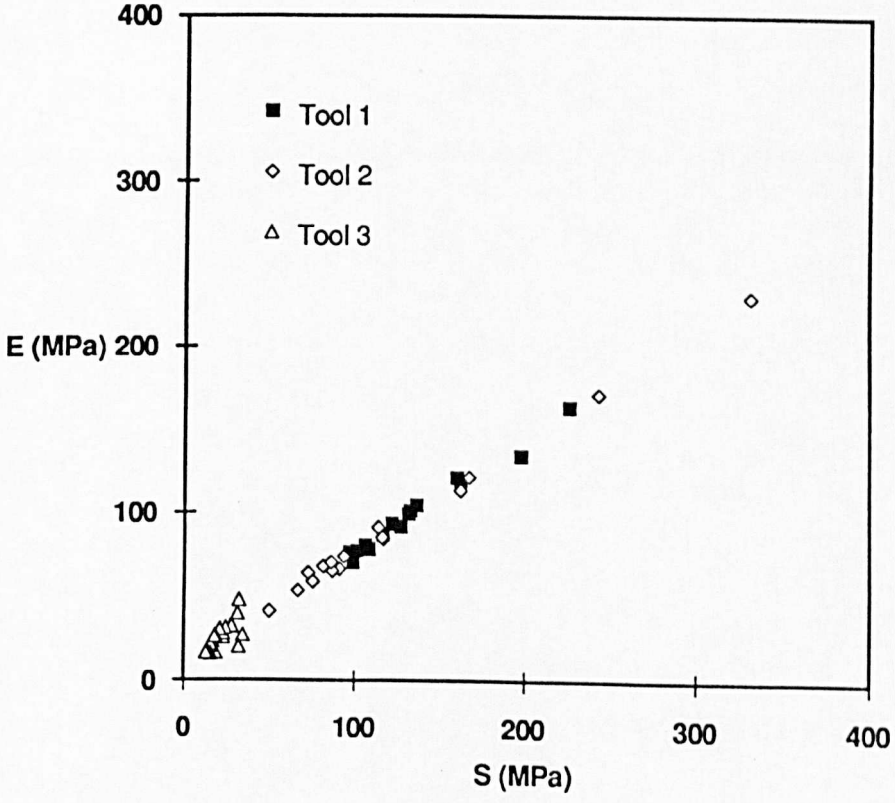

Figure 5.3: $\mathcal{E}$–$\mathcal{S}$ diagram for cutting experiments in Vosges.

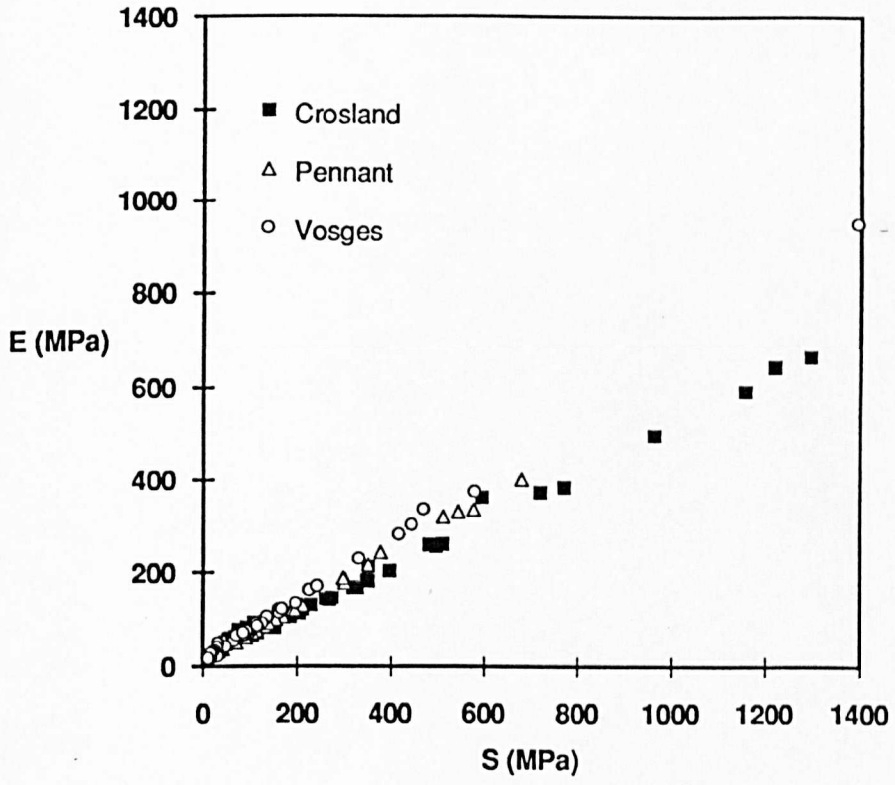

Figure 5.4: $\mathcal{E}$–$\mathcal{S}$ diagram for all cutting experiments.

Crosland Hill. One possible cause for this discrepancy is the high value of the contact stress in these tests (σ about 120 MPa, Section 5.4). Indeed, the internal friction angle in rocks is somewhat dependent on the magnitude of the mean stress and the friction angle should ideally be compared at the same reference stress. Note that the maximum confining pressure used in the triaxial tests was 23 MPa for the Vosges and 30 MPa for the Pennant, while the estimated contact strength was about 40 MPa for the Vosges and 50 MPa for the Pennant (see Section 5.4). Another factor that could affect the results is the fact that the rock was not dry. Certainly water content affects the results in uniaxial and triaxial tests, giving a lower value if the tests are drained. Two triaxial tests were performed to determine the friction angle of the Crosland in saturated samples. The tests gave a friction angle of 28° (see Appendix E for test specifications).

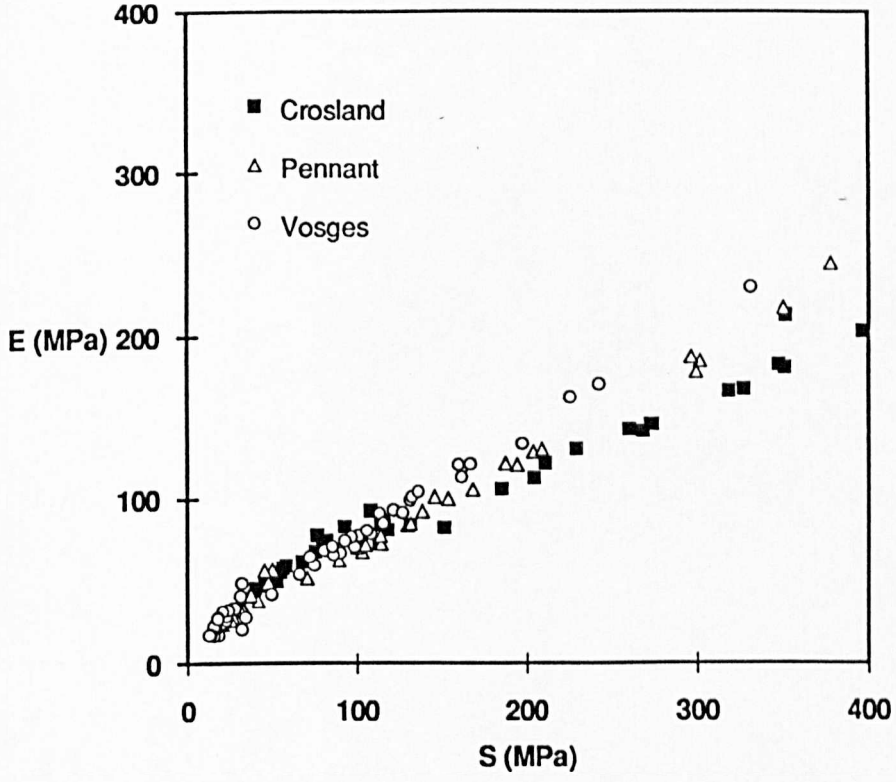

Figure 5.5: $\mathcal{E}$–$\mathcal{S}$ diagram for all cutting experiments (partial view).

5.3 Determination of the Cutting Point

The cutting point in the $\mathcal{E}$–$\mathcal{S}$ diagram characterizes ideal cutting conditions that can only be achieved with a perfectly sharp cutter. Two methods to estimate the cutting parameters ϵ and ζ are described below.

5.3.1 Estimation from Sharp Cutter Tests

The first approach that comes to mind for determining the cutting point is to exploit results of sharp cutter experiments [10]. The results of these tests are clustered in the lower left part of the $\mathcal{E}$–$\mathcal{S}$ diagram and can be used to obtain an estimate of the parameters, ϵ and ζ. These estimates, denoted by $\hat{\epsilon}_1$ and $\hat{\zeta}_1$, are calculated as follows[6].

$$\hat{\zeta}_1 = \min\left(\frac{\mathcal{S}}{\mathcal{E}}\right) \tag{5.1}$$

$$\hat{\epsilon}_1 = \mathcal{E} \quad \text{for} \quad \min\left(\frac{\mathcal{S}}{\mathcal{E}}\right) \tag{5.2}$$

Table 5.2 summarizes the estimates of $\hat{\epsilon}_1$ and $\hat{\zeta}_1$ for the three rocks tested, following this approach. However, these estimates do not appear to be very reliable.

Rock	$\hat{\epsilon}_1$ (MPa)	$\hat{\zeta}_1$
Crosland Hill	45.4	0.89
Pennant	26.8	0.72
Vosges	27.5	0.65

Table 5.2: Estimate of cutting parameters (method 1).

Indeed, there is experimental evidence to suggest that ζ is not very sensitive to the rock being cut (for a given rake angle of a PDC cutter). In other words, the contact friction angle ψ at the PDC/failed rock interface appears to be fairly constant, probably in the range of 12° to 18°. However, in the "sharp" cutter experiments carried out by Chaput[10], ζ appears to increase with the strength of the rock. Furthermore, the sharp cutters experiments are characterized by a decrease of the specific energy with the depth of cut (as for blunt cutters). This dependence of ζ on the strength of the rock and the dependence of $\mathcal{E}$ on the depth of cut could both be explained by assuming a "defect" in the cutting edge of the PDC cutter (see Appendix G). If this is the case, the coordinates of the observed "cutting point" would be given:

$$\hat{\zeta} = \frac{\zeta \mathcal{E} A + \sigma A^f}{\mathcal{E} A + \mu\gamma\sigma A^f} \tag{5.3}$$

where σ is the "contact strength," and A^f and γ are two parameters that characterize defects in the cutting edge (see Appendix G). If $\zeta < 1$ and $\mu\gamma < 1$, then necessarily $\hat{\zeta}$ increases with σ. This implies that the error in estimating the cutting point increases with the strength of the rock.

5.3.2 Estimation from the Intersection of Two Lines

The cutting point is defined as the intersection of two lines, the friction line and the cutting locus. As discussed above, ζ is best estimated from the tests in the

Rock	$\hat{\epsilon}_2$ (MPa)	$\hat{\zeta}_2$
Crosland Hill	14.5	0.65
Pennant	17.0	0.65
Vosges	15.9	0.65

Table 5.3: Estimate of cutting parameters (method 2).

weakest rock, Vosges. Here, the estimate of ζ (denoted as $\hat{\epsilon}_2$) is taken to be equal to 0.65; this value of ζ corresponds to $\psi = 18^o$ (for a 15^o rake angle tool), certainly an upper bound to the "true" value of ψ, but likely to be close. The estimation of the friction line parameters by regression is very reliable, hence the cutting point is estimated by the calculation of the intersection of the estimated cutting locus and the calculated friction line:

$$\hat{\epsilon}_2 = \frac{\mathcal{E}_o}{1 - \hat{\zeta}_2 \mu} \tag{5.4}$$

where $\mathcal{E}_o$ is the intercept of the friction line on the $\mathcal{E}$-axis. Table 5.3 summarizes the values obtained by this approach.

5.3.3 Discussion

Taking the calculated intrinsic specific energy ϵ and ζ from Table 5.3, it is possible to estimate σA^f and γ for the cutting tests with the sharp cutters. Table 5.4 shows the averages for each rock. Note that the average values of γ for the tests with the new cutter are much larger than those calculated by assuming a wearflat of constant width along the cutting edge of the tool (less than 1.1). See Appendix G for further details. The estimates of ϵ shown in Table 5.3 are very close to each other, even though the rocks have significantly different peak strength (see Table 4.3 for triaxial test results). This lack of correlation between the specific energy for the cutting process and the peak strength of the rock can be explained conceptually as follows. Beyond the peak strength, a brittle rock (such as these sandstones) behaves basically as a "frictional" material. In view

Rock	γ	σA^f (N)
Crosland Hill	1.60	143
Pennant	1.63	47.8
Vosges	1.36	30.4

Table 5.4: Average σA^f and γ for tests with "sharp" cutters.

of the large strain characterizing the cutting process, the intrinsic specific energy is dominated by the energy expended when the rock has lost its cohesion. The peak strength of the rock is thus not expected to influence greatly ϵ.

5.4 Frictional Contact Forces

The contact force can be estimated by different methods. In Section 2.3, we have identified two of them: one approach is to subtract the cutting contribution from the total force, the other one is to vectorially decompose the total cutter force into its cutting and contact components. The first method requires that ϵ and ζ are known, while the second is based on the knowledge of ζ and μ. If the appropriate parameters are known, these techniques can be applied to any individual results. Yet another approach is to consider collectively all the tests conducted with the same rock and cutter (i.e. varying only the depth of cut), and to extract the contact force from a linear regression of the cutter force versus the cross-sectional area A. Two of these two techniques are presented below.

5.4.1 Subtracting the Cutting Contribution

Following Eq. (2.16), it is possible to determine the frictional contact force for the cutting tests by subtracting the cutting contribution. The intrinsic specific energy used for this calculation will be $\hat{\epsilon}_2$, as it is likely to be the closest to the true value of ϵ. The normal contact force is plotted in Figures 5.6 and 5.7 according to the sequence of tests for tool 1 and tool 2, in order to show its evolution. These figures also show the estimated normal contact force for the

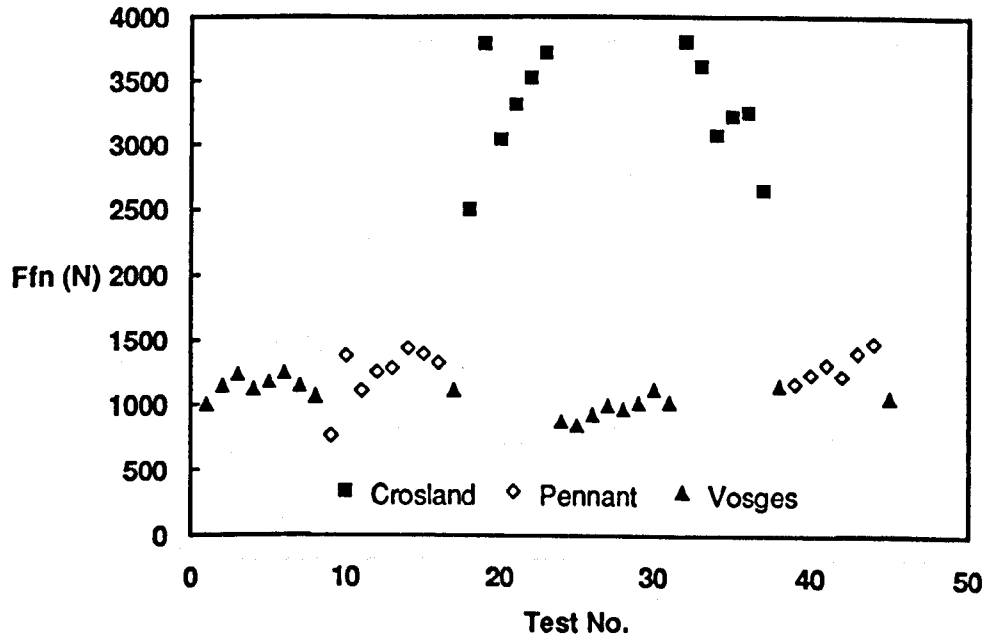

Figure 5.6: Normal contact force, F_n^f, according to test sequence (tool 1).

reference tests conducted after each series of cutting experiments. The results for the reference tests give a measure of the evolution of the tool geometry due to wear. A table with the estimated values of the contact forces can be found in Appendix H.

5.4.2 Regression Analysis

If the contact force remains approximately constant in a series of cutting experiments where only the depth of cut is changing, then the cutter force should be linearly related to the cross-sectional area of the cut, A, (assuming that the cutting process is characterized by the two constants ϵ and ζ).

Figures 5.8, 5.9, 5.10, showing the cross-sectional area versus the normal cutter force F_n for each series of tests in the three rocks, suggest that this linear relation exists. The normal contact force, F_n^f, can then be estimated as the intercept of the linear regression line with the F_n-axis. The values of the normal contact

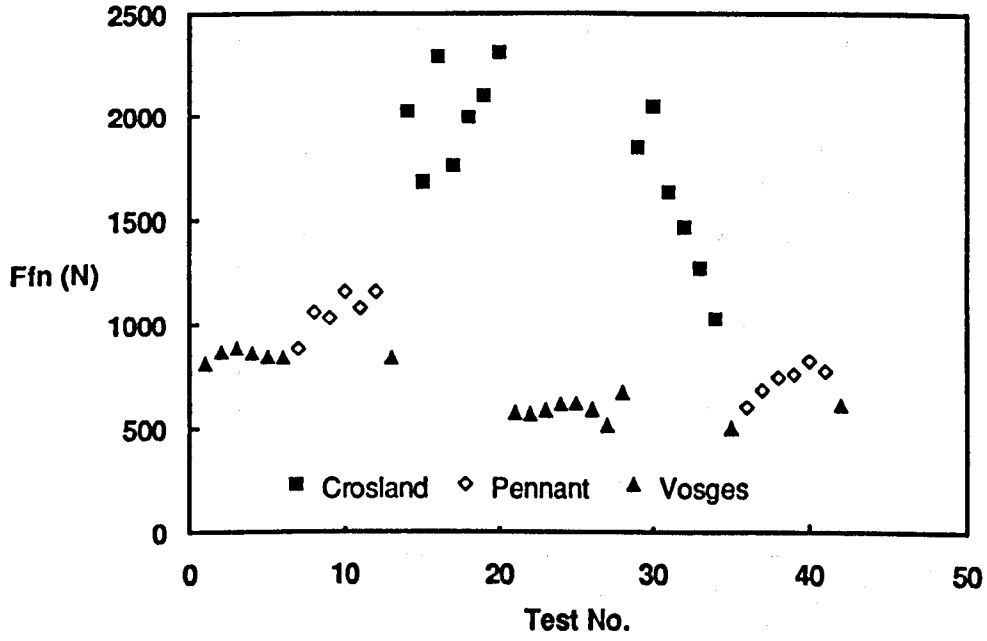

Figure 5.7: Normal contact force, F_n^f, according to test sequence (tool 2).

force, computed by linear regression, can be found in Tables 5.5, 5.6, and 5.7[1].

For the first series of tests on the Vosges with Tool 1, the graph shows a large spread for the normal contact force; this is attributed to the tool being reshaped during the first tests, even though the tool was grounded (on a rock surface) for a few metres before the experimental programme started. This spread is reflected on the regression coefficient (0.21).

5.4.3 Reference Tests

To have a measure of the development of the wear after series of each tests, reference tests were performed on the Vosges sandstone at 1 mm depth of cut. Results of these tests are plotted in Fig. 5.11 in the $\mathcal{E}$-$\mathcal{S}$ diagram. The numbers correspond to the sequence of tests. As it can be seen, the PDC cutter does not follow a constant increase in contact frictional forces as the tool wears out,

[1]Note that some of the points were not considered for the regression analysis, as they were evidently out of line.

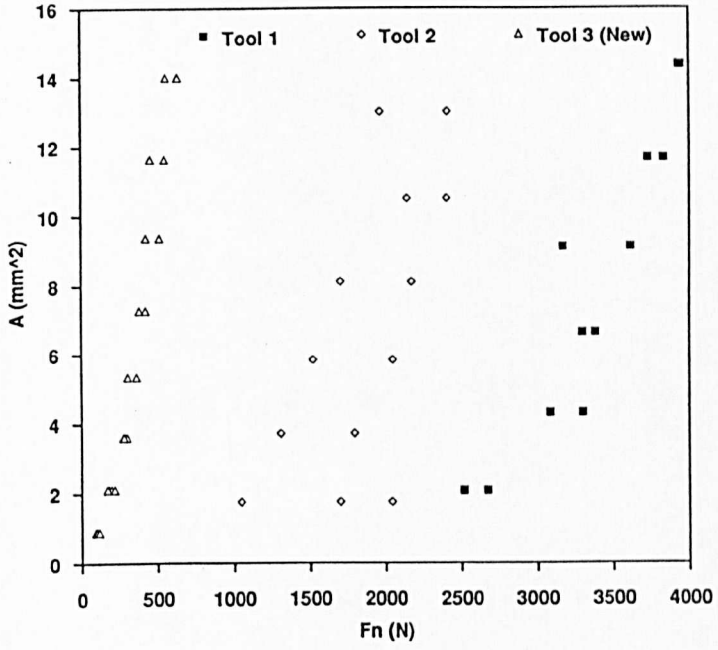

Figure 5.8: Cross-sectional area, A, versus contact force, F_n, (Crosland Hill).

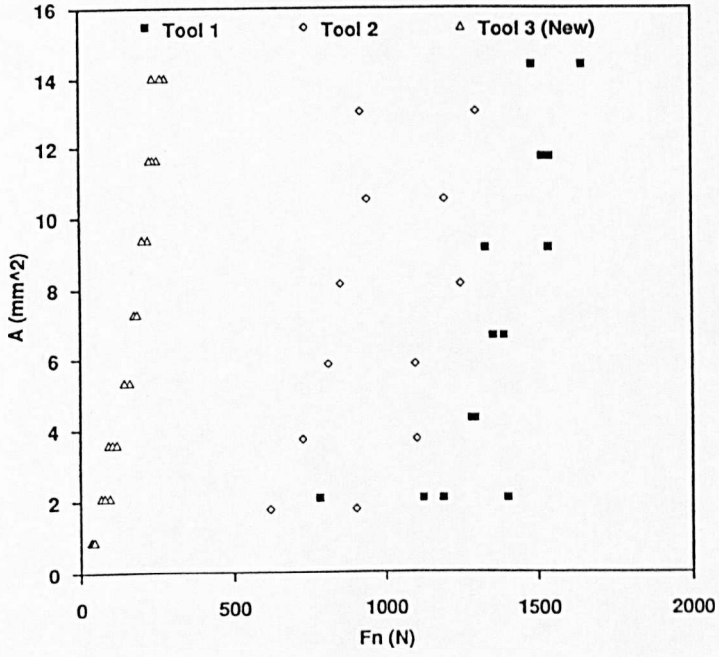

Figure 5.9: Cross-sectional area, A, versus contact force, F_n, (Pennant).

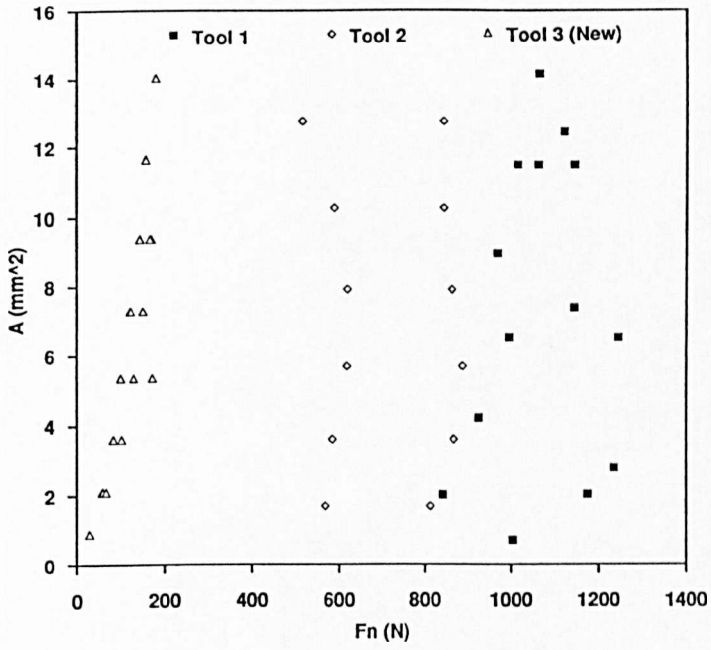

Figure 5.10: Cross-sectional area, A, versus contact force, F_n, (Vosges).

Crosland Hill	Tool 1 Series 1	Tool 1 Series 2	Tool 2 Series 1	Tool 2 Series 2
Slope (N/mm^2)	109.4	87.0	70.0	92.2
Intercept (N)	2514.8	2653.9	1590.3	957.7
r^2	0.91	0.95	0.95	0.89

Table 5.5: Crosland Hill: linear regression parameters for the force, F_n, versus cross-sectional area, A.

Pennant	Tool 1 Series 1	Tool 1 Series 2	Tool 2 Series 1	Tool 2 Series 2
Slope (N/mm^2)	30.2	34.7	30.4	27.4
Intercept (N)	1141.4	1116.9	922.1	612.7
r^2	0.76	0.90	0.81	0.89

Table 5.6: Pennant: linear regression parameters for the normal force, F_n, versus cross-sectional area, A.

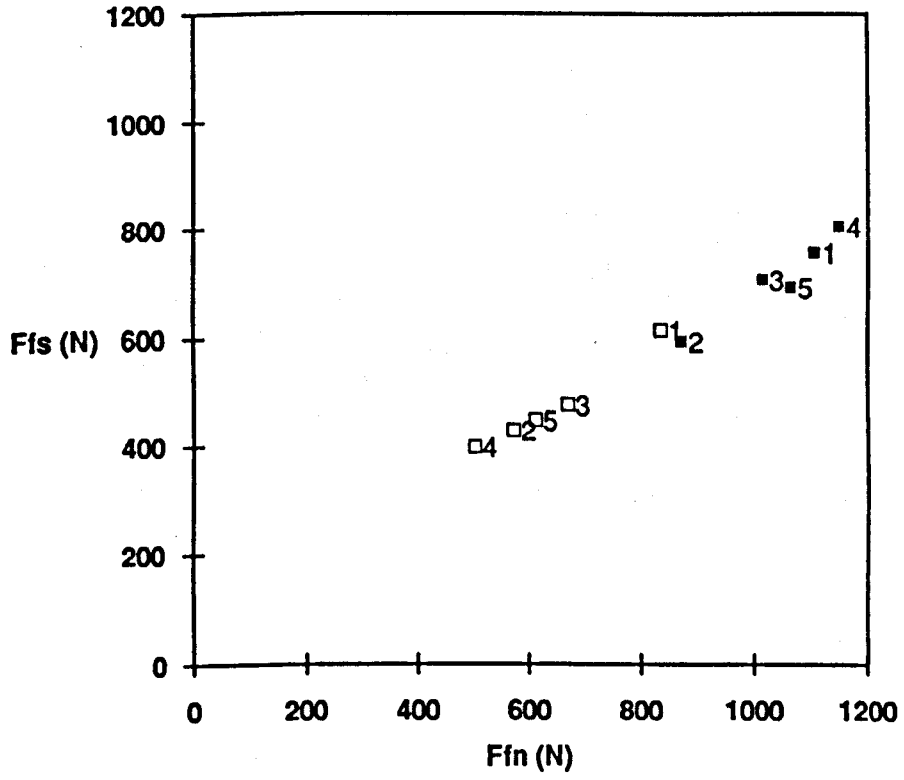

Figure 5.11: Frictional contact forces for the reference tests in Vosges.

but it decreases and then increases. This behaviour could be interpreted as a resharpening process.

5.4.4 Discussion

We have just presented two methods to evaluate the contact forces that is transmitted by the cutter wearflat. Two issues need now to be investigated:

- Can we speak of a contact strength to characterize the frictional contact process for a given rock; in other words, are the contact forces proportional to the wearflat area for a given rock

$$F_n^f = \sigma A^f \tag{5.5}$$

  where σ is the constant contact strength?

- Is there a link between the contact strength σ and other geomechanical properties of the rock?

Vosges	Tool 1 Series 1	Tool 1 Series 2	Tool 2 Series 1	Tool 2 Series 2
Slope (N/mm^2)	9.0	30.3	10.7	13.6
Intercept (N)	1149.0	832.5	847.9	574.0
r^2	0.21	0.77	0.75	0.85

Table 5.7: Vosges: linear regression parameters for the normal force, F_n, versus cross-sectional area, A.

[h]

Rock	Series 1	Series 2
Crosland Hill	2515/1590=1.58	2654/958=2.77
Pennant	1141/922=1.24	1116/613=1.82
Vosges	1149/848=1.35	833/574=1.45

Table 5.8: Ratios of Frictional Contact forces for Tool1/Tool2 by series.

	Crosland Hill	Pennant	Vosges	Reference
$\overline{\sigma}$ (MPa)	116.2	50.7	41.6	38.9
St. Dev. (Mpa)	22.2	9.3	6.5	5.9

Table 5.9: Average and standard deviation of the contact frictional stresses.

As it has been stressed earlier, the contact surfaces are evolving from test to test and it is therefore difficult to rigorously check the validity of Eq. (5.5). One approach is to compare the ratio of the forces (Tool1/Tool2) for each series of cutting experiments (the segregation by series is done to minimize the effect of the evolution of the contact surfaces). If Eq. (5.5) holds, then this ratio should be equal to the ratio of the wearflat area. The computed force ratios can be found in Table 5.8; these ratios are reasonably close to 1.53, the ratio of the wear flat area measured before conducting the cutting experiments. These tests therefore suggest that, in a first approximation, the contact forces are proportional to the wear flat area.

The contact strength for each of the sandstones can be estimated using the initial value of the contact area. Table 5.9 lists the average and the standard deviation of σ for both tools for each rock. It can be seen that the deviation from the mean is less than 20%, which is reasonable in view of the evolution of the wear flat area . A comparison of the estimate of σ with c, the rock cohesion (listed in Table 4.3), clearly indicates a correlation between the two quantities; σ increases with c.

5.5 Conclusion

An experimental investigation of the cutting action of blunt PDC cutters in three sandstones has been interpreted within the framework of the PDC bit response model.

Various methods for extracting the model parameters from the experimental results have been discussed, as identification of these constants is not always straightforward (for example estimating the contact strength σ when the contact surfaces are evolving, or evaluating the intrinsic specific energy, ϵ, with non-ideally sharp cutters).

The main conclusions that have been reached during this study can be sum-

marized as follows

- The prediction that a linear relation exists between $\mathcal{E}$ and $\mathcal{S}$ is well supported by the experimental results. For a given rock, the response of the cutter is indeed constrained by the same friction line, irrespective of the wear state of the cutter and the depth of cut. This implies that the action of a PDC cutter is at the minimum adequately characterized by the three constants (ϵ, ζ, μ) which are independent of the wear state of the tool and the depth of cut.

- The intrinsic specific energy, ϵ, is essentially the same for the three sandstones tested, even though the peak strength of these rocks varies significantly from one to another (the peak strength varies by more than one to two between the Vosges and the Crosland Hill). This conclusion is, however, reached on the hypothesis that ζ is identical for the three rocks tested. This assumption is thought to be legitimate as it is not expected that the friction angle characterizing the PDC/failed rock contact should change from one sandstone to another.

- The contact strength, σ, appears to be strongly correlated to the rock cohesion. Since the rock strength and elastic modulus are generally correlated (see Table E.1 in Appendix E), this observation gives credence to the conjecture that there is a correlation between the contact strength and the sonic transit time.

- The friction coefficient, μ, appears to reflect the internal frictional property of the rock. For the Vosges and the Pennant sandstone, the values of the friction angle measured in the cutting experiments and in the triaxial tests are the same within 2°. For the Crosland Hill sandstone, the discrepancy between the two values of φ is about 5° (the cutting experiment gives a lower value). This difference has been attributed to the dependence of the friction

angle on the confining pressure, which implies that φ must be measured at the same reference pressure (the reference pressure in the cutting experiment — in effect the contact strength — is about equal to 120 MPa, and thus larger than the maximum confining pressure of about 80 MPa achieved in the triaxial test). A further explanation could be that the rock tested was not completely dry, which weaken the rock.

Chapter 6

Conclusions

The cutting problem has been investigated for almost 40 years with the purpose of understanding the mechanisms of drilling and tunnelling. These researches have tried to correlate mechanical properties of the rock with efficiency of cutting. A problem that has been investigated, but not in great detail, is the effect of wear on the efficiency and the mechanisms of drilling.

The main conclusions from previous investigations on drag bits, frequently sharp, were that the forces are proportional to the depth of cut, they increase with rake angle, and increase with wear on the tool. From observations of the process in different conditions, the conclusion was that two different failure mechanisms could be visualized: tensile and shear failure. The cross-sectional area of the groove cut can be approximated to the cross-sectional area of the cutting face in contact with the rock for shallow depths of cut and when drilling at great depths. The resultant force acting on the tool has been explained as a combination of two actions, one of cutting the rock and another, non-productive component, mainly caused by friction at the tool/rock interface.

From the above observations, a new model for sharp and blunt cutter forces has been presented[6]. It considers that the cross-sectional area of the cut is constant and that the force components on the tool are due to the process of "pure" cutting and friction at the tool/rock interface. It is also proposed that the drilling process can be described by these two *independent* processes.

Following this new idea, a numerical simulation was performed to verify that cutting and friction at the tool/rock interface are two independent processes and to investigate their respective contributions.

From the numerical investigation the main points are as follows.

For the sharp cutter:

- the material yields in front of the cutter face;
- varying the rake angle, θ, the internal friction angle, ϕ, and the interface friction angle, ψ, showed that the shear surface changes shape and inclination with these parameters, but a good approximation of the extent of the failure on the surface of the material can be predicted by drawing the shear plane proposed by Merchant (Eq. (3.8)); and

For the wearflat contact:

- the conjecture that the forces are proportional to the wearflat length is supported by the simulations; and
- as the inclination of the wearflat increases, the normalized contact stress increases linearly.

For the blunt cutter:

- the failure processes on the cutting face and the wearflat appear similar to those in the single processes;
- changing the depth of cut in blunt cutter simulations provides enough data for an $\mathcal{E}$–$\mathcal{S}$ diagram to be plotted.

The code has proved capable of representing the cutting mechanisms. It has shown that the two mechanisms of drilling, cutting and friction at the wearflat contact, indeed appear to be *independent*, as the model adopted for this research assumed. The model provided a good insight into the progressive failure of the

material. The possibility of drawing an $\mathcal{E}$–$\mathcal{S}$ plot from the results of blunt cutter simulations has shown that the cutting forces are proportional to the depth of cut, and most importantly, that the processes of cutting and friction at the contact could be regarded as *independent.*

To substantiate the new model, an experimental investigation was designed. It consisted of linear cutting tests in three different sandstones. The cutters for the experiments had a special characteristic (that made them a complement to the work of Glowka[24, 18, 45]) *i.e.* that the wearflat made a small angle with respect to the cutting surface so as to obtain a nearly constant contact area. A limiting factor was the development of the wear during the test itself.

The well-established experimental fact that the forces increase with depth of cut could be easily reproduced with the experiments, as well as the linear relation between parallel and normal forces when cutting with sharp tools. When cutting with blunt cutters, the linear relation between the parallel and the normal force is not clearly defined; therefore, the results were interpreted within the framework of the PDC bit response model[6].

The experimental results supported the prediction of a linear relation between $\mathcal{E}$ and $\mathcal{S}$, and also that for each rock the response of the cutter is constrained by the friction line, irrespective of the state of wear of the cutter. Therefore, the action of a PDC cutter could be adequately characterized by the three constants, ϵ, ζ and μ, which are independent of the state of the tool and the depth of cut.

Since the friction angle, characterizing the PDC/failed rock contact, remains practically the same for the three sandstones tested, the intrinsic specific energy ϵ should be essentially the same. This conclusion is reached on the hypothesis that ζ is identical for the three rocks tested.

The contact strength, σ, appears to be strongly correlated to the rock cohesion, the elastic modulus and the sonic velocity of the rock.

The friction coefficient μ appears to reflect the internal frictional property of

the rock. For the Vosges and the Pennant sandstone, the values of the friction angle measured in the cutting experiments and in the triaxial tests are the same within 2°. For the Crosland Hill, the discrepancy between the two values of φ is about 5° (the cutting experiment gives a lower value). This difference has been attributed to two factors. First the dependence of the friction angle on the confining pressure, which implies that φ must be measured at the same reference pressure. In the experiments, contact stresses were about 120 MPa, and thus larger than the maximum confining pressure of about 80 MPa achieved in the triaxial test. A second explanation could be that the rock tested was not completely dry, and hence the rock was weakened.

6.1 Application and Further Research

The model that has been substantiated by numerical and experimental investigations could have several important industrial applications. In the petroleum industry, because drilling is one of the most expensive activities, measurements while drilling (MWD) with PDC bits, could give an idea of the state of wear of the bit without needing to inspect the bit by pulling it out and, at the same time, provide a geomechanical characteristic of the rock being drilled, *i.e.* the internal friction angle of the rock.

Since the cutting process can be characterized by three parameters (ϵ, ζ and μ), rock characterization for cuttability assessment when drilling with PDC could be done in a linear cutting testing machine, similar to the one at Imperial College. The linear cutting test could also become a reliable form of obtaining the friction angle of the rock without needing to carry out triaxial tests that involve sophisticated sample preparation and equipment. It could become a standard procedure of testing for cuttability. Further experimental work on different rocks, tested in dry and in saturated condition, is also needed to corroborate this research.

It is possible that the process of cutting rocks with other drag cutters could also

be regarded as two independent mechanisms. In this case, the characterization for cuttability could be done using the cutting response model as a basis for other cutter models. Further research is also needed in this area.

References

[1] Roxborough, F.F. and Rispin, A. "The mechanical cutting characteristics of lower chalk". *Tunnels Tunnelling*, 7(3):261–274, 1973.

[2] Nishimatsu, Y. "The mechanics of rock cutting". *Int.J.Rock Mech.Min.Sci.*, 9(2):261–270, 1972.

[3] Wang, J.K. and Lehnhoff, T.F. "Bit penetration into rock - a finite element study". *Int.J.Rock Mech.Min.Sci.*, **13**(1):11–16, 1976.

[4] Sellami, H. and Deliac, E. "Simulation de la pénétration d'une roche par un pic jusqu'à la rupture par la MEF". In *"Méthodes Numériques Utilisées en Mécanique des Roches*, Fountainebleau, France, 1985. Ecole Nationale Supérieure des Mines de Paris.

[5] Ingraffea, A.R. "Theory of crack initiation and propagation in rock". In Atkinson, B.K. (editor), *Fracture Mechanics of Rock*, pages 71–110. Academic Press, 1987.

[6] Detournay, E. and Defourny, P. "A phenomenological model of the drilling action of drag bits". *Int.J.Rock Mech.Min.Sci.*, **29**(1):13–23, 1992.

[7] Itasca. *FLAC Manual, Version 3.0.* Itasca Consulting Group, Inc., Suite 210, 1313 5th Street SE, Minneapolis, Minnesota 55414, 1991.

[8] Merchant, E. "Mechanics of the metal cutting process. II. Plasticity Conditions in Orthogonal Cutting". *J.Appl.Phys.*, **16**(6):318–324, 1945.

[9] Detournay, E. "Upper bound solution for wearflat contact". Personal communication, 1991.

[10] Chaput, E. *Observations and Analysis of Hard Rock Cutting Failure Mechanisms using PDC Picks.* M.Phil. Thesis, Imperial College, University of London. To be published.

[11] Fish, B.G. "The basic variables in rotary drilling". *Mine Quarry Engng.*, **27**:29–34, 1961.

[12] Fish, B.G. "The basic variables in rotary drilling". *Mine Quarry Engng.*, **27**:74–81, 1961.

[13] Fairhurst, C. and Lacabanne, W.D. "Hard rock drilling techniques". *Mine Quarry Engng.*, **23**:157–161 and 194- -197, 1957.

[14] Roxborough, F.F. and Phillips, H.R. "Experimental studies on the excavation of rock using picks". In *Proc. 3rd Congress I.S.R.M.*, Vol. II- B, pages 1407–1412, Denver, Colorado, 1974. National Academy of Science.

[15] Ip, C.K. and Fowell, R.J. "A new concept in water jet assisted drag tool cutting of rock". In *Proc. 29th U.S. Symp. Rock Mech.*, Vol. 1, pages 545--552, Minneapolis, Minnesota, 1988. A.A.Balkema.

[16] Whittaker, D. "Effect of pick shape on cutting forces". *Colliery Guardian*, **205**(5288):242–244, 1962.

[17] Zijsling, D.H. "Analysis of temperature distribution and performance of polycrystalline diamond compact bits under field drilling conditions" (SPE 13260). In *Proc. 59th Annual Tech. Conf. Exhib.*, Houston,Texas, 1984. SPE.

[18] Glowka, D.A. "Use of single cutter data in the analysis of PDC bit designs: Part 1 — Development of a PDC cutting force model". *J.Pet.Tech.*, **41**(8):797–849, 1989.

[19] Warren, T.M. and Sinor, A. "Drag bit performance modelling". *SPE Drill. Engng.*, 4(2):119–127, 1989.

[20] Barker, J.S. "A laboratory investigation of rock cutting using large picks". *Int.J.Rock Mech.Min.Sci.*, 1:519–534, 1964.

[21] Gray, K.E. , Armstrong, F. , and Gatlin, C. "Two-dimensional study of rock breakage in drag-bit drilling at atmospheric pressure". *J.Pet.Tech.*, 14(1):93–98, 1962.

[22] Nishimatsu, Y. "On the effect of tool velocity in the rock cutting". In *Proc. Int. Conf. Min. Mach.*, pages 314–319, Brisbane, Australia, 1979. Institute of Engineering.

[23] Cook, N.G.W. , Joughim, N.C. , and Wiebols, G.A. "Rock cutting an its potentialities as a new method of mining". *J.S.Afr.Inst.Min.Met.*, 68(10):435–454, 1968.

[24] Glowka, D.A. "Development of a method for predicting the performance and wear of PDC drill bits". Report SAND86-1745, Sandia National Laboratories, Albuquerque, New Mexico, 1987.

[25] Glowka, D.A. and Stone, C.M. "The thermal response of polycrystalline diamond compact cutters under simulated downhole conditions" (SPE 11947). In *Proc. 58th Annual Tech. Conf. Exhib.*, San Francisco, California, 1983. SPE.

[26] Mc.Feat-Smith, I. and Fowell, R.J. "Correlation of rock properties and the cutting performance of tunnelling machines". In *Proc. Conf. Rock Engng.*, pages 581–602, Univ. of Newcastle upon Tyne, 1977. Univ. of Newcastle upon Tyne.

[27] Misra, B. *Correlation of Rock Properties with Machine Performance.* Ph.D. Thesis, Dept. Mining and Mineral Science, University of Leeds, 1972.

[28] Morrel, R.J. , Bruce, W.E. , and Larson, D.A. "Tunnel boring technology: Disk cutter experiments in sedimentary and metamorphic rocks". Report of Investigation 7410, U.S. Bureau of Mines, 1970.

[29] Rad, P.F. and Olson, R.C. "Interaction between disk cutter grooves in rocks". Report of Investigation 7881, U.S. Bureau of Mines, 1974.

[30] Rad, P.F. and Olson, R.C. "Size distribution of rock fragments produced by rolling disk-cutters". Report of Investigation 7882, U.S. Bureau of Mines, 1974.

[31] Morgan, J.M. , Barratt, D.A. , and Hudson, J.A. "Tunnel boring machine performance and ground properties". Supplementary Report 469, TRRL, 1979. Report on the initial 1.5 km of the North Wear Drive, Kielder Aqueduct.

[32] O'Rourke, T.D. and Priest, S.D. "Some observations of machine tunnelling at the Kielder aqueduct". TRRL Report SR 532, Department of the Environment, 1979.

[33] Jenni, J.P. and Ballisat, M. "Rock testing methods performed to predict the utilization possibilities of a tunnel boring machine". In *Proc. 4th Congress I.S.R.M.*, Vol. 2, pages 267–274, Montreux, Switzerland, 1979. A.A. Balkema.

[34] McFeat-Smith, I. and Tarkoy, P.J. "Assessment of tunnel boring machines performance". *Tunnels Tunnelling.*, 9(2):29–33, 1977.

[35] Tarkoy, P.J. and Hendron, A.J. "Rock hardness index properties and geotechnical parameters for predicting tunnel boring machine performance". Report for the National Science Foundation (Grant GI-36468), Dept. of Civil Engineering, Univ. of Illinois, 1975.

[36] Nelson, P.P. and O'Rourke, T.D. "Tunnel boring machine performance in sedimentary rock." report to Goldberg-Zoino Associates of New York P.C. Geotechnical Engineering Report 83-3, School of Civil and Environmental Engineering, Ithaca, New York, 1983.

[37] Ingraffea, A.R. , Gunsallus, K.L. , and Beech, J.F. "Fracture toughness testing system for the prediction of tunnel boring machine performance". In *Proc. 23rd U.S. Symp. Rock Mech.*, pages 463- -470, Berkeley, California, 1982. AIME.

[38] Nelson, P.P. , Ingraffea, A.R. , and O'Rourke, T.D. "TBM performance prediction using rock fracture parameters". *Int.J.Rock Mech.Min.Sci.*, **22**(3):189- -192, 1985.

[39] Nelson, P.P. and Fong, F.L.C. "Characterization of rock for borability using fracture materials properties". In *Proc. 27th U.S. Symp. Rock Mech.*, pages 846- -852, Littleton, Colorado, 1986. SME.

[40] Almenara, J.R. *Rock characterization for cuttability assessment.* M.Sc. Thesis, Imperial College, University of London, 1988.

[41] Feenstra, R. "Status of Polycrystalline-Diamond- Compact bits: Part 1—Development". *J.Pet.Tech.*, 40(6):675–684, 1988.

[42] Feenstra, R. "Status of Polycrystalline-Diamond- Compact bits: Part 2—Applications". *J.Pet.Tech.*, 40(7):817–821, 1988.

[43] Varnado, S.G. , Huff, C.F. , and Yarrington, P. "The design and use of polycrystalline diamond compact drag bits in the geothermal environment". In *Proc. 54th Annual Tech. Conf. Exhib.*, Las Vegas, 1979. SPE.

[44] Cheatham Jr., J.B. and Daniels, W.H. "A study of factors influencing the drillability of shales: Single-cutter experiments with STRATAPAX drill blanks". *J.Energ.Res.Tech.*, **101**:189–195, September 1979.

[45] Glowka, D.A. "Use of single cutter data in the analysis of PDC bit designs: Part 2 — development and use of the PDCWEAR computer code". *J.Pet.Tech.*, **41**(8):850–859, 1989.

[46] Glowka, D.A. "Implications of thermal wear phenomena for PDC bit design and operation", SPE 14222. In *Proc. 60th SPE Annual Tech. Conf. Exhib.*, Las Vegas, Nevada, 1985. SPE.

[47] Cheatham, C.A. and Loeb, D.A. "Effects of field wear on PDC bit performance" (SPE 13464). In *SPE/IADC Drill. Conf.*, New Orleans, Louisiana, 1985. SPE.

[48] Clark, D.A. and Walker, B.H. "Comparison of laboratory and field data for a PDC bit (SPE 13459)". In *SPE/IADC Drill. Conf.*, New Orleans, Louisiana, 1985. SPE.

[49] Daniels, W.H. and Thompson, D.A. "Fabrication and laboratory testing of a bit containing diamond compacts" (SPE 6713). In *Proc. 52nd Ann. Fall Tech. Conf. Exhib.*, Denver, Colorado, 1977. SPE.

[50] Merchant, E. "Basic mechanics of the metal-cutting process". *J.Appl.Mech.*, **11**:A168–A175, 1944.

[51] Merchant, E. "Mechanics of the metal cutting process. I. Orthogonal Cutting and Type 2 Chip". *J.Appl.Phys.*, **16**(5):267–275, 1945.

[52] Evans, I.A. "Theory of the basic mechanics of coal ploughing". In *Proc. Int. Symp. Min. Res.*, Vol. 2, pages 761- -798, Univ. of Missouri, 1962. Pergamon Press.

[53] Lebrun, M. *Etude théorique et expérimentale de l'abattage mécanique; application à la conception de machines d'abattage et de creusement.* Doctoral dissertation, Ecole Nationale Supérieure des Mines de Paris, Fountainebleau, France, 1978.

[54] Lebrun, M. "Analyse des facteurs influencant la marche d'une machine d'abatage a pics". *Industrie Minerale - Les Techniques*, pages 269- -274, 1983.

[55] Warren, T.M. and Sinor, A. "Drag bit performance modelling" (SPE 15618). In *Proc. 62nd Annual Tech. Conf. Exhib.*, New Orleans, Louisiana, 1986. SPE.

[56] Swenson, D.V. "Modelling and analysis of drag bit cutting". SAND83-0278, Sandia National Laboratory, Albuquerque, New Mexico, 1983.

[57] Saouma, V.E. and Kleinosky, M.J. "Finite element simulation of rock cutting: a fracture mechanics approach". In *Proc. 25th U.S. Symp. Rock Mech.*, pages 792- -799, Evanston, Illinois, June 1984. AIME.

[58] Cundall, P. "Explicit finite difference methods in geomechanics". In *Numerical Methods in Engineering, Proc. EF Conf. Num. Meth. Geomech.*, Vol. 1 pages 132–150, Blacksburg, Virginia, 1976. ASCE.

[59] Marti, J. and Cundall, P. "Mixed discretization procedure for accurate modelling of plastic collapse". *Int.J.Num.Anal.Meth.Geomech.*, 6:129–139, 1982.

[60] Craig, R.F. *Soil Mechanics.* Van Nostrand Reinhold, UK, 4th edition, 1987.

[61] Detournay, E. and Atkinson, C. "Influence of pore pressure on the drilling response of PDC bits". In *Rock Mechanics as a Multidisciplinary Science*, Proc. 32nd US Symp. Rock Mech., pages 539–547, The University of Oklahoma, Norman, USA., 1991. A.A.Balkema.

[62] Dresher, A. "Lower bound on the limit force on a PDC cutter". Technical report, Schlumberger Cambridge Research, 1991.

[63] Sneddon, M. and Hall, D. "Polycrystalline diamond: Manufacture, wear mechanisms, and implications for bit design". *J.Pet.Tech.*, 40(12):1593-1601, 1988.

[64] Sellami, H., Heffernan, J., Cordelier, Ph. and Chaput, E. . "The influence of rock properties on the efficiency of mechanized mining with reference to hard rock cutting". Technical report, Imperial College London and Ecole des Mines de Paris. EEC Contract Reference: MA1M-0054-C, 1988–1990.

[65] Santarelli, F. *Theoretical and Experimental Investigation of the Stability of Axisymmetric Wellbore.* Ph.D. Thesis, Imperial College, University of London, 1987.

[66] Priest, S.D. and Selvakumar, S. "The failure characteristics of selected British rocks". Technical report, Imperial College London, 1982. Report to TRRL.

[67] Fowell, R. , Ip, C. , and Waggott, A. "High pressure water jet assisted drag tool cutting". In *CARE'88 (Conference on Applied Rock Engineering)*, pages 61–69, Newcastle upon Tyne, 1988. IMM.

[68] Armstrong, M. *Basic Geostatistics for the Mining Industry.* Centre de Geostatistique Fontainebleau, France, 1986. ERASMUS Geostatistics Course, Leuven, 10–14 Sept. 1990.

[69] Journel, A.G. and Huijbregts, Ch.J. *Mining Geostatistics.* Academic Press, London, 1978. 600pp.

Appendix A

Flac Instructions for Modelling Cutter

A.1 Sharp Cutter Model

```
ti
Shear plane detection (psi=20, phi=20, theta=16)
gr 41,21
m m
ma i=1,9 j=15
ma i=1,11 j=14
ma i=9 j=15,22
ma i=11 j=14,22
mod null reg 10,16
gen 0,0 0,3.5 1.5,3.5 1.5,0 i=1,11 j=1,14
gen 1.5,0 1.5,3.5 10,3.5 10,0 i=11,42 j=1,14
gen 1.5,3.5 1.8,4.5 10,4.5 10,3.5 i=11,42 j=14,22
gen 1,5 1.95,5 1.5,3.5 1,3.8 i=1,9 j=15,22
gen rat 0.8 0.8 i=1,11 j=1,14
gen rat 1.25 0.8 i=11,42 j=1,14
gen rat 1.25 1.25 i=11,42 j=14,22
gen rat 0.8 1 i=1,9 j=15,22
```

```
* properties of the rock E=100000 Nu=.2 Dens=1
m ss reg 19,2
prop s=41666.7 b=55555.6 d=1e-3  reg 19,2
prop fric=20 coh=1 reg 19,2
m e reg 1,20
* properties of tool E=1000000 nu=.2 dens=1
prop s=416666.7 b=555555.6 d=1e-3 reg 1,20
* defining interface
* int 1 as from 1,14 to 11,14 / bs from 9,15 to 9,22
int 2 as from 11,14 to 11,22 / bs from 1,22 to 9,22
* properties of interface
* int 1 kn=5e7 ks=5e7 coh=0 fric=20
int 2 kn=1e7 ks=1e7 coh=0 fric=20
* fix boundary
fix x i=1 j=1,14
fix y j=1
fix x i=42
ini xv 8e-6 i=1,9 j=15,22
fix x i=1,9 j=15,22
fix y i=1,9 j=15,22
apply sxx -1 i=1 j=1,14
apply sxx -1 i=42
his nste=5
his unbal
set pltc 1
set pltf 15
set large
step 1500
```

A.2 Contact Problem Model

```
gr 21,21
ti
Contact problem (phi=30 psi=30 inclination= 3deg)
m m
ma i=1,22 j=19
ma i=1,7 j=20
ma i=7 j=20,22
mod null reg 18,20
gen 0,0 0,4 2,4 2,0 i=1,8 j=1,19
gen 2,0 2,4 3,4.052 3,0 i=8,14 j=1,19
gen 3,0 3,4.052 10,4.052 10,0 i=14,22 j=1,19
gen 2,4 2,4.2 3,4.2 3,4.052 i=1,7 j=20,22
gen rat 0.8 0.8 i=1,8 j=1,19
gen rat 1 0.8 i=8,14 j=1,19
gen rat 1.25 0.8 i=14,22 j=1,19
ret
* properties of the rock E=100000 Nu=.2 Dens=1e-3
m ss reg 19,2
prop s=41666.67 b=55555.56 d=1e-3 fric=30 coh=10 T=10 reg 19,2
m e reg 1,21
* properties of tool E=1000000 nu=.2 dens=1e-3
prop s=416666.7 b=555555.6 d=1e-3 reg 1,21
* defining interface
int 1 as from 8,19 to 14,19 / bs from 1,20 to 7,20
* properties of interface
int 1 kn=1e7 ks=1e7 coh=0 fric=30
* fix boundary
```

```
fix x i=1 j=1,19
fix y j=1
fix x i=22 j=1,19
ini xv 8e-6 i=1,7 j=20,22
fix x i=1,7 j=20,22
fix y i=1,7 j=20,22
his nste=5
his unbal
his syy i=2 j=20
his sxx i=2 j=20
his sxy i=2 j=20
his szz i=2 j=20
set pltc 10
set pltf 30
set large
step 1500
```

A.3 Blunt Cutter Model

```
* blunt cutter model small wearflat (0.5mm length),
* depth of cut 1.5mm
ti
int1=cut int2=wear (phi=30 coh=10; psi1=psi2=30 tetha=16 alpha=3)
gr 41,41
m m
ma i=1,20 j=24
ma i=20 j=25,42
ma i=10 j=25,42
ma i=1,10 j=25
m null reg 19,25
```

```
gen 0,0 0,3.5 2,3.5 2,0 i=1,6 j=1,24
gen 2,0 2,3.5 2.5,3.518 2.5,0 i=6,20 j=1,24
gen 2.5,0 2.5,3.518 10,3.518 10,0 i=20,42 j=1,24
gen 2.5,3.518 2.95,5.018 10,5.018 10,3.518 i=20,42 j=24,42 gen
2,3.5 2,5.035 2.95,5.035 2.5,3.518 i=1,10 j=25,42
gen rat 0.8 0.8 i=1,6 j=1,24
gen rat 1 0.8 i=6,20 j=1,24
gen rat 1.25 0.8  i=20,42 j=1,24
gen rat 1.25 1.25 i=20,42 j=24,42
* properties of the rock E=1000000 nu=.2 dens=1e-6
m ss reg 18,1
prop s=416666.7 b=555555.6 d=1e-6 reg 18,1
prop fric=30 coh=10 t=10 reg 18,1
m e reg 5,30
* properties of the tool E=10000000 nu=.2 Dens=1e-4
prop s=4166666.7 b=5555555.6 d=1e-6 reg 5,30
* defining interfaces
* interface 1 between tool cut face and rock
int 1 as from 10,25 to 10,42 / bs from 20,24 to 20,42
* interface 2 between tool wear and rock
int 2 as from 1,25 to 10,25 / bs from 6,24 to 20,24
* interface properties
int 1 kn=5e7 ks=5e7 coh=0 fric=30
int 2 kn=5e7 ks=5e7 coh=0 fric=30
* fix boundary
fix x i=1 j=1,24
fix y j=1
fix x i=42
ini xv 8e-6 i=1,10 j=25,42
```

```
fix x i=1,10 j=25,42
fix y i=1,10 j=25,42
his nstep=5
his unbal
set pltc 10
set pltf 30
set pltt 10
set large
step 1500
```

Appendix B

Summary of FLAC Results

ϕ	ψ	θ	Merchant	$\mathcal{E}/c$ (FLAC)	Lower Bound
10	10	16.70	4.37	4.60	3.58
15	10	16.70	5.16	5.15	4.14
20	10	16.70	6.17	5.70	4.80
25	10	16.70	7.52	6.55	5.59
30	10	16.70	9.42	7.85	6.77
35	10	16.70	12.24	8.75	7.90
10	20	16.70	5.80	4.74	3.50
15	20	16.70	7.20	5.26	4.13
20	20	16.70	9.18	5.99	4.90
25	20	16.70	12.16	6.83	5.84
30	20	16.70	17.03	8.05	6.95
35	20	16.70	25.97	8.76	8.82
30	30	16.70	44.28	7.98	6.40

Table B.1: Sharp cutter model results compared to Upper (Merchant) and Lower (Dresher) solutions.

ϕ	ψ	Lower	Flac (F/lc)	Upper
10	10	4.716247	5.33	13
15	15	5.118673	6.035	22
20	20	5.645227	6.58	38.02
25	25	6.104371	7.208	90
30	30	6.486282	7.88	250
35	35	7.158279	8.28	1200

Table B.2: Flac results for contact problem compared to Upper (Detournay) and Lower (Dresher).

Wearflat (mm)	*Depth (mm)*	$\mathcal{E}/c$	$\mathcal{S}/c$	ϵ/c
1.00	0.25	2.45	1.20	9.81
1.00	0.50	4.04	2.03	8.08
1.00	0.75	5.90	2.96	7.87
1.00	1.00	8.62	4.34	8.63
1.00	1.25	9.95	5.00	7.96
1.00	1.50	11.26	5.66	7.51
0.50	0.25	2.23	1.10	8.94
0.50	0.50	4.62	2.24	9.25
0.50	0.75	5.73	2.80	7.65
0.50	1.25	10.40	5.12	8.32
0.50	1.50	12.61	6.22	8.41

Table B.3: Intrinsic specific energy ϵ from blunt cutter simulations.

Appendix C

Interface Logic

The code incorporates the facility of modelling distinct planar interfaces between two or more portions of the grid. This capability gives the opportunity to model:

- joints, faults or bedding planes in a geologic medium;
- an interface between a foundation and the soil;
- a contact between two colliding objects;
- a contact plane between a cutting tool and the rock to be cut.

The interfaces can also be used to join different parts of the grid to obtain the geometry desired.

The formulation used in the code for the calculation of the forces and stresses, can be explained following Fig. C.1, where an interface is represented by two planes connected by a shear and a normal stiffeness springs. The nodes are checked one by one for contact with the nearest point in the opposite side of the interface. Consider point N from Fig. C.1, this point is checked for contact with the segment between M and P. If there is contact, the unit normal, $\vec{n}$, to the contact is computed, and a 'length', L, for the node N, is defined as half the length to the nearest node to the left plus half the length to the nearest node to the right, *irrespective of whether the neighbouring point is on one side or the other.* Note that by this method the total length assigned to one side of

the interface is approximately half the true length of the contact (depending on grid density on each side). Fig. C.2, shows a case where an interface is used. It represents a plate inclined 2° resting on the surface of a frictional material. The plate is then displaced at constant horizontal velocity, sliding across the surface.

Using the printing and plotting facilities embedded in the code, it is possible to print out the horizontal and vertical reaction forces at the boundary of the grid (Tables C.2 and C.3). The sum of all the forces in the X and Y direction on the plate, and on the material must be equal (in case of the numerical code, very close as there is still a small unbalance force), as it is shown in Table C.2 and C.3. Table C.1 presents the data of the interface, *i.e.* the shear and the normal stresses, the normal unit vector and the 'lengths' associated to each point. The sum of the lengths assigned for each node (for each side of the interface) shows that it represents approximately half the total length, as mentioned above. The force on the plate can be calculated from this printout of the interface data. The normal and the shear forces are calculated as follows:

$$F_n = \sigma_n * LF_s = \sigma_s * L \tag{C.1}$$

where σ_n and σ_s are the normal and shear stresses and L the length related to the node. These two forces F_n and F_s can be rotated to the X and Y direction (the values for the example are shown in Table C.1).

The total force in the horizontal direction has to be taken as:

$$\frac{\Sigma(F_{xi})}{\Sigma(L_i)} * (real\ length\ of\ contact) \tag{C.2}$$

Equation C.2 is also valid for the vertical component. Another way of obtaining these forces is by adding the forces on each side of the interface. This result is more accurate as the forces related to each node act in a segment of the interface that is exclusive for the node(see Fig. C.1).

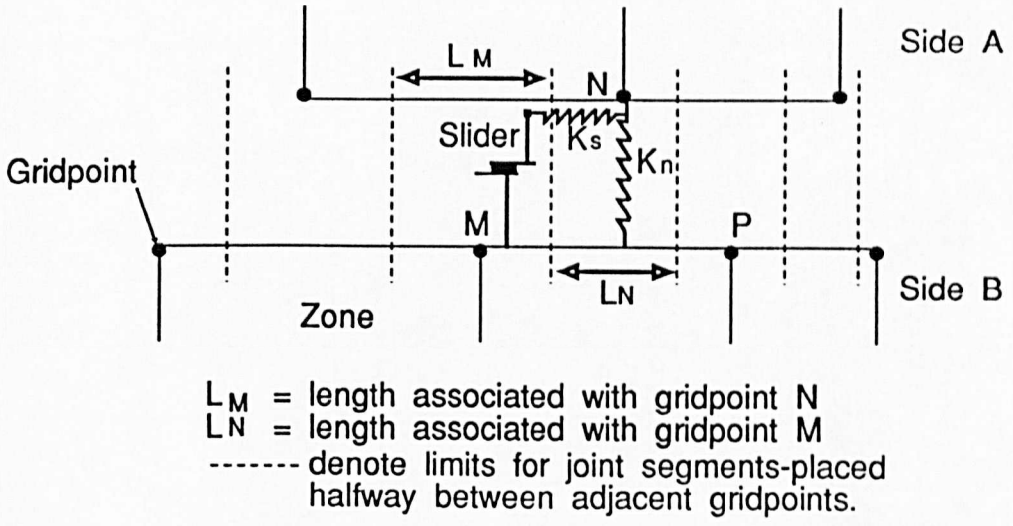

Figure C.1: Interface, sides A and B connected by shear and normal stiffness springs, (after Itasca [7])

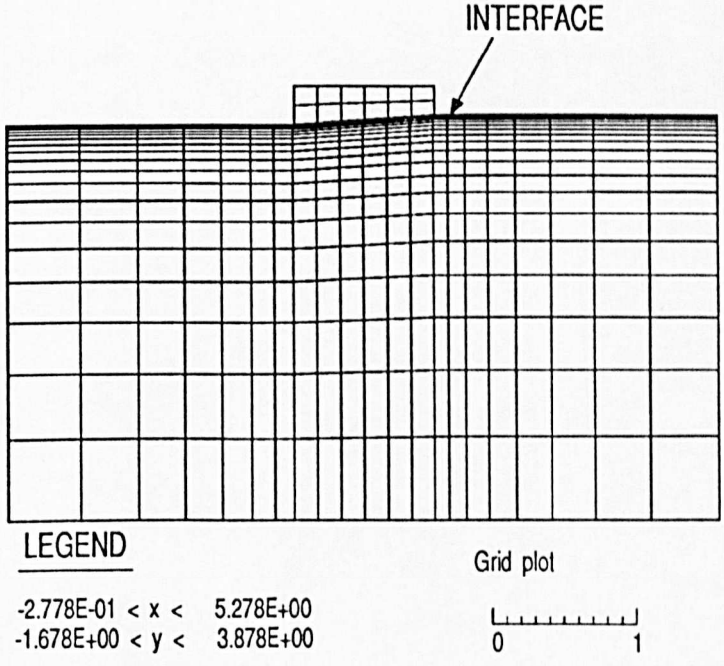

Figure C.2: Geometry of a model using interface logic

>pr if									
Interface 1									

Friction	cohesion	ks	kn	t-bond	glued?				
1.000E+01	0.000E+00	1.000E+08	1.000E+08	0.000E+00	no				
	Side-A								
	------								
i	j	normal str	shear str	slip?	unit	normal	length	Fx	Fy
8	19	0.00E+00	0.00E+00	yes	0.00E+00	0.00E+00	0.00E+00	0	0
9	19	-5.58E+01	9.83E+00	yes	5.19E-02	-9.99E-01	8.35E-02	1.06118	-4.60534
10	19	-2.08E+01	3.67E+00	yes	5.19E-02	-9.99E-01	8.35E-02	0.395625	-1.71678
11	19	-1.29E+01	2.27E+00	yes	5.19E-02	-9.99E-01	8.35E-02	0.245378	-1.06442
12	19	-5.45E+01	9.61E+00	yes	5.19E-02	-9.99E-01	8.35E-02	1.036881	-4.49964
13	19	-4.00E+01	7.06E+00	yes	5.19E-02	-9.99E-01	8.35E-02	0.76157	-3.30475
14	19	-6.15E+01	1.08E+01	yes	5.19E-02	-9.99E-01	8.35E-02	1.169936	-5.07853
15	19	0.00E+00	0.00E+00	no	0.00E+00	0.00E+00	0.00E+00	0	0
16	19	0.00E+00	0.00E+00	no	0.00E+00	0.00E+00	0.00E+00	0	0
17	19	0.00E+00	0.00E+00	no	0.00E+00	0.00E+00	0.00E+00	0	0
18	19	0.00E+00	0.00E+00	no	0.00E+00	0.00E+00	0.00E+00	0	0
19	19	0.00E+00	0.00E+00	no	0.00E+00	0.00E+00	0.00E+00	0	0
20	19	0.00E+00	0.00E+00	no	0.00E+00	0.00E+00	0.00E+00	0	0
21	19	0.00E+00	0.00E+00	no	0.00E+00	0.00E+00	0.00E+00	0	0
22	19	0.00E+00	0.00E+00	no	0.00E+00	0.00E+00	0.00E+00	0	0
	Side-B						0.5007	4.670569	-20.2695
	------								
i	j	normal str	shear str	slip?	unit	normal	length	Fx	Fy
7	20	0.00E+00	0.00E+00	no	0.00E+00	0.00E+00	0.00E+00	0	0
6	20	-5.11E+01	9.00E+00	yes	-5.19E-02	9.99E-01	8.35E-02	-0.97155	4.2164
5	20	-1.84E+01	3.24E+00	yes	-5.19E-02	9.99E-01	8.34E-02	-0.34908	1.514938
4	20	-6.28E+01	1.11E+01	yes	-5.20E-02	9.99E-01	8.34E-02	-1.19472	5.18385
3	20	-5.98E+01	1.05E+01	yes	-5.20E-02	9.99E-01	8.34E-02	-1.13727	4.935838
2	20	-3.49E+01	6.16E+00	yes	-5.19E-02	9.99E-01	8.34E-02	-0.6639	2.881403
1	20	-1.81E+02	3.20E+01	yes	-5.10E-02	9.99E-01	3.88E-02	-1.59659	6.958694
							0.45591	-5.91312	25.69112
								10.58369	45.96058

Table C.1: Example of a print out of interface data with calculated forces.

>pr xr																													
x reaction																													
	I 1	2	3	4	5	6	7																						
J22	0	0	0	0	0	0	0																						
21	0	-0.001	0	0.001	-0.001	0	0																						
20	-1.672	-1.678	-1.522	-1.497	-1.366	-1.763	-1.086	-10.585																					
								I8	9	10	11	12	13	14	15	16	17	18	19	20	21	22							
19	0.216	0	0	0	0	0	0	0	0	0	0	0	0	0	0	0	0	0	0	0	0	-0.209							
18	0.047	0	0	0	0	0	0	0	0	0	0	0	0	0	0	0	0	0	0	0	0	0.015							
17	0.058	0	0	0	0	0	0	0	0	0	0	0	0	0	0	0	0	0	0	0	0	0.021							
16	0.071	0	0	0	0	0	0	0	0	0	0	0	0	0	0	0	0	0	0	0	0	0.028							
15	0.085	0	0	0	0	0	0	0	0	0	0	0	0	0	0	0	0	0	0	0	0	0.038							
14	0.102	0	0	0	0	0	0	0	0	0	0	0	0	0	0	0	0	0	0	0	0	0.053							
13	0.121	0	0	0	0	0	0	0	0	0	0	0	0	0	0	0	0	0	0	0	0	0.074							
12	0.14	0	0	0	0	0	0	0	0	0	0	0	0	0	0	0	0	0	0	0	0	0.105							
11	0.157	0	0	0	0	0	0	0	0	0	0	0	0	0	0	0	0	0	0	0	0	0.152							
10	0.167	0	0	0	0	0	0	0	0	0	0	0	0	0	0	0	0	0	0	0	0	0.22							
9	0.164	0	0	0	0	0	0	0	0	0	0	0	0	0	0	0	0	0	0	0	0	0.32							
8	0.136	0	0	0	0	0	0	0	0	0	0	0	0	0	0	0	0	0	0	0	0	0.465							
7	0.066	0	0	0	0	0	0	0	0	0	0	0	0	0	0	0	0	0	0	0	0	0.673							
6	-0.07	0	0	0	0	0	0	0	0	0	0	0	0	0	0	0	0	0	0	0	0	0.96							
5	-0.297	0	0	0	0	0	0	0	0	0	0	0	0	0	0	0	0	0	0	0	0	1.34							
4	-0.634	0	0	0	0	0	0	0	0	0	0	0	0	0	0	0	0	0	0	0	0	1.808							
3	-1.086	0	0	0	0	0	0	0	0	0	0	0	0	0	0	0	0	0	0	0	0	2.349							
2	-1.616	0	0	0	0	0	0	0	0	0	0	0	0	0	0	0	0	0	0	0	0	2.949							
1	-0.949	0	0	0	0	0	0	0	0	0	0	0	0	0	0	0	0	0	0	0	0	1.629							
	-3.122																					12.99	9.868						

Table C.2: Reaction forces in the X direction for the grid.

>pr yr																													
y reaction																													
	I 1	2	3	4	5	6	7																						
J22	0	0	0	0	0	0	0																						
21	0	0	0	0	0	0.001	0																						
20	7.285	7.281	6.606	6.496	5.929	7.647	4.712	45.957																					
								I8	9	10	11	12	13	14	15	16	17	18	19	20	21	22							
19	0	0	0	0	0	0	0	0	0	0	0	0	0	0	0	0	0	0	0	0	0	0							
18	0	0	0	0	0	0	0	0	0	0	0	0	0	0	0	0	0	0	0	0	0	0							
17	0	0	0	0	0	0	0	0	0	0	0	0	0	0	0	0	0	0	0	0	0	0							
16	0	0	0	0	0	0	0	0	0	0	0	0	0	0	0	0	0	0	0	0	0	0							
15	0	0	0	0	0	0	0	0	0	0	0	0	0	0	0	0	0	0	0	0	0	0							
14	0	0	0	0	0	0	0	0	0	0	0	0	0	0	0	0	0	0	0	0	0	0							
13	0	0	0	0	0	0	0	0	0	0	0	0	0	0	0	0	0	0	0	0	0	0							
12	0	0	0	0	0	0	0	0	0	0	0	0	0	0	0	0	0	0	0	0	0	0							
11	0	0	0	0	0	0	0	0	0	0	0	0	0	0	0	0	0	0	0	0	0	0							
10	0	0	0	0	0	0	0	0	0	0	0	0	0	0	0	0	0	0	0	0	0	0							
9	0	0	0	0	0	0	0	0	0	0	0	0	0	0	0	0	0	0	0	0	0	0							
8	0	0	0	0	0	0	0	0	0	0	0	0	0	0	0	0	0	0	0	0	0	0							
7	0	0	0	0	0	0	0	0	0	0	0	0	0	0	0	0	0	0	0	0	0	0							
6	0	0	0	0	0	0	0	0	0	0	0	0	0	0	0	0	0	0	0	0	0	0							
5	0	0	0	0	0	0	0	0	0	0	0	0	0	0	0	0	0	0	0	0	0	0							
4	0	0	0	0	0	0	0	0	0	0	0	0	0	0	0	0	0	0	0	0	0	0							
3	0	0	0	0	0	0	0	0	0	0	0	0	0	0	0	0	0	0	0	0	0	0							
2	0	0	0	0	0	0	0	0	0	0	0	0	0	0	0	0	0	0	0	0	0	0							
1	-0.231	-0.792	-1.425	-1.962	-2.24	-2.263	-2.102	-2.325	-2.749	-2.779	-2.718	-2.666	-2.646	-2.086	-1.716	-2.034	-2.317	-2.487	-2.458	-2.199	1.844	0.821	-44.86						

Table C.3: Reaction forces in the Y direction for the grid.

Appendix D

Asyst Acquisition Code

Acquisition program for cutting tests.

```
screen.clear
echo.off

\linear.cut
\data acquisition for linear cutting tests

forget.all
normal.display
-1 6 fix.format

\defining variables

1  string rep
1  string var1
2  string var2
8  string depth_cut
32 string rock
64 string filename
64 string remarks
```

```
integer scalar Dim
7000 Dim :=

real scalar time1
real scalar time2

integer dim[ Dim ] array cutting.buffer
integer dim[ Dim ] array normal.buffer

\creating a/d.templates and digital switch for multiplexer

dash16

0 0 a/d.template cutting cutting.buffer template.buffer
0 0 a/d.template normal  normal.buffer  template.buffer

5 digital.template dig.port.out

\Data acquisition

: start.acq

\ initialisation of all the template required
    cutting a/d.init
    normal  a/d.init
    dig.port.out digital.init
\ start acquisition
    cr cr ." type  key to start acquisition with linear14.cut"
```

```
   bell key
    cr cr cr cr cr cr cr cr cr cr
    cr ."       ( 9 seconds before starting acquisition ) "
9000 msec.delay
    bell bell bell bell bell bell bell bell bell screen.clear
  cr cr cr cr cr ." acquisition ..."
    rel.time time1 :=
    Dim 1 + 1 do
        0 dig.port.out digital.out cutting a/d.in>array
        1 dig.port.out digital.out normal  a/d.in>array
    loop
    rel.time time2 :=

\ end of acquisition
    screen.clear bell
    cr cr cr cr ." test length (ms) : "
    time2 time1 - .
    cr cr cr ." type  key to continue "
    key
;

\Data plotting

\ plotting subroutine

: plot
    graphics.display
    solid
```

```
   cr ." cutting force     (part 1) "
   cutting.buffer sub[ 1 , Dim 2 / ] y.auto.plot
   cr cr ." type key     to continue " bell key

   cr cr cr ." Do you want to plot the second part ? (Y/N)"
bell
   "input rep ":=
   screen.clear
   rep " N" "= rep " n" "= or
   if
       cr ." normal force      (part 1) "
       normal.buffer sub[ 1 , Dim 2 / ] y.auto.plot
       cr cr ." type key     to continue " bell key
       screen.clear

   else
       rep " Y" "= rep " y" "= or
       if
           cr ." cutting force     (part 2) "
           cutting.buffer sub[ Dim 2 / , Dim  2 / ] y.auto.plot
          cr cr ." type key     to continue " bell key
           screen.clear

           cr ." normal force      (part 1) "
           normal.buffer sub[ 1 , Dim 2 / ] y.auto.plot
           cr cr ." type key     to continue " bell key
           screen.clear

           cr ." normal force      (part 2) "
```

```
            normal.buffer sub[ Dim 2 / , Dim 2 / ] y.auto.plot
           cr cr ." type key    to continue " bell key
            screen.clear

        else myself
        then
    then
    normal.display
;


\ you can avoid the plots :

: plot-y/n
    cr cr cr ." Do you want to plot the data ? (Y/N)"
    bell
    "input rep ":=
    rep " Y" "= rep " y" "= or
    if plot
    else
        rep " N" "= rep " n" "= or
        if
        else myself
        then
    then
;

\ Data saving
```

```
\ verify file name

: input.name
    bell
    cr ." name of file to create ( ex: Vo12_4.unr )  ? "
    "input filename ":=
    cr ." Filename : " filename "type
    ."     OK  ? (Y/N)"
    bell
    "input rep ":=
    rep " Y" "= rep " y" "= or
    if
    else myself
    then
;

\ Automatic procedure for rock name

: rock.type
    filename 2 "left var2 ":=
    var2 " ch" "= var2 " Ch" "= or var2 " CH" "= or
    if
        " Crosland Hill sandstone" rock ":=
    then
    var2 " fd" "= var2 " Fd" "= or var2 " FD" "= or
    if
        " Forest of Dean sandstone" rock ":=
    then
    var2 " Vo" "= var2 " VO" "= or var2 " vo" "= or
```

```
    if
        " Vosges sandstone" rock ":=
    then
;

\ file creation

: create.file
    input.name
    rock.type
    file.template
        5 comments
        cutting.buffer []form.subfile
        2 times
    end
    " c:\raimundo\tests\" filename "cat defer> file.create
screen.clear cr cr ." Comments : "
    cr ." depth of cut ( mm ) "
    "input depth_cut ":=
    cr ." remarks "
    "input remarks ":=

\ write

    filename defer> file.open

    "date 1 >comment
    rock 2 >comment
    depth_cut 3 >comment
```

```
    remarks 4 >comment
    .08008 "." 5 >comment

    1 subfile cutting.buffer array>file
    2 subfile normal.buffer  array>file
    file.close
;

\ asks if you want to save the data

: create.file-y/n
    cr cr cr ." Do you want to save the data ? (Y/N)"
    bell
    "input rep ":=
    rep " Y" "= rep " y" "= or
    if create.file
    else
        rep " N" "= rep " n" "= or

        if
        else myself
        then
    then
;

start.acq
plot-y/n
create.file-y/n
```

Appendix E

Geomechanical Description

Table E.1 gives a summary of the main geomechanical parameters for the Crosland Hill, Pennant, and Vosges sandstones. Results of triaxial tests can be found in Tables E.4-E.2; they are also plotted in Fig. E.1.

	Crosland Hill	Pennant	Vosges
Uniaxial Compressive Strength (MPa)	92	72	37
Tensile Strength (MPa)	7.5	9.4	3.8
Young's Moduli (MPa)	24520	17940	10800
Density (Kg/m^3)	2428	2446	2067
Sound Velocity (m/s)	3272	3354	2008
Porosity (%)	5.88	3.58	22.65
K_{Ic} ($MN/m^{1.5}$)	1.239	1.157	0.40
CERCHAR Hardness (Id points)	12	9	5
CERCHAR Abrassiveness (Ia points)	2	0.6	0.1

Table E.1: Geomechanical parameters for the three sandstones

$\sigma 3$ (MPa)	$\sigma 1$ (MPa)
0	88.59
6	106
12	136.2
24	164
30	173.5

Table E.2: Triaxial Tests Results for Pennant sandstone

$\sigma 3$ (MPa)	$\sigma 1$ (MPa)
0	54.12
4.5	79.5
9	100
18	124
23	149

Table E.3: Triaxial Tests Results for Vosges sandstone

Crosland Hill	$\sigma 3$ (MPa)	$\sigma 1$ (MPa)
Series 1	0	90
	4.5	90
	9	143.5
	18	203
Series 2	4.5	122.5
	9	153
	18	239
	23	265
	35	347
	65	482.8
Series 3 (saturated)	24.5	189.56
	63	302.76
Santarelli(1987)[65]	0	96.15
	5	135.87
	8.1	152.01
	10	168.26
	16.2	198.81
	20	225.65
	24.2	240.72
	30	275.22
	32.3	277.95
	40	312.82
	50	354.35
	60	391.52
	70	437.39
	80	475.65

Table E.4: Triaxial Tests Results for Crosland Hill sandstone

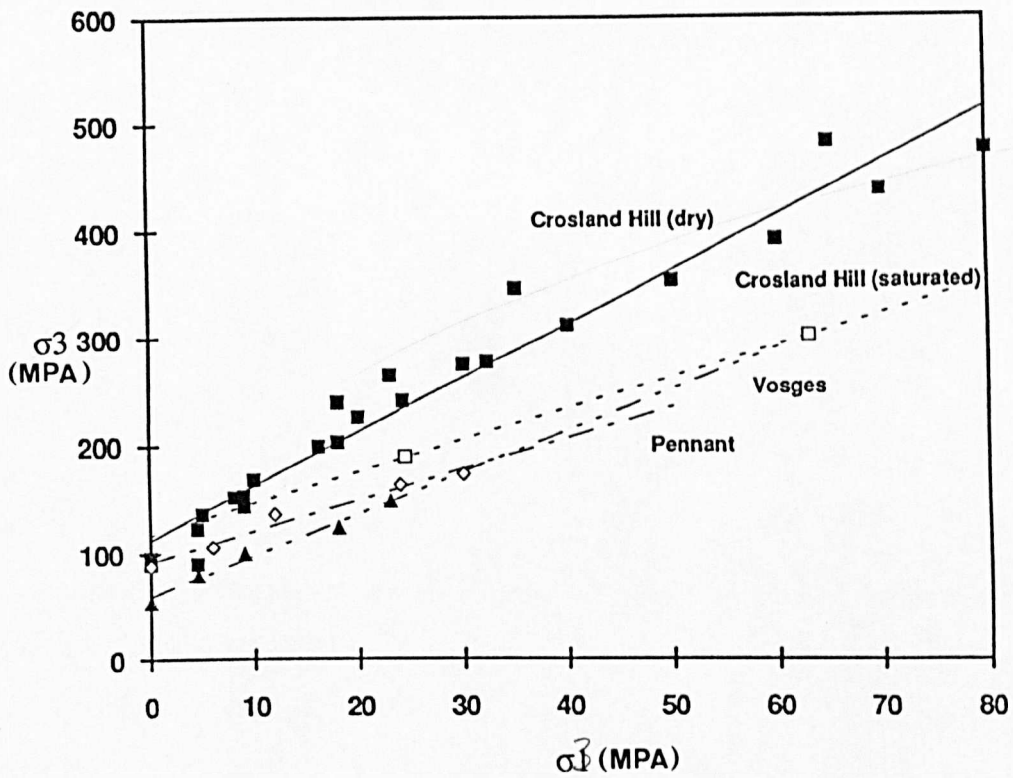

Figure E.1: Results of triaxial tests

Appendix F

Results of Cutting Experiments

The results of the cutting experiments with the blunt PDC cutters are summarized in Table F.1. For the sake of completeness, the results obtained by Chaput [10] with a "sharp" cutter are listed in Table F.2. Information for decoding the tables is given below.

Test No	Tests chronological sequence
Tool Test No	Tests sequence for each tool
Rock Type	Rock type tested
Depth (mm)	Depth of cut
Tool No	Cutter 1,2, or 3
Area (mm2)	Cross-section area of the cut
Cutting (N)	F_s, horizontal component of the cutter force
SD-Fc (N)	Standard deviation of F_s
Normal (N)	F_n, vertical component of the cutter force
SD-Fn (N)	Standard deviation of F_n
$\mathcal{S}$ (MPa)	Drilling strength
$\mathcal{E}$ (MPa)	Specific energy
Length (cm)	Length of the cutting test
Filename	Name of the cutting test record

TEST No.	Tool Test No.	Rock Type	Depth (mm)	Tool No.	Area (mm)	Cutting (N)	SD_Fc (N)	Normal (N)	SD_Fn (N)	S (MPa)	E (MPa)	Length (cm)	Filename
1	1	Vosges	0.09	1	0.724	690	157.17	1010	214.90	1394.60	952.16	30	VO001.025
2	2	Vosges	0.84	1	7.516	891	278.10	1221	379.58	162.48	118.56	30	VO002.100
3	3	Vosges	0.34	1	2.846	860	286.30	1264	444.03	444.20	302.24	30	VO003.050
4	4	Vosges	1.34	1	12.658	896	413.08	1250	608.97	98.74	70.81	30	VO004.150
5	5	Vosges	0.25	1	2.064	770	274.53	1196	457.79	579.36	372.78	30	VO005.025
6	6	Vosges	0.75	1	6.637	884	356.51	1312	573.26	197.73	133.14	30	VO006.075
7	7	Vosges	1.25	1	11.702	917	437.54	1264	654.79	108.04	78.38	30	VO007.125
8	8	Vosges	1.25	1	11.702	904	427.89	1181	606.58	100.94	77.25	30	VO008.125
9	1	Vosges	0.25	2	1.762	591	96.86	829	128.26	470.53	335.30	37.5	VO009.025
10	2	Vosges	0.50	2	3.715	634	134.08	903	169.18	243.18	170.63	37.5	VO010.050
11	3	Vosges	0.75	2	5.835	658	192.44	946	251.52	162.11	112.80	37.5	VO011.075
12	4	Vosges	1.00	2	8.103	687	265.69	944	350.13	116.53	84.72	37.5	VO012.100
13	5	Vosges	1.25	2	10.502	700	315.55	949	422.50	90.33	66.68	37.5	VO013.125
14	6	Vosges	1.50	2	13.019	771	333.16	974	428.91	74.82	59.25	37.5	V0014.150
15	7	Pennant	0.25	2	1.762	565	264.83	901	440.05	511.27	320.55	34	FD015.025
16	8	Pennant	0.50	2	3.715	698	342.31	1101	587.65	296.41	187.85	34	FD016.050
17	9	Pennant	0.75	2	5.835	708	360.81	1096	619.19	187.78	121.35	34	FD017.075
18	10	Pennant	1.00	2	8.103	811	437.18	1246	688.82	153.76	100.10	34	FD018.100
19	11	Pennant	1.25	2	10.502	816	471.16	1195	703.30	113.81	77.68	34	FD019.125
20	12	Pennant	1.50	2	13.019	918	486.30	1301	714.30	99.95	70.50	34	FD020.150
21	9	Pennant	0.25	1	2.064	504	266.93	780	424.96	377.90	244.03	34	FD021.025
22	10	Pennant	0.25	1	2.064	829	389.52	1401	766.93	678.66	401.31	34	FD022.025
23	11	Pennant	0.25	1	2.064	682	291.13	1123	559.90	544.13	330.28	34	FD023.025
24	12	Pennant	0.50	1	4.283	794	350.88	1293	685.49	301.96	185.47	34	FD024.050
25	13	Pennant	0.75	1	6.637	854	402.36	1352	733.64	203.75	128.63	34	FD025.075
26	14	Pennant	1.00	1	9.114	961	467.48	1535	849.83	168.45	105.39	34	FD026.100
27	15	Pennant	1.25	1	11.702	982	549.40	1518	940.71	129.69	83.91	34	FD027.125
28	16	Pennant	1.50	1	14.388	975	598.84	1483	978.65	103.07	67.76	34	FD028.150
29	17	Vosges	1.00	1	9.114	899	356.72	1200	503.74	131.65	98.65	30	REF1029.100
30	13	Vosges	1.00	2	8.103	737	327.93	920	426.40	113.50	90.91	30	REF2030.100
34	18	Crosland	0.25	1	2.064	1329	638.32	2518	1291.63	1219.82	643.83	32	CH034.025
35	19	Crosland	1.50	1	14.388	2100	1117.07	3932	2063.00	273.26	145.98	32	CH035.150
36	20	Crosland	0.50	1	4.283	1596	781.23	3084	1541.27	720.21	372.60	32	CH036.050
37	21	Crosland	0.75	1	6.637	1733	872.46	3381	1734.47	509.37	261.08	32	CH037.075
38	22	Crosland	1.00	1	9.114	1851	948.89	3613	1879.24	396.44	203.03	32	CH038.100

TEST No.	Tool Test No.	Rock Type	Depth (mm)	Tool No.	Area (mm)	Cutting (N)	SD_Fc (N)	Normal (N)	SD_Fn (N)	S (MPa)	E (MPa)	Length (cm)	Filename
39	23	Crosland	1.25	1	11.702	1968	1025.00	3832	2030.67	327.45	168.17	32	CH039.125
40	14	Crosland	0.25	2	1.762	1042	489.65	2040	1021.83	1158.09	591.35	32	CH040.025
41	15	Crosland	0.25	2	1.762	872	347.20	1700	686.64	964.85	495.17	32	CH041.025
42	16	Crosland	1.50	2	13.019	1378	663.05	2416	1200.63	185.55	105.82	32	CH042.150
43	17	Crosland	0.50	2	3.715	963	426.09	1795	943.81	483.22	259.23	32	CH043.050
44	18	Crosland	0.75	2	5.835	1057	491.71	2049	82.00	351.11	181.06	32	CH044.075
45	19	Crosland	1.00	2	8.103	1146	559.05	2176	1234.50	268.60	141.48	32	CH045.100
46	20	Crosland	1.25	2	10.502	1367	609.53	2410	1223.80	229.49	130.21	32	CH046.125
47	21	Vosges	1.00	2	8.103	553	152.23	655	174.26	80.87	68.27	30	REF2047.100
48	22	Vosges	0.25	2	1.762	404	77.64	584	96.73	331.67	229.18	30	VO048.025
49	23	Vosges	0.50	2	3.715	448	102.73	621	126.42	167.17	120.72	30	VO049.050
50	24	Vosges	0.75	2	5.835	498	136.31	676	164.02	115.84	85.26	30	VO050.075
51	25	Vosges	1.00	2	8.103	531	162.75	701	199.79	86.51	65.51	30	VO051.100
52	26	Vosges	1.25	2	10.502	563	226.95	695	275.89	66.20	53.63	30	VO052.125
53	27	Vosges	1.50	2	13.019	542	266.35	647	344.50	49.68	41.66	30	VO053.150
54	24	Vosges	1.00	1	9.114	734	315.93	966	413.88	106.04	80.49	30	REF1054.100
55	25	Vosges	0.25	1	2.064	582	100.64	862	145.66	417.34	281.84	30	VO055.025
56	26	Vosges	0.50	1	4.283	696	140.92	968	187.48	225.96	162.63	30	VO056.050
57	27	Vosges	0.75	1	6.637	799	364.05	1063	537.47	160.12	120.34	30	VO057.075
58	28	Vosges	1.00	1	9.114	790	346.53	1061	480.84	116.41	86.73	30	VO058.100
59	29	Vosges	1.25	1	11.702	895	425.64	1134	602.78	96.87	76.46	30	VO059.125
60	30	Vosges	1.50	1	9.114	918	455.16	1210	662.85	132.80	100.72	30	VO060.150
61	31	Vosges	1.00	1	9.114	848	349.55	1109	477.48	121.73	93.08	30	REF1061.100
62	28	Vosges	1.00	2	8.103	600	189.54	753	223.28	92.93	74.10	30	Ref2062.100
63	29	Crosland	1.50	2	13.019	1071	547.65	1973	1171.84	151.53	82.28	30	CH063.150
64	30	Crosland	1.25	2	10.502	1181	562.72	2148	1213.88	204.51	112.46	30	CH064.125
65	31	Crosland	1.00	2	8.103	986	459.07	1709	880.03	210.96	121.63	30	CH065.100
66	32	Crosland	0.75	2	5.835	834	412.99	1522	854.56	260.88	142.88	30	CH066.075
67	33	Crosland	0.50	2	3.715	791	322.02	1306	495.94	351.60	212.97	30	CH067.050
68	34	Crosland	0.25	2	1.762	637	178.36	1047	225.11	594.21	361.36	30	CH068.025
69	32	Crosland	1.50	1	14.388	2101	923.17	3945	1525.60	274.16	146.00	30	CH069.150
70	33	Crosland	1.25	1	11.702	1955	943.00	3729	1561.30	318.70	167.11	30	CH070.125
71	34	Crosland	1.00	1	9.114	1670	827.09	3170	1409.64	347.81	183.21	30	CH071.100
72	35	Crosland	0.75	1	6.637	1708	794.69	3296	1468.20	496.66	257.29	30	CH072.075
73	36	Crosland	0.50	1	4.283	1641	775.35	3299	1427.72	770.40	383.29	30	CH073.050

TEST	Tool	Rock	Depth	Tool	Area	Cutting	SD_Fc	Normal	SD_Fn	S	E	Length	Filename
No.	Test No.	Type	(mm)	No.	(mm)	(N)	(N)	(N)	(N)	(MPa)	(MPa)	(cm)	
74	37	Crosland	0.25	1	2.064	1374	635.99	2674	1130.60	1295.34	665.60	30	CH074.025
75	38	Vosges	1.00	1	9.114	948	341.80	1243	447.03	136.40	104.03	30	REF1075.100
76	35	Vosges	1.00	2	8.103	523	232.68	586	276.03	72.28	64.54	30	REF2076.100
77	36	Pennant	0.25	2	1.762	383	115.34	617	163.55	350.50	217.16	30	FD077.025
78	37	Pennant	0.50	2	3.715	449	179.53	723	313.66	194.49	120.98	30	FD078.050
79	38	Pennant	0.75	2	5.835	540	229.66	808	380.02	138.50	92.47	30	FD079.075
80	39	Pennant	1.00	2	8.103	586	258.44	849	393.46	104.79	72.30	30	FD080.100
81	40	Pennant	1.25	2	10.502	659	287.32	939	441.42	89.41	62.78	30	FD081.125
82	41	Pennant	1.50	2	13.019	675	336.38	918	499.99	70.55	51.86	30	FD082.150
83	39	Pennant	0.25	1	2.064	691	310.03	1189	676.21	576.06	334.67	30	FD083.025
84	40	Pennant	0.50	1	4.283	766	341.03	1283	717.49	299.61	178.80	30	FD084.050
85	41	Pennant	0.75	1	6.637	864	415.93	1388	795.91	209.10	130.21	30	FD085.075
86	42	Pennant	1.00	1	9.114	924	407.44	1330	617.77	145.95	101.36	30	FD086.100
87	43	Pennant	1.25	1	11.702	997	524.09	1540	843.92	131.61	85.18	30	FD087.125
88	44	Pennant	1.50	1	14.388	1051	557.19	1644	997.92	114.28	73.06	30	FD088.150
89	45	Vosges	1.00	1	9.114	834	374.42	1158	526.09	127.03	91.53	33	REF1089.100
90	42	Vosges	1.00	2	8.103	572	204.36	694	236.73	85.70	70.57	33	REF2090.100

Table F.1: Results for cutting experiments with blunt cutters (tool 1 and 2)

Rock Type	Depth (mm)	Tool No.	Area (mm)	Cutting (N)	SD_Fc (N)	Normal (N)	SD_Fn (N)	S (MPa)	E (MPa)	Filename
Pennant	0.50	3	2.106	77	46.57	65	30.21	30.89	36.57	FD24_asc
Pennant	0.50	3	2.106	119	58.40	95	40.59	45.09	56.63	FD40_asc
Pennant	0.50	3	2.106	88	50.87	77	34.26	36.78	41.80	FD43_asc
Pennant	0.75	3	3.614	103	68.31	91	49.20	25.08	28.49	FD32_asc
Pennant	0.75	3	3.614	116	65.41	103	43.21	28.59	32.04	FD25_asc
Pennant	0.75	3	3.614	124	71.22	117	49.69	32.38	34.35	FD42_asc
Pennant	0.75	3	3.614	119	70.31	117	48.31	32.43	32.87	FD44_asc
Pennant	1.00	3	5.353	186	97.53	159	65.38	29.63	34.81	FD26_asc
Pennant	1.00	3	5.353	152	96.40	141	64.35	26.41	28.40	FD33_asc
Pennant	1.25	3	7.287	211	121.10	172	81.50	23.62	28.94	FD27_asc
Pennant	1.25	3	7.287	194	119.15	183	88.24	25.18	26.57	FD34_asc
Pennant	1.50	3	9.391	285	161.34	219	105.61	23.34	30.36	FD29_asc
Pennant	1.50	3	9.391	255	156.86	201	106.35	21.38	27.12	FD35_asc
Pennant	1.75	3	11.644	340	202.77	251	133.23	21.56	29.16	FD28_asc
Pennant	1.75	3	11.644	279	196.23	237	133.51	20.36	23.99	FD36_asc
Pennant	1.75	3	11.644	313	196.16	225	129.91	19.36	26.84	FD39_asc
Pennant	2.00	3	14.029	384	223.76	278	141.95	19.81	27.35	FD22_asc
Pennant	2.00	3	14.029	352	231.56	264	151.50	18.79	25.08	FD37_asc
Pennant	2.00	3	14.029	325	215.08	237	141.25	16.90	23.16	FD38_asc
Vosges	0.25	3	0.884	43	31.85	28	18.56	31.96	48.22	VO05_asc
Vosges	0.25	3	0.884	24	22.66	30	14.33	34.15	27.37	VO21_asc
Vosges	0.50	3	2.106	70	40.70	57	23.22	26.99	33.12	VO06_asc
Vosges	0.50	3	2.106	69	39.01	59	66.93	27.91	32.84	VO13_asc
Vosges	0.50	3	2.106	86	39.09	66	21.58	31.45	40.70	VO22_asc
Vosges	0.75	3	3.614	95	55.07	83	33.55	22.84	26.19	VO07_asc
Vosges	0.75	3	3.614	103	45.81	82	69.13	22.78	28.52	VO14_asc
Vosges	0.75	3	3.614	120	54.12	100	31.29	27.77	33.19	VO23_asc
Vosges	1.00	3	5.353	109	58.85	171	34.74	31.95	20.45	VO08_asc

Rock Type	Depth (mm)	Tool No.	Area (mm)	Cutting (N)	SD_Fc (N)	Normal (N)	SD_Fn (N)	S (MPa)	E (MPa)	Filename
Crosland	0.25	3	0.884	72	52.61	104	50.75	117.83	81.23	CR29_asc
Crosland	0.25	3	0.884	65	49.95	100	50.86	112.82	73.05	CR31_asc
Crosland	0.25	3	0.884	82	52.19	95	46.41	107.78	92.93	CR28_asc
Crosland	0.25	3	0.884	75	48.74	101	48.55	113.91	84.46	CR40_asc
Crosland	0.25	3	0.884	75	51.68	116	52.94	131.38	84.47	CR43_asc
Crosland	0.50	3	2.106	145	85.44	179	77.86	85.08	68.78	CR30_asc
Crosland	0.50	3	2.106	175	92.46	195	83.68	92.73	83.16	CR33_asc
Crosland	0.50	3	2.106	149	84.42	170	77.11	80.95	70.81	CR27_asc
Crosland	0.50	3	2.106	162	84.80	215	79.84	102.00	76.77	CR41_asc
Crosland	0.75	3	3.614	246	133.72	273	122.15	75.40	67.99	CR26_asc
Crosland	0.75	3	3.614	262	133.12	287	121.45	79.49	72.45	CR32_asc
Crosland	0.75	3	3.614	269	132.05	296	118.89	81.82	74.37	CR34_asc
Crosland	0.75	3	3.614	280	123.98	276	115.77	76.37	77.52	CR42_asc
Crosland	1.00	3	5.353	310	181.18	301	159.11	56.15	57.84	CR21_asc
Crosland	1.00	3	5.353	329	182.25	363	161.19	67.83	61.51	CR35_asc
Crosland	1.25	3	7.287	365	206.24	383	179.95	52.55	50.09	CR22_asc
Crosland	1.25	3	7.287	432	235.98	424	203.28	58.23	59.25	CR36_asc
Crosland	1.50	3	9.391	442	226.56	426	57.75	45.41	47.02	CR23_asc
Crosland	1.50	3	9.391	520	282.27	513	229.23	54.68	55.33	CR37_asc
Crosland	1.75	3	11.644	474	297.69	457	242.48	39.22	40.74	CR24_asc
Crosland	1.75	3	11.644	605	342.96	550	273.14	47.22	51.98	CR38_asc
Crosland	2.00	3	14.029	637	383.48	560	306.49	39.89	45.40	CR25_asc
Crosland	2.00	3	14.029	672	404.43	638	301.56	45.45	47.87	CR39_asc
Pennant	0.25	3	0.884	50	35.30	44	24.02	49.57	56.98	FD30_asc
Pennant	0.25	3	0.884	38	32.98	32	19.49	36.36	42.80	FD21_asc
Pennant	0.25	3	0.884	34	32.40	37	20.18	41.57	37.98	FD23_asc
Pennant	0.25	3	0.884	43	35.31	42	22.11	47.63	49.10	FD41_asc
Pennant	0.50	3	2.106	86	47.85	76	33.74	36.28	40.95	FD31_asc
Vosges	1.00	3	5.353	92	64.91	99	78.62	18.51	17.12	VO15_asc
Vosges	1.00	3	5.353	171	77.62	129	47.17	24.03	31.92	VO24_asc
Vosges	1.25	3	7.287	171	101.71	120	62.50	16.50	23.47	VO09_asc
Vosges	1.25	3	7.287	153	88.62	122	86.57	16.72	21.06	VO16_asc
Vosges	1.25	3	7.287	225	98.20	150	58.97	20.62	30.93	VO25_asc
Vosges	1.50	3	9.391	206	111.91	144	68.83	15.35	21.93	VO10_asc
Vosges	1.50	3	9.391	157	107.19	143	94.21	15.26	16.69	VO17_asc
Vosges	1.50	3	9.391	259	130.33	169	78.96	18.01	27.55	VO26_2asc
Vosges	1.50	3	9.391	252	132.65	166	80.25	17.69	26.78	VO26_asc
Vosges	1.75	3	11.644	203	129.96	157	103.39	13.48	17.46	VO18_asc
Vosges	2.00	3	14.029	236	145.70	179	116.23	12.77	16.82	VO19_asc

Table F.2: Results for cutting experiments with a "sharp"cutter (tool)

Appendix G

Influence of a Defect along the Cutting Edge of a "Sharp" Cutter

According to the cutting response model, results of cutting tests with a perfectly sharp cutter should show in the $\mathcal{E}$–$\mathcal{S}$ diagram as a cluster of points that in average represents the cutting point defined $\mathcal{E} = \epsilon$ and $\mathcal{S} = \zeta\epsilon$. Perfectly sharp cutters are however ideal tools; in practice small imperfections on the cutter will have an effect on the location of the "experimental" cutting point. A γ factor is introduced for the "sharp" cutter, similar to the one for drill bits[6], that takes into account the distribution and orientation of the frictional contact forces due to small imperfections of the cutting edge. This γ factor is formely defined as

$$\gamma = \frac{F_s^f}{\mu F_n^f} \tag{G.1}$$

Let A_*^f denote the total contact area and A^f the projection of A_*^f on the horizontal plane. If the normal contact stress is a constant, σ, then the vertical and horizontal component of the contact force, F_n^f and F_s^f, can be expressed as

$$F_n^f = \sigma A^f \tag{G.2}$$

$$F_s^f = \mu\sigma A_*^f \tag{G.3}$$

It follows from Eq. (G.1), Eq. (G.2), Eq. (G.3), that the γ constant is given by:

$$\gamma = \frac{A_*^f}{A^f} \tag{G.4}$$

The apparent cutting point obtained with a "sharp" cutter having small imperfections is then

$$\begin{aligned} \hat{\epsilon} &= \epsilon + \mu\gamma\sigma\frac{A^f}{A} \\ \hat{\zeta}\hat{\epsilon} &= \zeta\epsilon + \sigma\frac{A^f}{A} \end{aligned} \tag{G.5}$$

The estimate of the cutting point improves with the depth of cut, δ, and decreasing contact strength σ.

Note that an explicit expression for γ can be obtained by assuming that the tool has a small wear flat around its edge of constant thickness, e. In this case,

$$A^f = 2e\sqrt{\delta(2R-\delta)} \tag{G.6}$$

$$A^f_* = 2eR\arccos\frac{R-\delta}{R} \tag{G.7}$$

is then given by

$$\gamma = \frac{R\arccos(R-\delta)/R}{\sqrt{\delta(2R-\delta)}} \tag{G.8}$$

is expression indicates that γ increases with the depth of cut. For the of depth of cut used in the sharp cutter experiments, the value of γ com- according to Eq. (G.8) is less than 1.1 and significantly smaller than the imentally deduced value which are in the range (1.2, 2).

ote that the cutting tests carried out with the blunt PDC cutters will give ssentially equal to 1 as the large wear flat are a under the tool overshadows fect of the small imperfections on the cutting edge.

Appendix H

Contact Stresses

Tables H.1–H.4 list the estimated values of the contact forces, computed by removing the cutting contribution from the cutter force. Information for decoding the tables is given below.

s (mm^2)	Cross-section area of the cut (A)D
Sig n (MPa)	F_n^f/A_*^f
Sig s (MPa)	F_s^f/A_*^f
Fn (N)	Vertical component of the cutter force
Fs (N)	Horizontal component of the cutter force
Ffn (N)	Vertical component of contact force $(F_n - \zeta\epsilon A)$
Ffs (N)	Horizontal component of the contact force $(F_s - \epsilon A)$
Tool Test No	Tests sequence for each tool
Tool No	Cutter 1, 2 or 3
w (mm)	Length of cutting edge of the tool
depth (mm)	Depth of cut in mm

Note that A_*^f is the wearflat area as it was measured before conducting the cutting experiments.

s	Sig n	Sig s	Fn	Fs	Ffn	Ffs	Tool Test	Tool	w	depth
(mm^2)	(MPa)	(MPa)	(N)	(N)	(N)	(N)	No.	No.	(mm)	(mm)
2.014	96.12	49.99	2518	1329	2499	1300	18	1	7.71	0.25
14.16	146.1	72.87	3932	2100	3799	1895	19	1	7.71	1.5
4.188	117.1	59.05	3084	1596	3045	1535	20	1	7.71	0.5
6.504	127.7	63.03	3381	1733	3320	1639	21	1	7.71	0.75
8.945	135.7	66.2	3613	1851	3529	1721	22	1	7.71	1
11.5	143.2	69.28	3832	1968	3724	1801	23	1	7.71	1.25
14.16	146.6	72.91	3945	2101	3812	1896	32	1	7.71	1.5
11.5	139.3	68.78	3729	1955	3621	1788	33	1	7.71	1.25
8.945	118.7	59.24	3170	1670	3086	1540	34	1	7.71	1
6.504	124.4	62.07	3296	1708	3235	1614	35	1	7.71	0.75
4.188	125.4	60.78	3299	1641	3260	1580	36	1	7.71	0.5
2.014	102.1	51.72	2674	1374	2655	1345	37	1	7.71	0.25
1.697	119.1	59.85	2040	1042	2024	1017	14	2	6.34	0.25
1.697	99.06	49.86	1700	872.2	1684	847.6	15	2	6.34	0.25
12.74	135.1	70.19	2416	1378	2296	1193	16	2	6.34	1.5
3.596	103.6	53.59	1795	963.1	1761	911	17	2	6.34	0.5
5.669	117.4	57.34	2049	1057	1996	974.8	18	2	6.34	0.75
7.894	123.6	60.68	2176	1146	2102	1032	19	2	6.34	1
10.25	136.1	71.67	2410	1367	2313	1218	20	2	6.34	1.25
12.74	109	52.13	1973	1071	1853	886.3	29	2	6.34	1.5
10.25	120.7	60.73	2148	1181	2051	1032	30	2	6.34	1.25
7.894	96.15	51.24	1709	985.6	1635	871.1	31	2	6.34	1
5.669	86.39	44.21	1522	833.8	1469	751.6	32	2	6.34	0.75
3.596	74.83	43.47	1306	791.2	1272	739.1	33	2	6.34	0.5
1.697	60.65	35.99	1047	636.5	1031	611.9	34	2	6.34	0.25

Table H.1: Contact forces (Crosland Hill)

s	Sig n	Sig s	Fn	Fs	Ffn	Ffs	Tool Test	Tool	w	depth
(mm^2)	(MPa)	(MPa)	(N)	(N)	(N)	(N)	No.	No.	(mm)	(mm)
2.014	29.15	18.06	780.2	503.8	757.9	469.6	9	1	7.71	0.25
2.014	53.03	30.55	1401	828.5	1379	794.3	10	1	7.71	0.25
2.014	42.34	24.91	1123	681.9	1101	647.7	11	1	7.71	0.25
4.188	47.95	27.81	1293	794.3	1247	723.1	12	1	7.71	0.5
6.504	49.24	28.59	1352	853.8	1280	743.2	13	1	7.71	0.75
8.945	55.24	31.1	1535	960.6	1436	808.5	14	1	7.71	1
11.5	53.5	30.24	1518	981.8	1391	786.3	15	1	7.71	1.25
14.16	51.02	28.24	1483	975	1327	734.3	16	1	7.71	1.5
2.014	44.87	25.26	1189	690.9	1167	656.7	39	1	7.71	0.25
4.188	47.57	26.71	1283	765.7	1237	694.5	40	1	7.71	0.5
6.504	50.62	28.99	1388	864.3	1316	753.7	41	1	7.71	0.75
8.945	47.35	29.68	1330	923.8	1231	771.7	42	1	7.71	1
11.5	54.34	30.82	1540	996.8	1413	801.3	43	1	7.71	1.25
14.16	57.21	31.16	1644	1051	1488	810.3	44	1	7.71	1.5
1.697	51.87	31.52	900.6	564.7	881.8	535.9	7	2	6.34	0.25
3.596	62.43	37.46	1101	697.9	1061	636.8	8	2	6.34	0.5
5.669	60.79	35.98	1096	708.1	1033	611.7	9	2	6.34	0.75
7.894	68.16	39.82	1246	811.1	1159	676.9	10	2	6.34	1
10.25	63.63	37.74	1195	815.8	1082	641.6	11	2	6.34	1.25
12.74	68.25	41.25	1301	917.8	1160	701.2	12	2	6.34	1.5
1.697	35.21	20.8	617.4	382.5	598.6	353.7	36	2	6.34	0.25
3.596	40.16	22.84	722.5	449.4	682.8	388.3	37	2	6.34	0.5
5.669	43.86	26.07	808.2	539.6	745.6	443.2	38	2	6.34	0.75
7.894	44.82	26.56	849.1	585.8	761.9	451.6	39	2	6.34	1
10.25	48.57	28.53	938.9	659.3	825.6	485.1	40	2	6.34	1.25
12.74	45.74	26.98	918.4	675.2	777.6	458.6	41	2	6.34	1.5

Table H.2: Contact forces (Pennant)

s	Sig n	Sig s	Fn	Fs	Ffn	Ffs	Tool Test	Tool	w	depth
(mm^2)	(MPa)	(MPa)	(N)	(N)	(N)	(N)	No.	No.	(mm)	(mm)
0.7055	38.57	26.09	1010	689.6	1003	678.4	1	1	7.71	0.09
7.369	44.03	29.77	1221	891.1	1145	773.9	2	1	7.71	0.84
2.78	47.51	31.39	1264	860.3	1235	816.1	3	1	7.71	0.34
12.45	43.13	26.86	1250	896.3	1121	698.3	4	1	7.71	1.34
2.014	45.2	28.37	1196	769.6	1175	737.6	5	1	7.71	0.25
6.504	47.88	30.01	1312	883.7	1245	780.3	6	1	7.71	0.75
11.5	44.04	28.24	1264	917.2	1145	734.4	7	1	7.71	1.25
11.5	40.85	27.73	1181	903.9	1062	721.1	8	1	7.71	1.25
2.014	32.34	21.15	861.6	581.9	840.8	549.9	25	1	7.71	0.25
4.188	35.55	24.23	967.7	696.5	924.4	629.9	26	1	7.71	0.5
6.504	38.3	26.74	1063	798.7	995.8	695.3	27	1	7.71	0.75
8.945	37.25	24.93	1061	790.5	968.6	648.3	28	1	7.71	1
11.5	39.04	27.38	1134	894.7	1015	711.9	29	1	7.71	1.25
14.16	40.91	26.65	1210	918	1064	692.9	30	1	7.71	1.5
1.697	47.73	33.15	828.9	590.6	811.4	563.6	1	2	6.34	0.25
3.596	50.96	33.92	903.4	633.9	866.2	576.7	2	2	6.34	0.5
5.669	52.2	33.42	946	658.2	887.4	568.1	3	2	6.34	0.75
7.894	50.75	33	944.3	686.5	862.7	561	4	2	6.34	1
10.25	49.57	31.61	948.7	700.3	842.8	537.3	5	2	6.34	1.25
12.74	49.55	33.45	974.1	771.3	842.4	568.7	6	2	6.34	1.5
1.697	33.33	22.16	584.2	403.7	566.7	376.7	22	2	6.34	0.25
3.596	34.34	23.02	621	448.5	583.8	391.3	23	2	6.34	0.5
5.669	36.32	23.96	676	497.5	617.4	407.4	24	2	6.34	0.75
7.894	36.44	23.84	701	530.8	619.4	405.3	25	2	6.34	1
10.25	34.67	23.54	695.3	563.2	589.4	400.2	26	2	6.34	1.25
12.74	30.3	19.98	646.7	542.3	515	339.7	27	2	6.34	1.5

Table H.3: Contact forces (Vosges)

s	Sig n	Sig s	Fn	Fs	Ffn	Ffs	Tool Test	Tool	w	depth
(mm^2)	(MPa)	(MPa)	(N)	(N)	(N)	(N)	No.	No.	(mm)	(mm)
8.945	42.60	29.11	1200.00	899.20	1107.55	756.97	17	1	7.71	1
8.945	33.62	22.75	966.50	733.60	874.05	591.37	24	1	7.71	1
8.945	39.10	27.16	1109.00	848.30	1016.55	706.07	31	1	7.71	1
8.945	44.25	31.00	1243.00	948.20	1150.55	805.97	38	1	7.71	1
8.945	40.98	26.62	1158.00	834.30	1065.55	692.07	45	1	7.71	1
7.894	49.30	35.95	919.70	736.60	838.12	611.09	13	2	6.34	1
7.894	33.75	25.16	655.30	553.20	573.72	427.69	21	2	6.34	1
7.894	39.50	27.93	753.00	600.40	671.42	474.89	28	2	6.34	1
7.894	29.65	23.38	585.70	523.00	504.12	397.49	35	2	6.34	1
7.894	36.05	26.25	694.40	571.80	612.82	446.29	42	2	6.34	1

Table H.4: Contact forces (reference tests in Vosges)